DISLOCATION MOBILITY

IN

MAGNESIUM OXIDE

by

B. J. WICKS

A dissertation submitted

to the University of Warwick for

admission to the degree of

Doctor of Philosophy

MEMORANDUM

This dissertation is submitted to the University of Warwick in support of my application for admission to the degree of Doctor of Philosophy. It contains an account of my own work performed at the School of Physics of the University of Warwick in the period October 1965 to June 1968 under the general supervision of Dr. M.H. Lewis. No part of it has been used previously in a degree thesis submitted to this or any other university. The work described in this thesis is the result of my own independent research except where specifically acknowledged in the text.

B J. Wicks

December 1968

B. J. WICKS

ACKNOWLEDGEMENTS

I am extremely grateful to Dr. M.H. Lewis for his continued help and encouragement throughout the course of this work and in the preparation of this thesis, and also wish to thank Professor A.J. Forty for making the facilities of the laboratories of the School of Physics available to me. Furthermore I wish to thank all those members of the School of Physics at the University of Warwick who have been available for discussion on sections of the work, particularly Dr. R. Dupree, Dr. M.J.A. Smith, and Dr. M.R. Tubbs. Workshop assistance was kindly provided by Mr. H.G. Ellacott.

My thanks are also due to the Science Research Council for providing the financial support of a Research Studentship during the period of this work.

I am grateful to Mrs. M. Archer for her care and attention in typing this thesis. Finally I wish to express my appreciation of the assistance of my wife in reading the manuscript, and for her encouragement throughout this research.

ABSTRACT

A study has been made of the influence of impurities on the flow stress of melt-grown magnesium oxide single crystals. The state of dispersion of the transition metal impurities chosen - iron, titanium, vanadium and chromium - was varied by heat treatment at temperatures up to 2,000°C in different environments, and the associated changes in flow stress measured at room temperature. Evidence for impurity redistribution in each case was derived from an application of optical and microwave absorption techniques, combined with direct microstructural observations by electron microscopy. A good correlation has been found between the experimentally observed flow stress and the calculated strengthening by dispersed obstacles identified by these methods.

In as-grown crystals the principal defects influencing the flow stress are considered to be in the form of impurity-vacancy pairs and anion-cation vacancy pairs, and it is these defects which govern the initial annealing behaviour. Additional evidence to substantiate these conclusions has been provided by measurements of the temperature dependence of the flow stress, and the recovery of neutron irradiation damage in doped crystals.

During low temperature anneals in air vacancy clustering and collapse as dislocation loops has been observed, and correlated with an initial plastic softening behaviour. Impurity oxidation also takes place under these conditions, leading to an increased concentration of impurity-vacancy pairs, and subsequently to the formation of a spinel precipitate dispersion. An explanation for the flow stress variations at low

temperatures for long ageing times is proposed in terms of a precipitation hardening-overageing behaviour in which precipitates are undeformed in the initial stages of yielding. As a result of the high nucleation rate in the supersaturated vacancy environment existing in as-grown crystals, a significant hardening is produced, even for low volume fractions of precipitate. In many cases the particle dispersion corresponding to the flow stress maximum has been found to be unresolvable. Nevertheless, a correlation of the flow stress calculated on the basis of an Orowan mechanism with the experimentally observed flow stress is possible by evaluating the precipitate volume fractions indirectly from the E.P.R. and optical results. The particle radii calculated in this way are in good agreement with the observed microstructure over the annealing ranges considered.

At elevated temperatures in air the flow stress has been found to be modified by interstitial oxygen diffusion. The centre responsible for the flow stress peak in these conditions is considered to be in the form of an interstitial oxygen ion trapped at an impurity site.

CONTENTS

1. GENERAL INTRODUCTION

1.1. Background

Interest in the ductile behaviour of ionic crystals has been shown since the discovery by Joffe[1] that normally brittle alkali halides could exhibit considerable ductility. Later experiments indicated that by suitable treatment even such a refractory ceramic compound as magnesium oxide could be moulded, by plastic deformation of single crystals, into a variety of shapes at room temperature.[2] From this arose the possibility of a ductile, polycrystalline solid which might be formed, if only to a limited extent, by plastic fabrication.

Subsequently a large amount of work has been carried out to elucidate the mechanism of flow and fracture of simple ionic crystals over a wide temperature range.

The initial claims of a viable plastic magnesia refractory have still to be realised for mainly two reasons:- Firstly, a pronounced plastic behaviour is only achieved by the removal of surface microcracks, and crystals are liable to fail in a brittle fashion if surface damage is reintroduced by mechanical contact. The extent of plastic elongation is also limited by crack nucleation at slip band intersections. Secondly, the strength and ductility of magnesium oxide is radically altered by heat treatments, which in turn is known to affect the impurity distribution, such that, in extreme cases, dislocations are completely immobilised as a result of static locking by impurity clusters and precipitates. This thesis is concerned with the second problem.

Investigations of the stress-strain behaviour and dislocation distributions in pure ionic single crystals have led to a more detailed understanding of the mechanical properties of pure crystals, but as yet only a limited

attempt has been made to understand the contribution of impurity ions as obstacles to dislocation motion. Under conditions in which impurity locking effects are absent the macroscopic flow stress of ionic crystals is determined by the mobility of freshly introduced dislocations.[3] It is well established that in commercially pure crystals of LiF dislocation mobility is controlled by impurities, while the intrinsic lattice resistance, or Peierls-Nabarro stress[4], may be quite small[5]. It is also known that the properties of commercial magnesium oxide are markedly affected by the presence of impurities, unavoidable by present growth techniques.

1.2. The Purpose and Scope of the Present Work.

The purpose of this work is to achieve an understanding of the nature of point defects and clusters of defects, introduced by intentional impurity additions, which control the flow stress of MgO during various stages of heat treatment.

The impurities chosen; iron, chromium, vanadium and titanium, have a limited solid solubility and are expected to be incorporated in precipitate lattices when heat treated at low temperatures.

The variation in state of dispersion of these impurity ions with heat treatment may be monitored using several physical techniques. In this study, concerned with transition metal impurity ions, optical and microwave spectroscopy has been combined with direct micro-structural observations by electron microscopy, in an attempt to correlate changes in the state of dispersion with mechanical flow stress measurements.

2. POINT DEFECTS AND POINT DEFECT CLUSTERS IN IONIC CRYSTALS CONTAINING IMPURITIES.

In this chapter the nature of some of the possible point defects and point defect associates in monovalent ionic lattices is described. For brevity the description will be limited to defects associated with impurity additions and whose structure is known to influence mechanical behaviour. This description is then extended to divalent (MgO type) crystals. Various physical property measurements applicable to the detection of impurity centres in ionic crystals are listed and those chosen for the present investigation are justified.

2.1. Types of Defect Identified in Monovalent Ionic Crystals.

Extensive investigations of impurity effects have been made in halide systems, where impurities can be easily introduced in variable and accurately determined concentrations during crystal growth, and the state of dispersion of impurities can be varied by quenching from relatively low temperatures near the melting point.

Substitutional incorporation of a divalent ion in a monovalent lattice requires the simultaneous introduction of either an interstitial anion or a cation vacancy to maintain overall charge compensation. It is believed that the observed hardening by divalent ions is due to vacancy defects and vacancy-impurity clusters which induce strong asymmetric lattice distortions[6].

The most important defects influencing dislocation mobility are those in which the charge-compensating cation vacancy is in close association with the divalent impurity ion. Simple configurations of these ionic defects are illustrated in Fig.2. 1(a) for a {001} plane of a rocksalt crystal lattice.

The notation used follows closely that of Kroger[7]. Here [M] is the label for a divalent impurity and [V] is a vacant cation site. $[MV]_1$ and $[MV]_2$ are defects oriented along <100> and <110> directions and resulting in tetragonal and rhombic lattice distortions respectively. Defects of lower symmetry, e.g. next-nearest-neighbour (n.n.n) centres aligned in a {111} configuration, are believed to be less important.

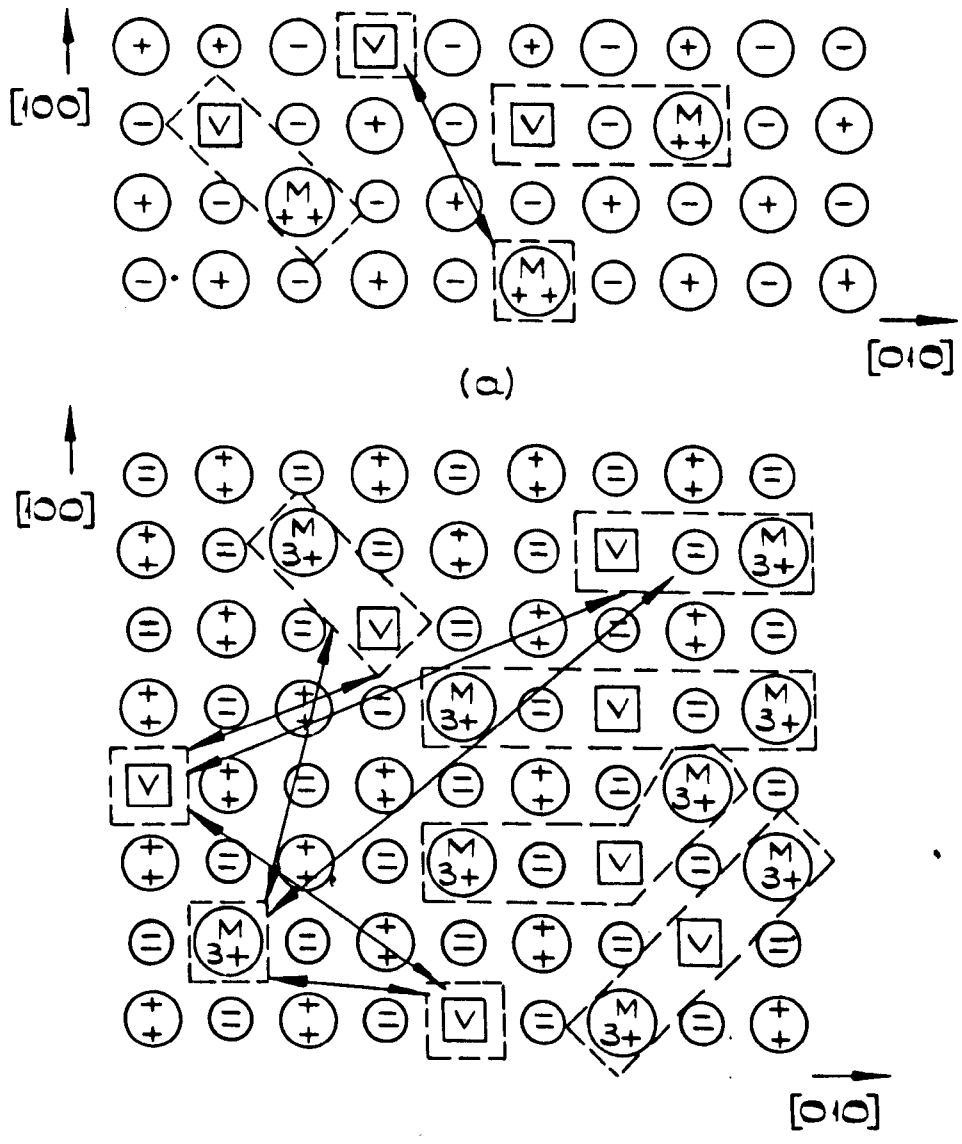

Fig. 2.1

MODELS FOR IMPURITY-VACANCY DEFECTS IN {001} PLANES OF (a) MONOVALENT NaCl-TYPE LATTICE, (b) DIVALENT MgO-TYPE LATTICE ARROWS JOINING PARTICULAR DEFECTS REPRESENT A DEGREE OF ELECTROSTATIC ATTRACTION.

Detailed experimental work, using the physical techniques described later, has confirmed that a large proportion of impurity metal ions are bound in $[MV]_1$ and $[MV]_2$ type centres for a variety of systems which contain low concentrations of impurity (150p.p.m.) after air quenches from above a temperature close to the melting point. On ageing at low temperatures (20-150°C) or a higher concentrations however, a decay in the concentration of simple dipoles is typically detected, giving rise to more complex aggregates containing three units, termed 'trimers'.

The initial aggregation follows third order kinetics, and was first discussed by Dryden[8] in terms of a clustering of dipoles three at a time followed subsequently by higher complexes formed by dipole attachment to trimers two at a time, described as 'pentamers', heptamers' etc.

Although the decay of dipoles into groups of three, five, seven or more is now well established, the structure of these aggregate centres is less defined, and appears to be sensitive to the matrix lattice.

A higher order aggregate model initially proposed by Cook and Dryden[9], formed by the addition of dipole pairs as a planar hexagonal arrangement on $\{111\}$ planes appears to be satisfactory for KCl: Sr^{2+}, KCl: Ba^{2+} and NaCl: Mn^{2+} [10]. On the other hand a 'butterfly-type' aggregate arrangement formed by dipole pairs on intersecting $\{111\}$ planes has been suggested for LiF:Mg^{2+} to explain the increased flow stress caused by clustering in this system[10]

Aggregation of Ca^{2+} - vacancy pairs in NaCl does not follow third order kinetics. The structure proposed for higher order clusters is that of a linear head-to-tail configuration of dipoles on $\{111\}$ planes[10].

2.2. Possible Defects in Divalent Ionic Lattices

The impurities under consideration in MgO exist in two or more stable ionisation states, leading to complex charge compensation effects. The

principal forms in which these impurity ions are found are now discussed.

(a) Substitutional solid solution of M^{2+}

No charge compensating vacancy is involved, and incorporation of M^{2+} substitutionally results in an isotropic elastic distortion caused by a difference in the ionic radii of M^{2+} and Mg^{2+} ions.

(b) Substitutional solid solution of M^{3+}

Only one charge compensating vacancy is necessary for every two M^{3+} ions, leading, not only to effectively negatively charged defects of similar geometry to those illustrated in Fig.2. 1(a), (designated for clarity in this case as $[M^{3+}\ V_{Mg}]_1$ and $[M^{3+}\ V_{Mg}]_2$ where $[V_{Mg}]$ represents a cation vacancy)but also more complex neutral centres of the type $[M^{3+}V_{Mg}M^{3+}]_1$, $[M^{3+}V_{Mg}\ M^{3+}]_2$ in $\langle 100 \rangle$ and $\langle 110 \rangle$directions, and split defects in which two cation vacancies are associated with an impurity ion; one in a (n.n.) site, the other in a (n.n.n.) site. These defects are illustrated in Fig.2 1(b) for a $\{001\}$ MgO plane. Lower symmetry centres on other planes are also possible.

A dipole type centre is over charge-compensated by the associated cation vacancy, and can therefore act as a trap for an anion vacancy, $[V_o]$, giving rise to a positively charged centre which continues to operate in a similar way.

(c) Substitutional solid solution of M^{4+}

Incorporation of ions of this valency in a divalent lattice is related to the situation of divalent ions in a monovalent lattice, and a similar charge compensation is to be expected, as illustrated in Fig. 2.1(a), except that, because of the higher ionic valency, binding energies are considerably greater.

(d) Metallic Precipitates

Under very severe reducing atmospheres and at high temperatures,

complete reduction of metal ions to metal precipitates has been found for iron[11] and nickel[12] impurities. Care was taken to avoid these conditions for the purposes of this study.

(e) Normal precipitates.

The stable precipitate structure expected for most of the impurities is that of the spinel lattice. Fig. 2.2. reproduces the phase diagram for the system $MgO-Fe_2O_3$[13]. Crystals grown from the melt and containing only the low molar percentage of iron used in this study are single phase above 1000°C, but during cooling or intentional ageing below this temperature the spinel precipitate magnesioferrite is formed. The phase equilibria of other spinel-forming impurities is similar to this for the concentrations investigated.

Two types of spinel structure have been identified.

The normal spinel of general formula MgM_2O_4, consists of a lattice of oxygen ions in slightly distorted cubic close packing with cations occupying interstitial positions. Each Mg^{2+} ion is surrounded tetrahedrally by anions, occupying one eighth of all possible sites of this kind, while the M impurity ion is octohedrally co-ordinated, filling one half of the possible sites. In the majority of spinels the metal ion M is in a tri-or tetravalent state.

The inverse, or equipoint, spinel structure Mg_2MO_4 has an identical anion arrangement. The four-coordinated sites are occupied by one half of the Mg ions, the remaining Mg ions, together with all M ions, being distributed over the octohedral sites in a regular way. Intermediate cation distributions are also possible e.g. in $MgFe_2O_4$.

The dimensions of the unit cell of 32 anions are determined primarily by the close packed oxygen ions, since the radii of the interstitial-occupying cations are small, and all the isostructural precipitates considered here vary very little in lattice spacing. The lattice parameter for

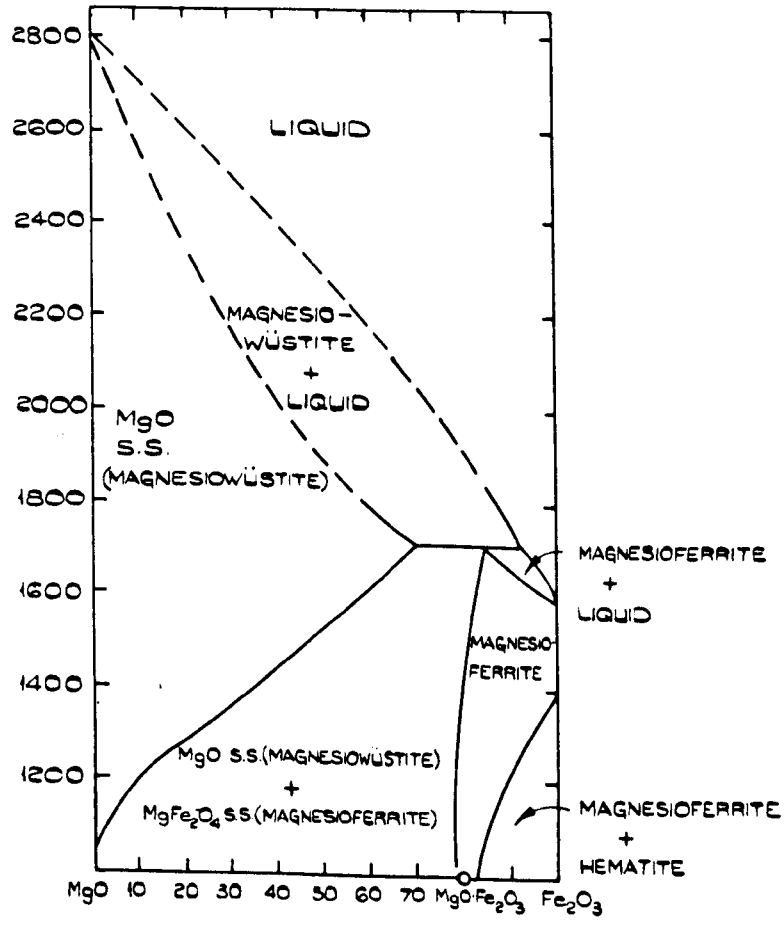

Fig. 2.2

PHASE RELATIONS IN THE SYSTEM MAGNESIUM OXIDE – IRON OXIDE IN AIR.

spinels relevant to this study is listed in Table 2.1 together with the lattice spacing of MgO for comparison.

Since in all cases only small anionic displacements are required to form the spinel lattice in an MgO matrix, nucleation of the precipitate is expected to occur readily. Reproduction and development of the spinel lattice requires only the aggregation of impurity metal ions and cation vacancies. For the normal spinel structure growth continues with the transference of Mg^{2+} ions to tetrahedral sites, and an ordering of vacancy and impurity ions in octohedral positions. In the inverse spinel, one half of the Mg^{2+} ions move to tetrahedral sites, and the remaining impurity ions, Mg^{2+} ions, and vacancies form an ordered cation sublattice.

Spinels readily form solid solutions with other oxides where the oxide structure is based on anionic close packing, and are known to accommodate large deviations from stoichiometry. Overall charge neutrality is preserved in non-stoichiometric spinels by the formation of vacancies either on the anionic or cationic sublattice sites which is not observed to destroy the ordered cation arrangement[14].

The presence of calcium as a major accidental impurity in melt-grown crystals leads one to expect the concurrent precipitation in minor quantities of the perovskite $CaMO_3$. The perovskite structure, typified by $CaTiO_3$, has a monoclinic or pseudo-cubic unit cell. Tetravalent Ti^{4+} ions occupy the corners of a slightly distorted cube, with divalent anions in edge-centering positions. The larger divalent Ca^{2+} occupies the body centre of the unit cell. The lattice can be considered essentially as the close packing of oxygen and calcium ions with titanium ions in the tetrahedral interstices.

Formula	Lattice Spacing a_o (Å)	Structure
MgO	4.213	
General Formula $Mg^{2+}M_2^{3+}O_4$		
$MgAl_2O_4$	8.086	$Mg[Al_2]\ O_4$
$MgCr_2O_4$	8.333	$Mg[Cr_2]\ O_4$
$MgTi_2O4$	8.474	$Mg[Ti_2]\ O_4$
MgV_2O_4	8.413	$Mg[V_2]\ O_4$
$MgFe_2O_4$	8.36	$Mg_{0.1}\ Fe_{0.9}[Mg_{0.9}Fe_{1.1}]\ O_4$
General Formula $Mg_2^{2+}\ M^{4+}O_4$		
$Mg_2\ Ti\ O_4$	8.445	$Mg\ [MgTi]\ O_4$
$Mg_2\ V\ O_4$	8.39	$Mg\ [Mg\ V]\ O_4$
$\gamma Fe_2\ O_3$	8.30	
$\gamma Cr_2\ O_3$	8.36	

Table 2.1.

Structure and lattice parameters of compounds with the spinel structure.[M]- denotes ions in octohedrally co-ordinated sites on the cation sublattice.

2.3. Methods of Analysis of the Structure and Concentrations of Defects Based on Physical Property Measurements.

Defects present in concentrations in excess of thermal equilibrium tend, from free energy considerations, to restore equilibrium in several ways. The annealing behaviour of such a supersaturation of point defects is conveniently monitored by a change in physical properties, which ideally can be represented in terms of a rate equation which describes the annealing kinetics, and enables one to differentiate between mechanisms for dispersal of atomic disorder.

Physical parameter variations have enabled estimations to be made of point defect formation energies, migration energies, association energies and the stability of cluster configurations in metals. Experimental data for point defects in ionic crystals is less comprehensive.

A variety of processes in ionic crystals are markedly affected by the presence of metal ions of different valence state to the host lattice. These will be mentioned briefly because of their relevance to a study of the state of dispersion of point defects, and the impact this has on a description of the interaction of defects in magnesium oxide.

2.3(a) Diffusion, Ionic and Electronic Conductivity

Although the diffusion coefficient D of a diffusing species is known to be concentration dependent in metals[15], striking variations can occur in ionic crystals.

Variations in D of 10% can be caused by a 1% change in divalent ion concentration in AgBr : Cd^{2+} [16] or even a 0.01% change in KCl : Pb^{2+} [17]. These results underline the importance of vacancies in ionic interchange processes.

Ionic and electronic conductivity have been useful techniques in studying the production and mobility of lattice defects. Simple ion

exchange processes cannot result in bulk charge transport, and the participation of vacancies and interstitials becomes even more necessary. Not surprisingly, the introduction of vacancy-inducing impurity ions leads to an enhanced conductivity, particularly at low temperatures[18], and the concentration of defects may be conveniently monitored by this method. Defect association, however, has only a second order effect, and deductions on the state of ionic dispersions from conductivity data therefore give only approximate, and not always consistent, conclusions[19]. Measurements of ionic conductivity are most useful in establishing activation energies of motion of point defects[20].

2.3(b) Dipolar Relaxation

We consider under this heading the effect of asymmetric trapped point defects, such as impurity-vacancy dipoles, capable of re-orientation under the influence of applied fields, and giving rise to either mechanical or electrical absorption peaks measured by internal friction or dielectric loss techniques. Information on defects is obtained from the degree of response of such a system of dipole moments to an externally applied driving force and its phase lag δ behind the applied force[21].

Jump configurations of bound vacancies give rise to a number of independent modes of relaxation with a range of relaxation times. In principle an analysis of the temperature and frequency dependence of an absorption band can give valuable information on jump rates and activation energies of simple complexes.

Dielectric loss and internal friction measurements have been very valuable in studying point defect configurations, and the effect of heat treatment on impurity-vacancy aggregation in a number of systems e.g. LiF : Mg^{2+} [22]; KCl : Sr^{2+}, Mn^{2+}, Ba^{2+} [23] and NaCl:Ca^{2+}, Mn^{2+}, Cd^{2+} [10][24][25]

2.3(c) Optical and Microwave Absorption

Electron spin resonance and optical absorption techniques do not lend themselves to a study of impurity-vacancy association in the alkali halides for the impurities normally used. Spectra caused by the proximity of vacancies to Mn^{2+} ion sites have been reported however[26][27], and this technique promises to be successful in identifying the state of dispersion of impurity ions where the impurity is paramagnetic.

2.3(d) Yield Stress

Early investigations showed that very small concentrations of divalent metal impurity ions were responsible for a considerable increase in the hardness of alkali halides[28][29][30], relative to a comparable monovalent ion content. More detailed information is now available on similar systems. e.g. LiF : Mg^{2+} [5]; NaCl : Ca^{2+} [31]; and NaCl : Sr^{2+} Cu^{2+}, and Mn^{2+}[32]; and the sensitivity of the flow stress on the degree of anisotropy of lattice defects caused by substitutional metal cations has been confirmed.

Basically two models have been developed for the interaction between glide dislocations moving on $\{110\}$ planes and the anisotropic strain field around a small defect.

Fleischer[6][33] considered centres which formed rigid static obstacles to dislocation motion. The predictions of this theory were applied successfully to observations on LiF : Mg^{2+}

Pratt et al.[34] calculated the effect of a stress-induced dipole ordering in the long range stress field of moving dislocations, and showed these results to be in good agreement with experimental data on NaCl ; Ca^{2+}. In both cases, however, the state of dispersion of defects was inferred

from previously reported observations, and not confirmed by direct analysis.

It would appear from the fact that these two similar systems show marked differences in behaviour under similar conditions, that although the defects responsible for hardening in doped crystals are fairly well established, knowledge of the precise mechanism of interaction is less satisfactory. Further anomalies are evident if we consider the quenching and ageing characteristics of these systems.

In the system LiF : Mg^{2+} a quench softening behaviour, in rapidly cooled crystals containing low Mg^{2+} concentrations[35], has been identified with an increase in dielectric absorption by impurity ion-cation vacancy dipoles[10]. Moreover, the increased hardness observed during anneals at intermediate temperatures is the result, not of the formation of trimers, but of the association of dipoles to aggregates of higher order. It is difficult to visualise an aggregate in which the total lattice strain is more than the sum of the individual dipoles; and clearly the treatment of Fleischer does not apply in this case.

In other systems such as NaCl ; Mn^{2+}, rapid cooling of lightly doped crystals (50 ppm) results in a decrease in strength over that of slowly cooled crystals for a different reason. This type of behaviour has been correlated with a higher density of dipoles formed during slow cooling[36].

At higher concentrations (200 p.p.m.) measurements during post-quench annealing at intermediate temperatures suggests that although the critical resolved flow stress is lowered by heat treatment, the flow stress is insensitive to the dispersion of impurities[10]. Other corroborative observations on this system, KCl : Sr^{2+}, KCl : Ba^{2+}[10]; and NaCl : Cd^{2+} [36]

confirm that although quenched crystals, containing a high proportion of impurity in dipole form, show an increase in hardness over those subject to slow cooling and containing high order aggregates, the hardness is insensitive to the initial stages of dipole aggregation.

Flow stress variations in the system NaCl : Ca^{2+} also show anomalous effects. At low concentrations the flow stress is fairly insensitive to ageing treatment, while at higher concentrations an enhanced flow stress on ageing has been attributed to the formation of a complex aggregate structure[10].

2.4 The Application of Physical Property Measurements to Magnesium Oxide.

In section 2.3. several physical property measurements were described which have been utilised, with varying degrees of success, in a study of the state of impurity ions in monovalent systems. The results of these techniques have indicated that a high proportion of impurities may be associated with vacancies as dipoles, and the morphology of higher order clusters have been identified. The applicability of these techniques to a study of MgO in particular is now discussed.

The advantage of working with MgO is that it has a simple, predominantly ionic, structure identical to NaCl, which enables a direct comparison to be made of defects in the two systems. Fig. 2.3(a) shows a representation of a unit cell of the crystal structure. The normal fracture path is the $\{100\}$ cleavage plane. Macroscopic plastic deformation experiments indicate that the glide elements at room temperature are $\{110\}\ \frac{a}{2}\langle 1\bar{1}0\rangle$ shown diagramatically in Fig.2.3(b).

The electrical conductivity of single MgO crystals has been measured by several investigators, and conflicting data on the mechanism of charge

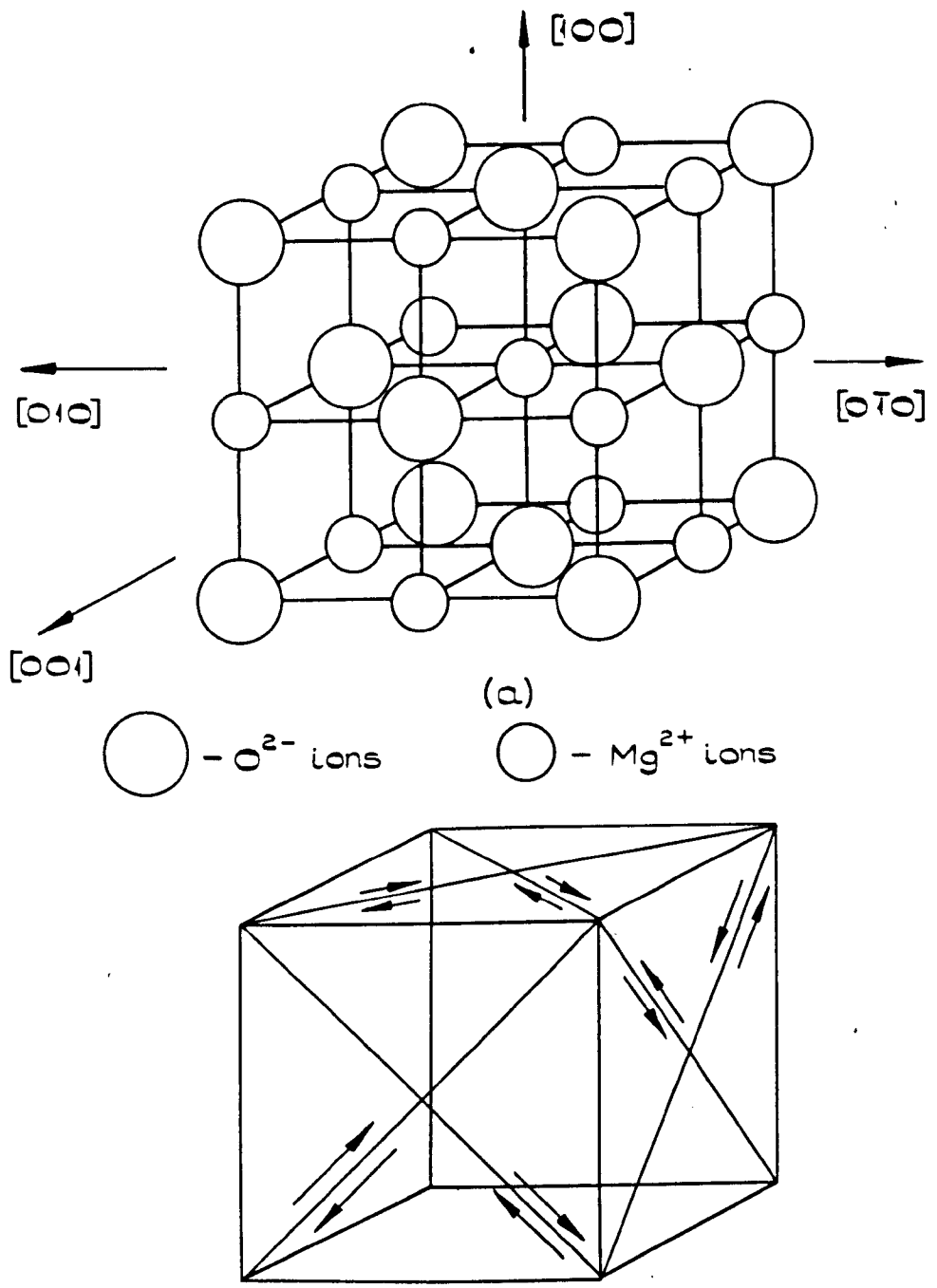

Fig. 2.3

REPRESENTATION OF (a) THE STRUCTURE

(b) SLIP SYSTEMS OF MgO

transport are reported[37]. Because of the lack of consistent results on pure crystals and the experimental difficulties involved in the measurements, this technique is not expected to prove useful for analysing impurity effects in MgO.

The interpretation of more complex centres by relaxation experiments in a divalent lattice is expected to be less satisfactory than in monovalent systems because the relaxation of numbers of discrete modes will obscure the details of individual processes. Other investigations using these techniques have made little progress in determining the nature of the more complicated ionic defect groups in magnesium oxide. Southgate[38] identified a broad internal friction peak in MgO occuring at 850°C with a large number of complicated relaxation modes associated with a deliberate trivalent dopant.

Observations of dislocation damping at a lower temperature (0-300°C) have given a value for the interaction energy between dislocations and Fe^{3+} ions of 0.035 eV[39]. Significantly, Fe^{2+} ions were shown to have considerably less influence.

Both these techniques have the disadvantage that they are most usefully applied at temperatures above 400°C, i.e. temperatures at which point defect clustering and impurity oxidation or reduction by atmospheric influence is expected. These techniques were, therefore, not used for the present research.

Optical and microwave spectroscopy may be used to study a static configuration of defects and, more important, a particular configuration of vacancy and paramagnetic impurity ion may be isolated from a complex background and unambiguously identified by its characteristic spectrum.

Electronic transitions detected by microwave and optical absorption spectra in doped, and irradiated, MgO have been identified with defects for which the analogues in monovalent lattices have known large dislocation interaction energies. No attempt has yet satisfactorily identified these or any other defects precisely with flow stress variations after heat treatment. In the work described in this thesis spectroscopical techniques are used to correlate the changes in concentration of impurity centres during ageing treatments over a wide temperature range with associated variations in dislocation mobility.

MgO is a useful material for plasticity experiments of this kind, since slip may be precisely controlled by the injection of fresh dislocation sources at the surface. The role of grown in, aged, and fresh dislocations in the initiation of plastic flow can be isolated in terms of static and dynamic pinning effects[40]. It is also possible to distinguish, from the character of etch pits, between fresh, aged, grown-in dislocations, and precipitates[41].

Polishing techniques for specimen preparation prior to electron microscopical examination are well known. Direct examination is not possible for the alkali-halides, and the ability to study the microstructure of MgO by this method is a considerable asset in determining the dispersion of impurity ions during ageing treatments, and in identifying precipitates of a second phase.

The applications and limitations of the techniques of spectroscopy and electron microscopy to the systems under study are discussed in Chapter 3.

3. THE SYSTEM UNDER INVESTIGATION

This Chapter extends the discussion of impurity effects in ionic crystals, developed earlier, to magnesium oxide. A description is given of the process of crystal growth by which crystals are conventionally prepared in both pure form and containing deliberately introduced impurities. The underlying principles of techniques which are subsequently used to investigate the state of impurity in melt-grown crystals are presented, and previous work in both nominally pure and doped crystals is briefly reviewed.

3.1. Crystal Growth and Impurity Incorporation

Many metallic impurities have a limited solid solubility in MgO, and are found as natural impurities in the oxide powder used for crystal growth. The most important of these are listed in Table 3.1 with the appropriate ionic radii[42]. It is clear that the majority of the cations have ionic radii close to that of Mg^{2+}, making it possible to introduce concentrations of up to 1 wt.% of a selected impurity substitutionally into the structure and thereby to study each impurity effect separately.

Also important in relation to this work, is that any lattice distortion by isolated impurity ions is expected to be small, and vacancy association effects will be more readily detected.

Attempts to grow crystals by the arc fusion method were unsuccessful in producing crystals of a sufficient size for use in this study, because of the sensitivity of the process to particle size in the raw powder, and crystals were supplied commercially. Nevertheless a description of the process is relevant because of its importance in determining the distribution of impurity ions in single crystals.

In the arc fusion process, an arc is struck between two carbon

Element	Valency	Ionic Radius (Å)
Al	+3	0.51
Ca	+2	0.99
Co	+2	0.72
Cr	+1	0.81
	+2	0.89
	+3	0.63
Fe	+2	0.76
	+3	0.64
Li	+1	0.68
Mn	+2	0.80
	+3	0.66
	+4	0.60
Ti	+2	0.94
	+3	0.76
	+4	0.68
V	+2	0.88
	+3	0.74
Zr	+4	0.79
Mg	+2	0.66
O	-2	1.32
	-1	1.76

Table. 2.1.

Table of ionic radii of ions commonly found in MgO, together with the radii of Mg^{2+} and O^{2-} ions.

electrodes inserted into a presintered MgO powder compact, melting and ionizing a small amount of material in the immediate vicinity of the discharge. Stabilised by the presence of an ionized atmosphere, the electrodes can then be separated, forming a molten zone which crystallises as the electrodes are gradually raised. Growth of columnar crystals continues until the discharge is spontaneously quenched at a critical electrode spacing. The period of cooling following this is of quite arbitrary duration, depending principally on the size of the melt.

Impurities may be introduced into the melt by mixing into the compact the appropriate oxide powders, e.g. V_2O_5, TiO_2, Fe_2O_3 etc. which are then incorporated in the lattice during crystallisation.

This method of crystal growth is very unsatisfactory from the point of view of the unpredictable impurity content of doped crystals, and an uncertain cooling rate during which vacancy and impurity clusters are formed. The presence of accidental impurities is unavoidable, since there is no method at present of refining the starting material to better than 100 p.p.m. of impurity.

The distribution of deliberate dopant is not found to be homogeneous over a melt. Crystals frequently have a 'banded' appearance caused by regions of higher impurity concentration, and a marked impurity segregation is noticeable at the top of the melt.

Crystals used in this study were supplied by W. & C. Spicer Ltd., Winchcomb, Glos. and Mr.J.H. Burrow of The University of Bristol, using powder obtained from the Canto Chemical Co. of Japan Ltd, Crystals containing 100 p.p.m. impurity were purchased from the Monocrystal Co. Cleveland, U.S.A.

A table of the crystal melts used is given in Table 3.2, listing

the predominant impurity together with a spectrographic analysis of the impurity concentration.

Reference used in the Text	Impurity Concentration Concentrations in p.p.m. except where otherwise stated.
V : 1	V 0.15%, Ca 400, Fe 150, Al ~20 Ti<50, Si 30, Mn 15, Zr >, Zn, Co. Cr Each<20, Mo<10, Be, Cd, Cu, Sn Each<5 Others<5
Ti : 1	Ti 0.1%, Ca 200, Fe 300, Al<70, V<50, Si 30, Mn 15, Others<5
Ti : 2	Ti 500, others undetermined
Cr : 1	Cr 600, others undetermined
Cr : 2	Cr 0.13%, others<100
Fe : 1	Fe 900, others undetermined
Fe : 2	Fe 0.75%, others<100
P : 1	< 100
P : 2	400

Table 3.2.

A description of crystal melts used in this study.

3.2. The Detection of Paramagnetic Centres by Electron Paramagnetic Resonance

The iron group transition metals, with which this research is mainly concerned, are characterised by a partially filled inner 3d shell, and induced excited states arise principally from a re-arrangement of the coupling of the inner electrons. For these transition metal ions, characteristically, the crystal field is of moderate strength, being larger than the spin-orbit coupling, but less than the Coulomb interaction between electrons[43]. In several cases a study of the energy level splittings by E.P.R. has been successful in elucidating the preferred sites of vacancies in the proximity of impurity ions. For these ions the ground state degeneracy in fields of high symmetry is lifted by local field asymmetries caused by vacancy association. The angular variation of the E.P.R. spectra under these conditions reflects the crystal field symmetry at the impurity ion. The fine structure splitting of electronic levels is also sensitive to the surrounding impurity environment by an interaction between identical magnetic dipoles. This usually affects the width of an absorption line and can be neglected in a dilute homogeneous solution.

Impurities are usually incorporated in the melt as di - tri-, and tetravalent ions. The latter two require simultaneous vacancy incorporation, and the configurations of impurity-vacancy centres expected have been discussed earlier. Subsequent oxidation or reduction involves the addition or removal of vacancies to maintain charge equilibrium. More unusual valence states e.g. Fe^{1+}, Ni^{1+}, Co^{1+}, Ni^{3+}, Mn^{4+} [44] have been found to be stabilised in the lattice by u.v., x-ray or γ-irradiation, neutron or electron bombardment, heat treatment or partial charge compen-

sation by another impurity, e.g. Li^{1+}. It is believed that accidental impurity ions, especially iron, play important roles as donors and acceptors in these valence changes during heat treatment.

Information from the spectra of impurity ions can often be obtained from the absorption line width. Three reasons for line broadening are now discussed.

(a) Spin Lattice relaxation.

The line width is a measure of the energy transferred from excited energy levels to the surroundings and depends on the crystal field splitting. For ions with large splittings, i.e. long relaxation times, the observed lines are extremely sharp and narrow in dilute homogeneous solutions, e.g. V^{2+}, Cr^{3+}, Mn^{2+}, Fe^{3+}. However Ti^{2+}, Fe^{2+} have extremely short relaxation times and are observed only at low temperatures. The E.P.R. spectra of these ions were not detected at 77°K, the lowest temperature possible with the equipment available.

(b) Dipolar Interactions.

An interaction between spins of the same kind leads to a line broadening which, for a dilute solution, is indicative of ion cluster formation.

(c) Internal Strains.

An enhanced line width is often observed for ions at sites of crystal field distortions which arise from internal lattice strains.

In contrast to the charge compensating mechanisms in the alkali halides it is established that charge compensation in MgO need only be achieved over relatively large atomic dimensions. Studies of the E.P.R.

spectra of trivalent ions indicate that a large proportion of the sites are in predominently octohedral crystal field symmetry, isolated from cation vacancies.

Data on impurity-vacancy aggregates is most comprehensive for Cr^{3+} ions, where dimers formed by vacancy association in (n.n.) and n.n.n) positions aligned in ⟨110⟩ and ⟨100⟩ directions, designated as $[Cr^{3+}V]_2$ and $[Cr^{3+}V]_1$, have been detected [45]. The existence of $[Cr^{3+}V\ Cr^{3+}]_1$, and $[Cr^{3+}V\ Cr^{3+}]_2$ type centres, formed by the association of a second trivalent impurity ion to an existing dimer, has been proposed to explain more complex E.P.R. spectra[46]. A spectrum in MgO crystals containing titanium impurity ions has been interpreted as a centre of the type $[Ti^{3+}V]_1$, and a more complex background spectra apparent after heat treatments attributed to centres of lower symmetry[47].

The E.P.R. spectra of each of the impurity ions under examination is considered in detail in Chapter 5, together with the effect of heat treatments in both oxidising and reducing atmospheres.

3.3. Optical Properties of Defects

Optical spectroscopy has been an important technique in the study of electron and hole centres in the alkali-halides. It offers a useful method for monitoring both the relative concentration of a defect, with respect to a particular initial state, and the absolute concentration, where an optical absorption band can be calibrated directly by another method and expressed as an oscillator strength.

Less comprehensive optical absorption work has been reported on impurity levels in MgO, mainly concerned with Ni^{2+}, Co^{2+}, Cr^{3+}, V^{3+}, Fe^{2+} and Fe^{3+}. The most prominent absorption bands of crystals containing

these impurities have been attributed to ions in isolated, cubic field, sites, Very little attention has been given to the relatively weak bands which have been assigned to vacancy-impurity complexes.

Information from optical absorption spectroscopy is essential for ionic valence states which are undetectable by E.P.R. techniques.e.g. V^{3+}, for which the level separation is too wide to be observed, and Ti^{3+} in a cubic field, for which the ground state is an orbital triplet.

There is also evidence that precipitate particles can cause attenuation of the transmitted light intensity by both absorption and Tyndall scattering. Optical absorption spectra may be used therefore to detect the presence of second phase particles during heat treatment, which can then be studied in more detail by electron microscopy.

Optical absorption spectroscopy is thus expected to be a less informative method of detecting impurity-vacancy aggregation, and is used in this research as a supplementary technique to E.P.R. to clarify the state of impurities where a complete description by microwave spectroscopy is lacking.

3.4. Direct Microstructural Observation of MgO.

The presence of impurities in commercially available MgO single crystals has been recognised for some time, and studies by electron microscopy have identified the form, dispersion, and composition of precipitates commonly observed in nominally pure crystals.

Second phase particles examined by transmission electron microscopy may be detected by two effects, arising principally from

(a) matrix contrast, caused by lattice strains in the vicinity of coherent particles.

(b) Precipitate contrast, the result of differences in structure factor of the two lattices.

(a) Strain Contrast

For a spherically symmetric strain field around an inclusion, where the precipitate lattice can be derived from a simple dilation or contracti of the matrix lattice, matrix contrast appears characteristically as a pair of fringes, or lobes, situated symmetrically around a line of no contrast, given by the scalar product, $\underline{g} \cdot \underline{R} = 0$

where $\underline{g}$ is the operating diffracting vector, and $\underline{R}$ is the radial displacement around the particle.

Ashby and Brown[48] have computed image profiles for the transmitted and diffracted electron intensity on the basis of this simple misfitting-sphere model. The displacements outside the particle can be described by a factor

$$\varepsilon = \frac{3K\delta}{3K + 2E/(1-\nu)}$$

representing the lattice strain at a point in the matrix, where K is the bulk modulus of the precipitate, E and ν are Young's modulus and Poisson's ratio for the matrix, and δ is the fractional misfit between the two unstrained lattices.

Taking the elastic constants of spinel and MgO to be equal, and $\nu = 1/3$, results in

$$\varepsilon \simeq 2/3\,\delta$$

The image pattern derived from this treatment shows several features useful in determining the minimum detectable particle radius by coherency strain contrast. The image width is found, in particular, to be strongly dependent on the magnitude of the misfit strain and the operating reflection, but is relatively insensitive to the distance of the source of strain from the specimen surface. Near to the specimen surface, (at distances closer than $\frac{1}{2}\xi_g$ where ξ_g is the extinction distance for the imaging reflection) wide asymmetrical images are produced by surface relaxation effects.

An estimate of the limits of visibility of small particles can be made, on the assumption that the lattice mismatch can be completely accounted for as elastic strain energy, and with a knowledge of the extinction distance ξ_g, by using Fig.15 of Ashby and Brown's paper. Here, a parameter $\frac{\varepsilon g r_0^3}{\xi_g}$ is used as a measure of the visibility of spherical inclusions, analogous to the $\underline{g} \cdot \underline{b}$ criterion for dislocation visibility.

The limit of visibility in these calculations is assumed to be reached when the image width, defined by a 10% enhancement of the background intensity, reduces to the particle diameter.

Visibility limits for spinel precipitates in MgO imaged by coherency strain contrast are discussed in detail in Chapter 6.

(b) Structure Factor Contrast.

In addition to strain contrast, a consideration of particle visibility must also include an additional contrast effect due to differences in structure factor, and hence extinction distance, in the two lattices. This results in an effective change in specimen thickness in a column passing through the precipitate particle.

Ashby and Brown[49] have discussed the visibility of particles in terms of structure factor contrast, developing an expression for the maximum intensity change at $S_g = 0$, i.e. at the exact Bragg condition as:

$$\frac{\Delta I}{I} = 2\pi \Delta t \left| \frac{1}{\xi_g^s} - \frac{1}{\xi_g^m} \right|$$

where Δt is the thickness of the inclusion and

$$\xi_g^s \quad \text{and} \quad \xi_g^m$$

are extinction distances for corresponding Bragg reflections in the spinel and matrix lattices respectively.

The parameters ξ_g may be computed from

$$\xi_g = \frac{\pi V_c \cos\theta}{\lambda F_g}$$

where Vc is the volume of a unit cell, θ is the Bragg angle for a reflection g, and λ and F_g are respectively the electron wavelength and structure factor suitably corrected for relativistic effects at 100 kV

$$F_g = \sum_i f_i \, e^{-2\pi i(hu_i + kv_i + lw_i)}$$

where u_i v_i, w_i, are the co-ordinates of an atom in the unit cell with atomic scattering factor f_i.

As a criterion for the visibility of small particles by structure factor contrast, it is assumed that for the minimum change of intensity detectable, $\frac{\Delta I}{I} = 10\%$.

In addition, the visibility of particles may be limited by the resolving power of the electron microscope. A suitable figure for this is probably 7 - 10 Å.

Detailed calculations of extinction distances and minimum visible particle radii are given in Chapter 6.

Venables initially observed impurity precipitates in nominally pure MgO, by transmission electron microscopy, in the form of rod-shaped particles decorating grown-in dislocations, identified by surface electron diffraction with ZrO_2.[50]. Small precipitates showing coherency strains of asymmetric image contrast have also been identified with the spinel lattice $MgAl_2O_4$[51]. Solution treatment at 2000°C was found to drastically decrease both the size and density of precipitates.

The effect of thermal history on the precipitate distribution is further emphasised by work on the etching behaviour of heat treated crystals [41], following a correlation of pyramidal etch features produced by fuming nitric acid with impurity precipitates observed by electron microscopy[52]. The density of surface pyramids on as-grown pure crystals was found to be progressively lowered by anneals at 1500°C, to give a surface denuded zone, indicating that a re-solution mechanism dependent on atmospheric participation was operating.

Large variations in particle size and distribution have also been detected by ultramicroscopy in as-grown crystals obtained from different sources[53]. Several types of precipitate arrangement either decorating dislocation lines or dispersed at random were observed. In particular, a spiked 'hair-pin' type of formation with the long axis along <100> was attributed to a dendritic dislocation climb process concurrent with precipitation. Similar dislocation configurations have been observed by x-ray diffraction topography (54)

A study of the development of dislocation configurations associated with precipitation of vanadium and titanium spinels on ageing at 1200°C has been made by transmission electron microscopy[55]. The nucleation of precipitates of vanadium spinel appeared to be associated with a low density of dislocation loops. Precipitate growth was characterised by the similtaneous growth of the loops into elongated edge dipole configurations, leading eventually to an irregular dislocation network stabilised by large spinel particles. The precipitation of titanium spinel was unaccompanied by a similar dislocation substructure.

Observations on thin foils of commercially pure MgO have detected similar elongated configurations of grown-in dislocations[56], usually decorated by precipitates and presumably formed by the same mechanism.

A study of the distribution and form of precipitate in commercially pure and Zr doped MgO was made by Matkin and Bowen[57]. Precipitates extracted and examined by electron diffraction and electron probe microanalysis were found to be consistent with the pseudo perovskite $CaZrO_3$, containing Ti and Fe in solution, Fe_3O_4, the γ form of Fe_2O_3, the monoclinic form of ZrO_2, and calcia stablized zirconia.

These isolated reports of microstructural observations described here emphasise the need for a systematic study of precipitation in MgO containing one predominant impurity spec ies, in both as-grown crystals and at various stages of annealing over a wide temperature range. The wide range of precipitates and precipitate densities reported for crystals obtained from various sources demonstrates that a study of the ageing behaviour is inconclusive without a simultaneous microstructural study.

3.5. Mechanical Property Measurements

Much of the work on the yielding behaviour of MgO has been concerned with the influence of heat treatment on suppression of dislocation sources. In MgO it is possible to draw a clear distinction between the behaviour of fresh, aged and grown-in dislocations in terms of static and dynamic locking by impurities, demonstrated by the known sensitivity of mechanical properties to the surface condition of as-grown crystals.

As grown crystals polished to remove surface sources are extremely strong and elastic, yielding suddenly at shear stresses of 2000 - 3500 kg/mm^2 [58]. All grown-in dislocations are found to be heavily decorated with precipitate particles, which, it is believed, results in complete immobilisation up to high stresses[59]. The yield stress of crystals containing only grown in sources is found to be increased further by a 2000°C anneal.

The fresh and aged dislocation effects can be most easily discussed in terms of the initiation and propogation of flow as defined by (a) a pinning stress, or the stress required to operate a dislocation source (b) a flow stress, or the stress required for continued dislocation movement.

The characteristic behaviour of grown-in dislocations leads to the belief that two independent static locking mechanisms of aged dislocations operate in MgO[56].

The operation of fresh dislocation sources which normally occurs quite readily at low stresses is restricted by anneals in excess of 600°C[40]. The etch pits associated with dislocations injected prior to these heat-treatments have a different appearance, characteristic of aged disloca-

tions, concurrent with the development of yield drops and jerky flow during initial yielding. This 'weak' locking behaviour, operating predominantly in the temperature range 600 - 1000°C, is identified with a redistribution of impurities onto dislocation lines. Dislocation movement then requires stresses sufficiently strong to detach the dislocation line from its impurity environment.

Similar strain ageing effects in the yielding behaviour of NaCl : Cd^{2+} have been shown to be consistent with impurity-vacancy segregation to dislocation cores[60].

At high temperatures, predominant above 1000°C, a stronger dislocation locking giving rise to a change in ageing kinetics is noticeable, during which dislocations climb and interact to form configurations lying out of the $\{110\}$ slip plane. Such configurational locking is expected to be extremely strong in ionic solids of the rock salt structure, where slip on systems other than $\{110\}\ a/2\langle 1\bar{1}0\rangle$ generates a high energy electrostatic fault[61].

Studies of the propagation of dislocations have been mainly concerned with the microstructural changes accompanying heat treatment of nominally pure crystals. The associated changes of flow stress are the result of a dynamic interaction between dislocations and precipitates or solute impurities. From these studies no clear idea has emerged of the type of obstacle effective in impeding dislocation glide.

The redistribution of impurity in precipitate form by heat treatment, already discussed, has been inferred by many workers to indicate that a precipitation hardening mechanism, responsible for a peak in the flow stress

of commercially pure crystals[40] [62] for isothermal and isochronal anneals between 600 - 1000°C. Heat treatments above this range, up to 2000°C, removes precipitate into solid solution, with a consequently lower flow stress. Nevertheless, it is unlikely that microscopic precipitates of the size considered would be of sufficient density to seriously impede glissile dislocations, and a consideration of the distribution of point defects is also necessary.

Similar suggestions that precipitates are predominant obstacles to glide have been made for doped crystals, especially for iron impurity additions[11][63]. The increase in strength is here attributed to precipitates of the spinel 'magnesioferrite', although no quantitative measurements connecting these obstacles with the flow stress were attempted. Point defect strengthening effects were ignored in these studies. Solid solutions of NiO and MnO in MgO fabricated by impurity diffusion also lead to substantial increases in compressive strength[64] however, and because of the known rapid strengthening of centres inducing anisotropic lattice distortions, such as those formed by impurity ions of different valence state to the host lattice, an account must be taken of impurity-vacancy pairs in any interpretation of the flow stress. An adequate knowledge of the state of aggregation of point defects after heat treatment is especially lacking.

In the research described here the state of aggregation and dispersion of point defects and precipitates has been measured quantitatively by E.P.R., optical absorption spectroscopy and electron microscopy, after various heat treatments. A correlation between these measurements and the flow stress variation has enabled the obstacles effective in impeding

dislocation motion to be more clearly defined for a range of thermal histories.

4. EXPERIMENTAL TECHNIQUES

4.1. Mechanical Tests

4.1.a. Three Point Bend Tests

In the experiments described later many of the flow stress measurements were performed by three-point-bend tests. The yield stress under these loading conditions is determined by the maximum axial stress at the tensile surface. For a beam of length l, width b, and thickness a, this is given in the elastic range, by

$$\tau = \frac{M\, a/2}{I}$$

where M is the moment of the internal stress distribution about the neutral axis, and I is defined as the second moment of the cross sectional area about the bending axis. For a beam deformed in pure bending, the externally applied bending moment is balanced by the internal moment M, so that

$$M = \frac{Wl}{4} \qquad \text{and } I = \frac{ba^3}{12}, \quad \text{where W is the applied load.}$$

The relation between the outer fibre tensile stress, and applied load, is then given by:-

$$\tau = \frac{3Wl}{2ba^2}$$

τ is to be distinguished from $\tau(r)$, which is the resolved shear stress on a {110} plane.

Three-point-bend specimens of approximate dimensions 10 x 3 x 0.5 mms were cleaved from the bulk crystal and polished in boiling orthophosphoric acid at 120°C for two minutes to remove surface microcracks caused by cleaving[65]. Fresh dislocation sources could be produced by sprinkling with 220 mesh silicon carbide powder to inject dislocation loops into the surface. The room temperature bending jig was attached to the compression load cell of an Instron testing machine, and the output

plotted on a high speed recorder giving an optimum load sensitivity of 3 gms. for observations of serrated yielding behaviour.

Tests at higher temperatures were made in air in a silicon carbide resistance furnace, using an alumina bending jig, up to 1500°C.

A jig designed for three-point-bend tests at temperatures down to 77°K is shown schematically in Fig.4.1. The load is transmitted by steel rods to the Instron tension load cell, which pass through slots designed to give a sliding fit to ensure axiality of loading. The jig is operated in an inner metal container filled with isopentane.

A convection current is set up by filling the space between the upper metal wall and the outer dewar with liquid nitrogen contained in a polythene sac. The thermal capacity of the assembly is such that a constant temperature is maintained throughout the interval of a mechanical test. All temperatures were measured using a calibrated copper-constantan thermo-couple.

Although the three-point-bend test is an accurate measure of flow stress as calculated from the elementary elastic beam formula, it has several disadvantages. The number of tests on a given specimen is restricted, and relatively large specimens are required. It is also a much less satisfactory measure of dislocation pinning stresses, since mechanical contact with the loading points provides a source of fresh dislocations, especially at the central loading point on the compression face.

4.1.b. Micro-Hardness Tests

Several authors have used a much more convenient micro-hardness test as a measure of the flow stress of MgO[11],[63],[66] in which the propagation distance of dislocations from a micro-hardness indent is

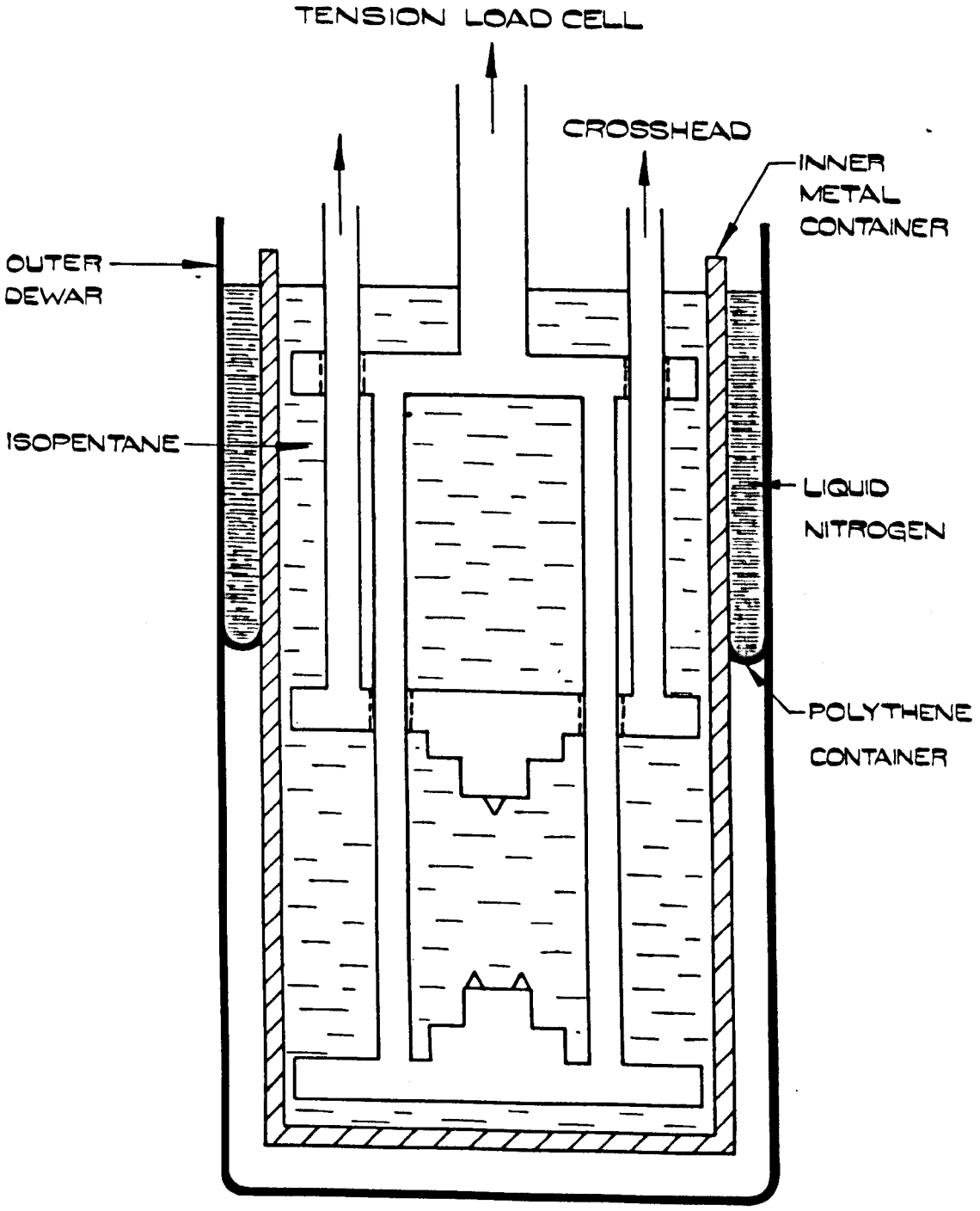

FIG. 4.1

THE LOW TEMPERATURE MECHANICAL TESTING JIG.

taken to be a more sensitive and interpretable measure of the flow stress than the hardness number. The obvious advantage of this method is that a large number of tests can be carried out on smaller specimens. However, the nature of deformation in the small region of high stress concentration around the indent is not clearly understood, and for the research described here a study was made of indentation behaviour which will assist in the interpretation of later results.

Experiments were performed to investigate (a) the relation between wing size and orientation of indenter with respect to the crystal axis. (b) the relationship between wing size and indenter load. The results of (a) are shown in Fig.2.2.

Each point on the graph represents the average of measurements taken from both <110> wings on two separate indents, with 0° representing the situation where the pyramid diagonals are parallel to a <100> crystal direction. At $\pi/4$ intervals from this orientation the measurements can be interpreted in terms of a variation in resolved shear stress on different slip planes resulting in plastic flow away from the indent. At intermediate angles a complicated fine structure is indicated, for which an explanation cannot be easily formulated in terms of dislocation participation, and seems to be evidence for the contribution of fracture processes in absorbing elastic strain energy.

This is confirmed by an examination of the indent at two orientations. Fig.4.3 shows the type of indent produced on a chemically polished MgO surface using a Vickers diamond pyramid at a load of 200 gms. taken with the diamond diagonal (a) parallel to a <100> direction, and (b) rotated by 20°. Both the slip band distribution and <110> fracture paths are extremely regular for 0 and $\pi/4$ orientations. At intermediate

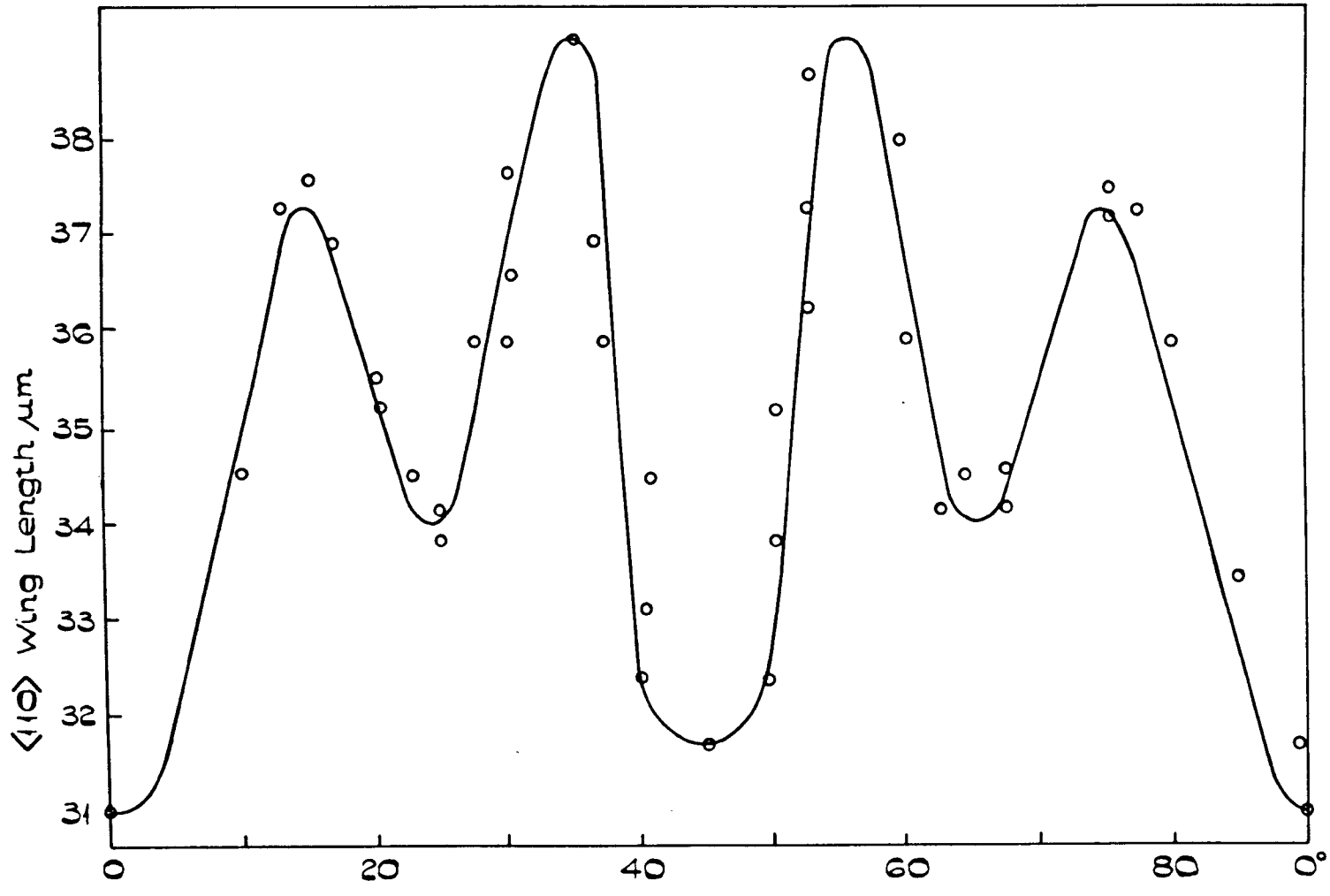

FIG. 4.2

ORIENTATION DEPENDENCE OF THE ⟨110⟩ DISLOCATION BAND LENGTH FOR A LOAD OF 50gm.

angles a complicated fracture pattern is observed with deflections on {100} and {110} planes. The unusual {110} fracture plane observed in the symmetrical orientations appears to be due to a dislocation reaction of the type originally proposed by Keh[67], leading to dislocation pile up along <1$\bar{1}$0> directions.

Experiments performed to investigate the reliability of measurements at different loadings indicate that estimates of flow stress at low loads (5-10gm) could contain a large error, because of a reduction in dislocation mobility close to the surface.

The average stress over the indented area for loads of 5gm and 50 gm of iron doped crystals were calculated, from the respective indent dimensions, to be 750 kg/mm^2 and 195 kg/mm^2. On the assumption that the resolved shear stress on a slip plane is, at a maximum, one sixth of this, the stress supported by each slip plane becomes 125 kg/mm^2 and 32.5 kg/mm^2 respectively. The later value is very close to that calculated from three-point-bend tests.

At high loads, however, the dislocation slip distance become very orientation dependent, and misalignment errors are more important.

From these considerations, loads of 20gm and 50gm were used throughout the tests. For an estimated error in crystal alignment prior to testing of $\pm$ 5°, reference to Fig.4.5. suggests that this would lead to an under-estimate of the flow stress of at most 2 kg/mm^2. Fig.4.4 shows a typical indentation which has been etched for five seconds in concentrated nitric acid at 100°C to reveal the dislocation pattern around the indent. The most prominent features are those of edge and screw dislocation bands extending along <110> and <100> directions

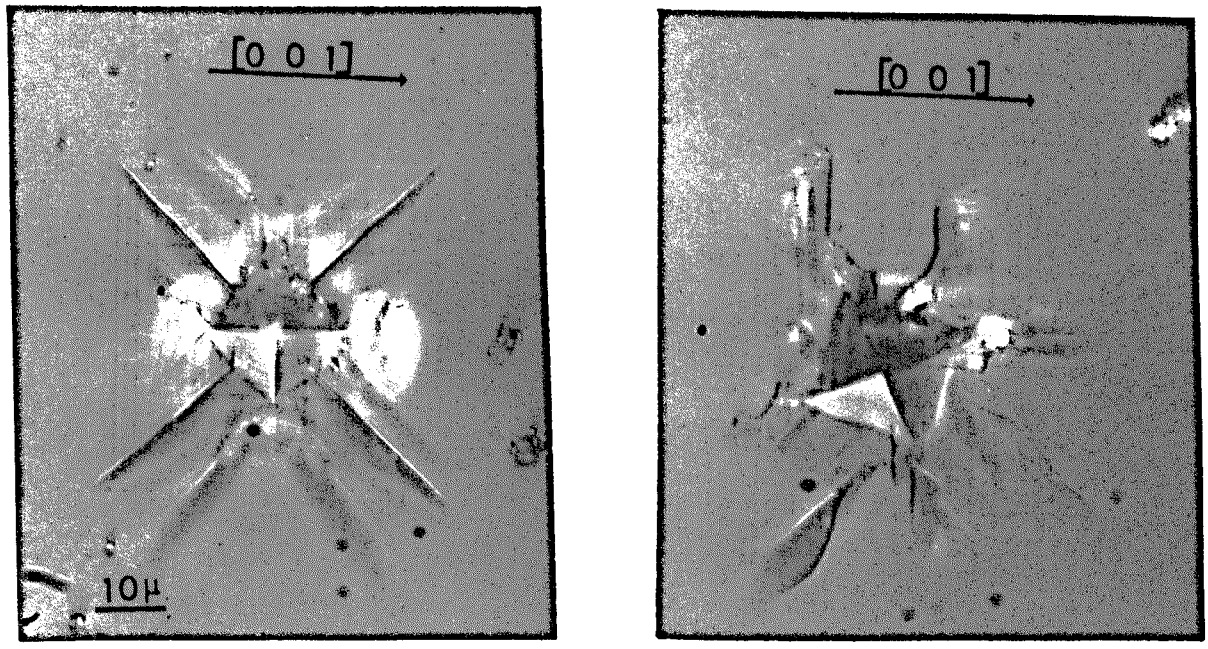

(a) (b)

Fig. 4.3

Microhardness indent pattern for the pyramid diagonal oriented along (a) ⟨100⟩ direction (b) rotated by 20°.

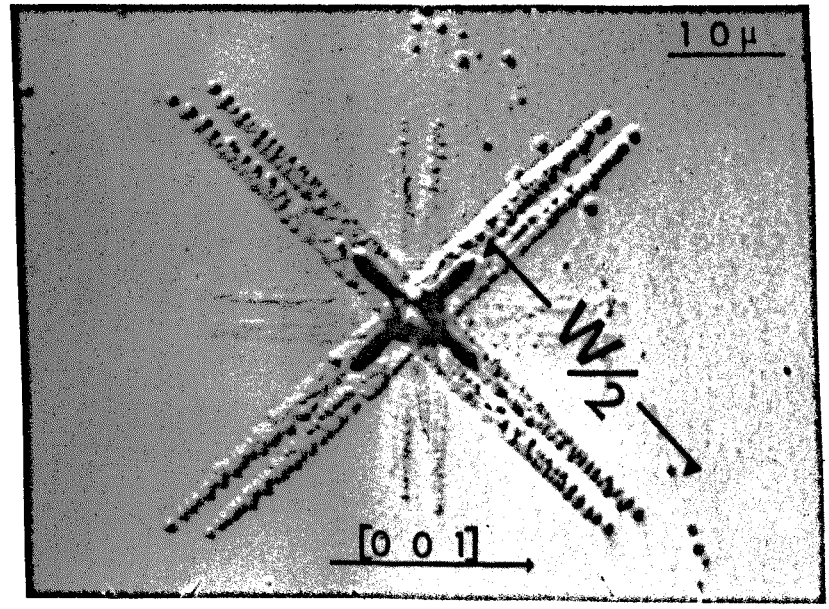

Fig. 4.4.

Method of measurement of wing size (W)

respectively, and cracks along <110> bands. The glide bands are composed of two rows of dislocations of opposite sign corresponding to the two glide directions.

A direct calibration of the edge dislocation band wing size and the flow stress measured in transverse bending was made on a series of crystals of different flow stress and impurity dopant, shown in Fig.5. for a 50gm load. A similar comparison was made for 20gm loading. Previous workers have assumed that the flow stress, given essentially by the mobility of dislocation half loops introduced by the diamond pyramid, shows an inverse proportionality with the measured wing size. It is clear from the calibration curve that a linear range exists, falling off at high and low values, which depends on the concentration and species of impurity ions as a result of differences in work of fracture in each crystal.

This behaviour is evidence that several factors are involved in an interpretation of micro-plasticity.

(a) Plastic flow due to the creation and motion of glide dislocations.

(b) Substantial fracture and the subsequent enlargement and healing of cracks.

(c) An account must also be taken of residual elastic strains in addition to the recoverable strain energy.

An examination of etch pit patterns shows that at low flow stresses, the distribution of slip bands becomes less anisotropic, with screw bands becoming more pronounced. This shows itself in the lower sensitivity of the edge band wing size at low flow stress. At high stresses, crack nucleation and growth is seen to be of increasing importance in absorbing elastic strain energy.

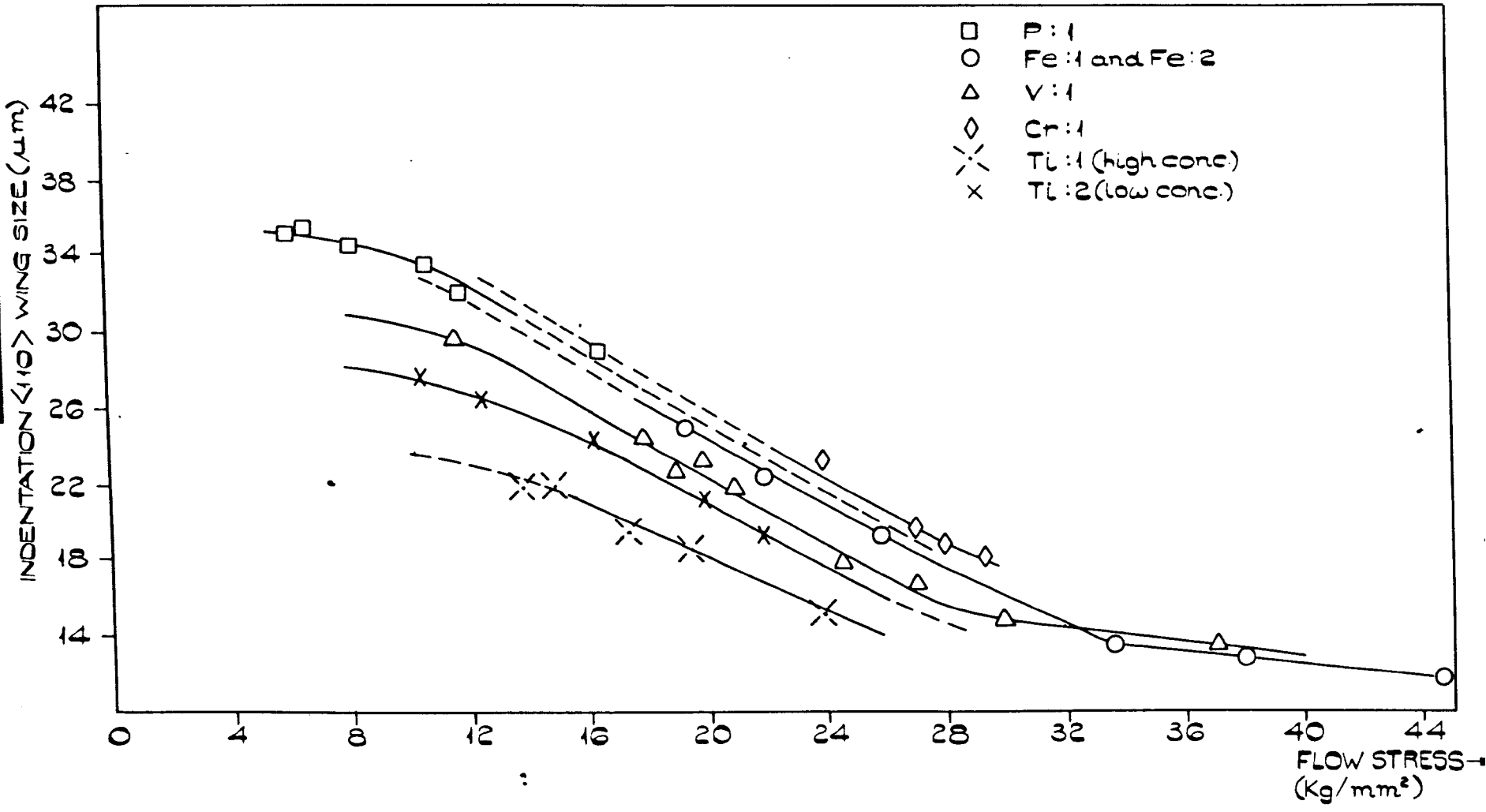

FIG. 4.5

CALIBRATION OF THE INDENTATION WING SIZE AS A FUNCTION OF YEILD STRESS

These measurements are in contrast to those of Davidge[11] who found little significant difference in specimens of different iron concentrations, and a departure from linearity only at low flow stresses.

All measurements in which the flow stress is evaluated from a microhardness test represent an average of eight readings, two on each indentation for loads of both 50 gm and 20gm. After each heat treatment specimens were chemically polished to remove several microns from the surface. A direct comparison was then possible with the outer fibre tensile stress determined by three-point-bend tests.

As far as possible, with the availability of large crystals, direct measurements of the flow stress were made in transverse bending, especially at important points on ageing curves. Estimates from micro-hardness tests were only utilised at intermediate points to complete the form of the curve.

4.1.c Compression Tests

In a few cases the results of three-point-bend tests were checked by loading bulk crystals in compression. These specimens were cleaved from the parent crystal to typical dimensions 3.5 x 3.5 x 5.0 mms. In order to avoid cracking, axiallity of the two compression surfaces was maintained by using a jig consisting of a steel hemisphere between the specimen andlower load cell, and a ball and socket joint at the upper surface.

4.2. Specimen Preparation for Electron Microscopy

Initially specimen preparation was carried out by the technique of Washburn et. al[68] in which a jet of boiling acid is directed onto a thin slice of MgO until perforation occurs. Small areas are then detached from the edges of the perforation for examination. A more convenient technique was subsequently employed using a P.T.F.E. holder.

Cleaved specimens of approximately 0.5 mm thickness were cut ultrasonically into discs of 3.3 mm diameter, fitted into a P.T.F.E. holder, and chemically polished in a gentle stream of hot acid at 120°C. using an inverted funnel with cuts around the circumference (Fig.4.6.). When perforation occurred the specimen was quickly removed, washed in hot and cold water, rinsed in methanol and mounted in the electron microscope specimen holder. All micrographs presented in the text show sections taken from {100} specimens. Samples prepared by this method had the advantage of being mechanically stronger, and requiring a smaller quantity of as-grown crystal. Problems were encountered, however, from electrostatic charging effects in the electron beam.

The specimens were examined in a JEM 7 electron microscope fitted with a large angle goniometer stage.

4.3. Specimen Heat Treatment

Heat treatments up to 1500°C were made in air in a horizontal alumina tube, platinum wound furnace, or in a reducing atmosphere in an alumina tube, silicon carbide element furnace. In each case temperature measurements were made with a Pt/Pt-13% Rh thermocouple. Solution treatments at 2000°C were carried out in an induction furnace under an argon atmosphere.

FIG. 4.6

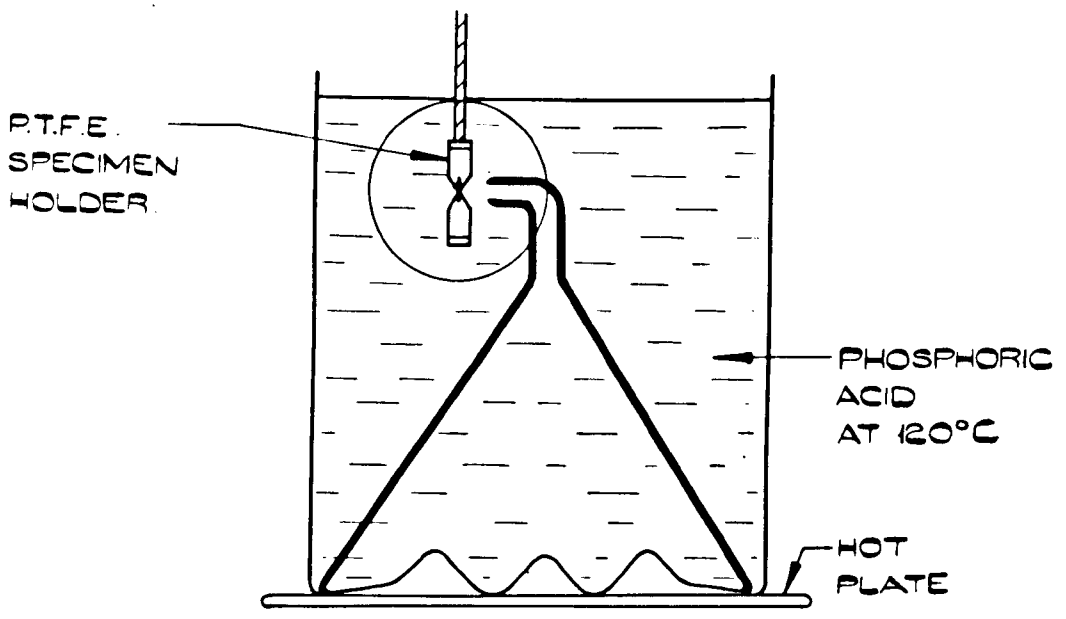

(a)

POLISHING APPARATUS FOR ELECTRON MICROSCOPE SPECIMEN PREPARATION.

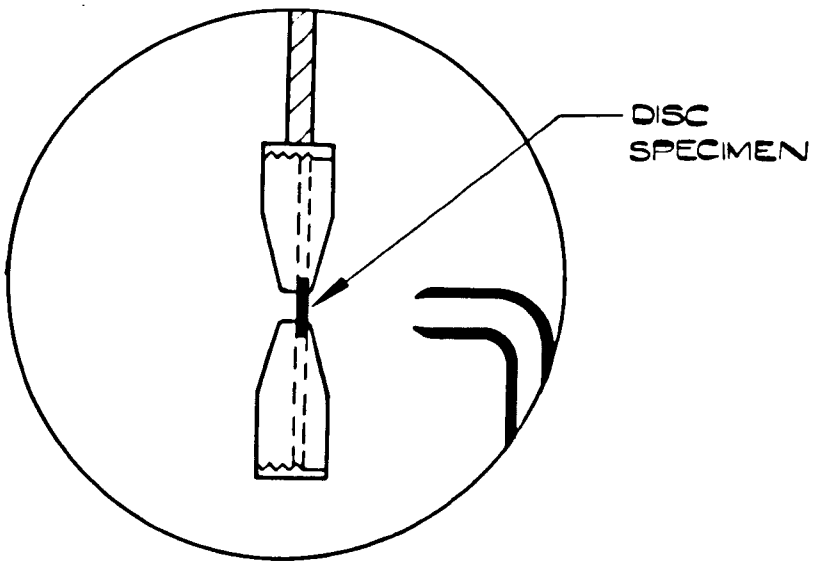

(b)

ENLARGED VIEW OF SPECIMEN HOLDER SHOWING THE ACID STREAM DIRECTED ONTO THE CRYSTAL FACE AND THE METHOD OF MOUNTING THE DISC IN THE HOLDER.

4.4. Optical Spectroscopy

Infra-red, optical and u.v. absorption spectra over the wavelength range 200 mμ - 24 μ were studied using a Perkin-Elmer 450 double beam spectrophotometer. Measurements of the high absorbance values below 4000 Å were made from platelets mechanically and finally chemically polished to a thickness of 0.005 cms.

4.5. Electron Paramagnetic Resonance Measurements

A Decca X-3 spectrometer operating at 9270 MHz with 100 kHz field modulation was used to monitor the E.P.R. signal of impurity ions in MgO samples. Specimens were cleaved from the same region of the parent crystal block to consistent dimensions to ensure a uniformity of impurity distribution and a constant filling factor in the spectrometer microwave cavity. This had the advantage that the signal from specimens after heat treatment could be directly compared. Except for a pre-calibrated gain control all spectrometer settings were identical. Field sweeps were performed both at room temperatures, and at liquid nitrogen temperatures using a quartz cold finger which extended into the cavity. Orientation effects in each case were investigated using a P.T.F.E. goniometer.

5. THE EFFECT OF HEAT TREATMENT ON THE FLOW STRESS OF DOPED MgO.

5.1. Introduction

In this chapter it is intended to examine in detail the changes in flow stress induced by a wide range of heat treatments, for crystals each containing a single major impurity, in order to isolate the characteristic features of the strengthening phenomena caused by each ion species separately. A concurrent study over selected temperature ranges is also made of the state of the impurity in solid solution by E.P.R. and optical absorption spectroscopy, and of visible microstructural changes by electron microscopy. On this basis it is possible to identify each feature of the ageing behaviour with a particular defect.

For convenience these observations are listed under the headings of the predominant impurity. To avoid repetition, where a mechanism is believed to operate in two systems, it will be fully discussed in the earlier section and referred to more briefly in the latter.

5.2. Iron

Two crystals were selected for study: - Fe : 1 containing 900 p.p.m. iron, and Fe : 2 doped to a level of 7,500 p.p.m. Because of the marked differences in behaviour the results for each crystal are presented separately, followed by a complete discussion.

5.2.a. Flow Stress Variations for Fe : 1

The effect of isothermal and isochronal heat treatments in air on the flow stress of as-grown crystals is shown in Fig.5.1 (a) and (b). (The isothermal results are drawn on a semi-logarithmic plot).

For ageing temperatures up to 1,400°C the flow stress initially decreases below the as-received value, reaching a minimum after 1 hour at 1,000°C. Following this temporary softening, the flow stress recovers, reaching a maximum after 70 hours at 800°C and thereafter exhibiting an overaged

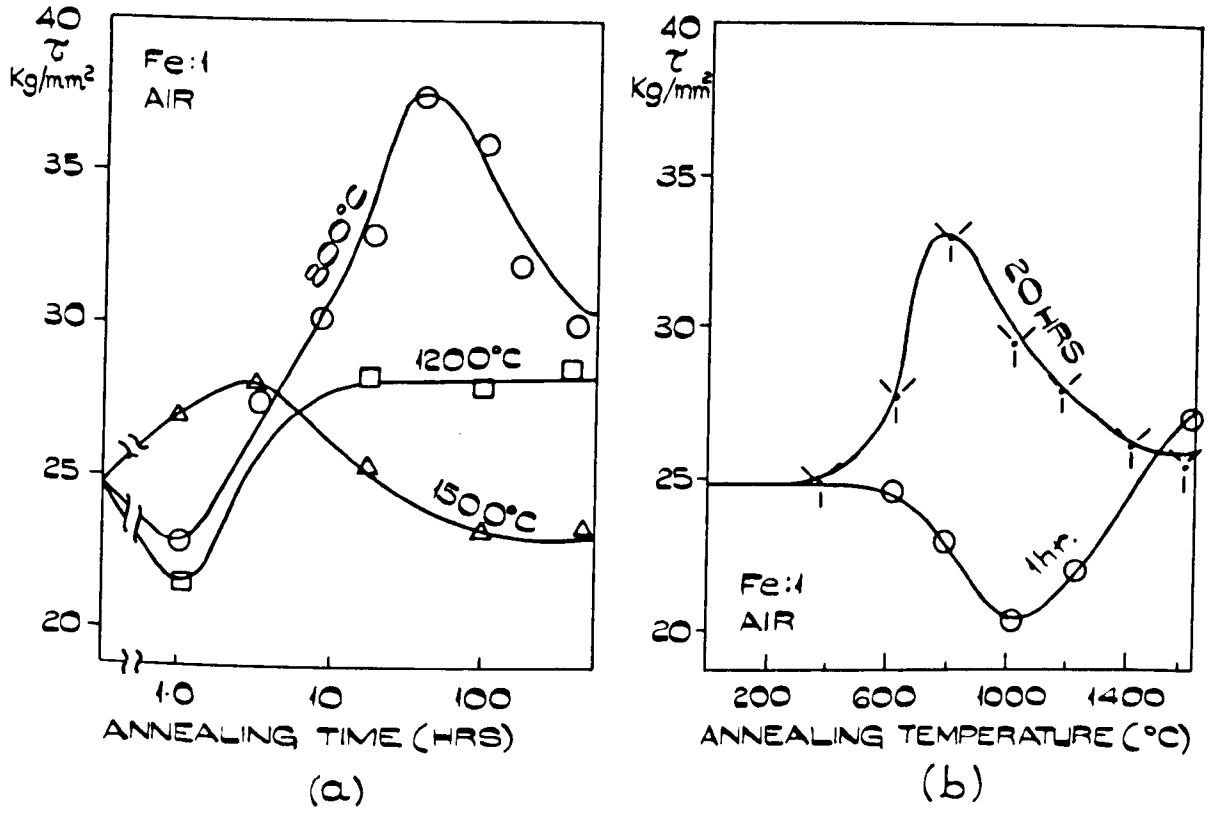

FIG. 5.1

ISOTHERMAL AND ISOCHRONAL ANNEALS FOR CRYSTAL Fe:1.

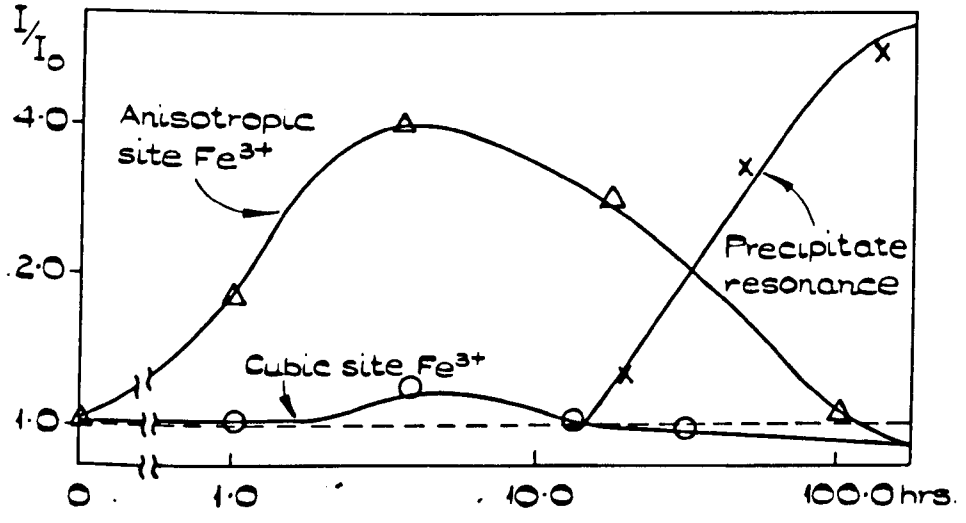

FIG. 5.2

THE RELATIVE INTENSITY VARIATIONS (I) OF (1) SINGLE Fe^{3+} IONS (2) CLOSE-PAIRED IMPURITIES AND VACANCIES (3) Fe^{3+} IONS IN THE SPINEL PRECIPITATE LATTICE EXPRESSED AS A RATIO TO THE INITIAL INTENSITY I_0.

behaviour, returning after long ageing times at 800°C to a value not far removed from the initial hardness.

Above 1,200°C, air anneals have the effect of causing a more pronounced increase in flow stress, showing a distinct maximum and subsequent decay after relatively short ageing times.

5.2.b. The E.P.R. Spectra of Fe : 1

The E.P.R. spectrum of Fe^{3+} ions in cubic site symmetry is well established[69], consisting of a symmetrical quintet of lines. The central line in this group is of much greater amplitude and a very convenient measure of the Fe^{3+} concentration. The spectrum of divalent ions has also been observed at 4°K as a narrow (10gauss) line, and a very broad (450 gauss) line which has been attributed to lattice strains around the ion site[70]. Facilities were not available for E.P.R. studies at liquid helium temperatures, however, and the presence of divalent iron is surmised from a determination of the absolute concentration of Fe^{3+} ions using a standard E.P.R. sample as a comparison.

In the full field sweep spectrum of Fe : 1 reproduced in Fig.5.3(a) only the three most prominent lines of the Fe^{3+} quintet are resolvable against background noise at 77°K. It is observed that in addition to these lines, other lines are also present showing an orientation dependence consistent with vacancy association in (n.n.) or (n.n.n.) configurations[11]. Only a small proportion of the total iron content is associated with vacancies in close-paired configurations.

The effect of annealing is not shown directly in Fig.5.3. for Fe : 1 but absorption lines similar to those presented in (b) and (c) for Fe : 2 are observed for Fe : 1 to be correspondingly less intense.

Fig.5.2 illustrates the variation in intensity of the lines associated with Fe^{3+} ions in Fe : 1 on ageing at 800°C. The line attributed to simple

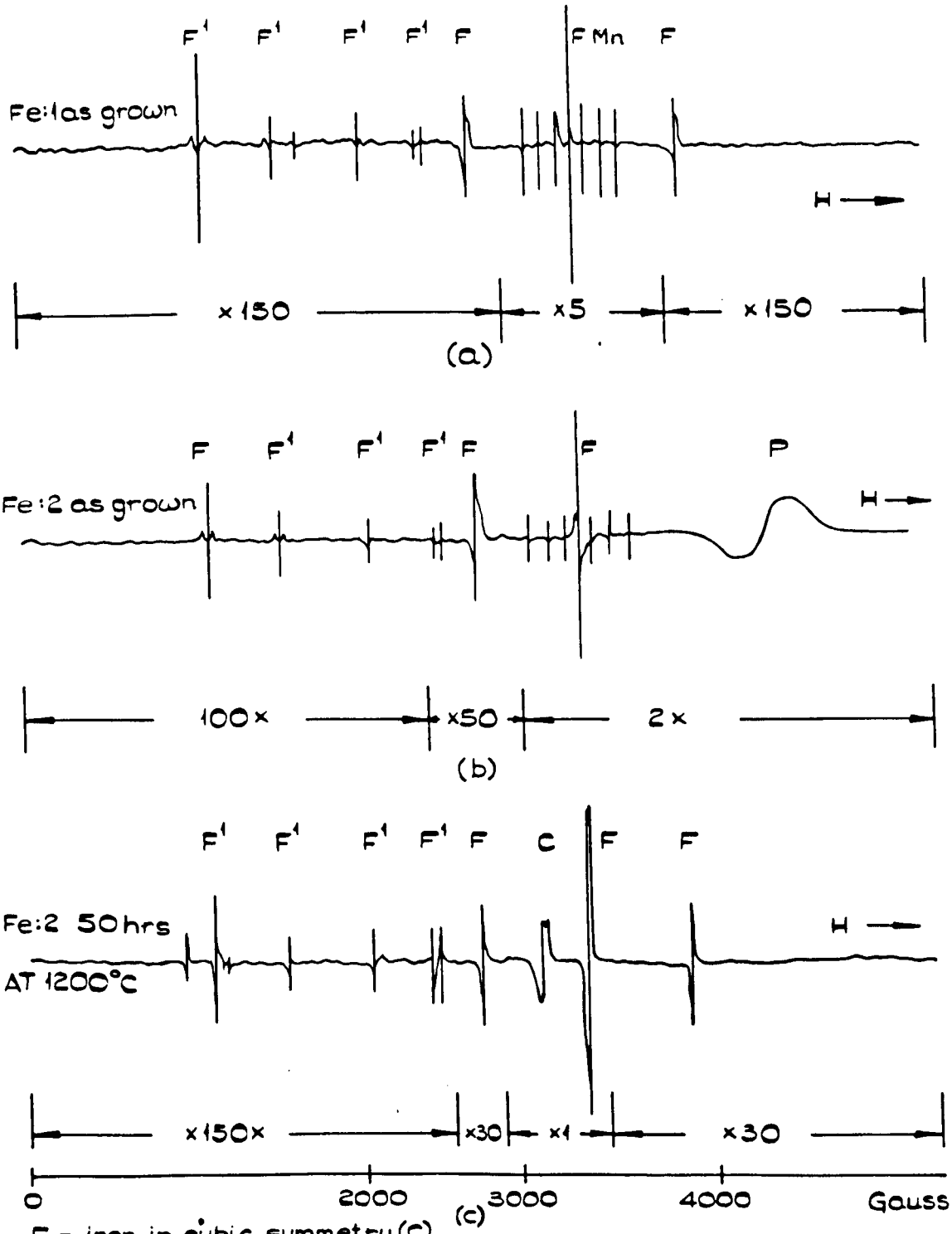

F – iron in cubic symmetry (C)
F¹ – iron in sites of lower symmetry
P – iron in the spinel precipitate $MgFe_2O_4$
C – unknown cluster appearing at high temperatures in air
other lines are due to substitutional Mn^{2+} ions as accidental impurity

FIG. 5.3
E.P.R. SPECTRA OF FE^{3+} IONS IN Fe:1 AND Fe:2.

impurity ion - vacancy dimers is particularly affected, rising to a maximum after 5 - 10 hours, and decaying after that time. A similar, but less marked behaviour is shown in the intensity of the line due to isolated Fe^{3+} ions. The source of extra ions in these oxidising conditions is assumed to be ions pre-existing in the divalent state.

After 15 - 20 hours the growth of another line is detected at high magnetic fields, similar to the line shown in Fig. 5.3.(b), and is attributed to Fe^{3+} ions in a precipitate lattice. This line grows rapidly, corresponding to the decrease in density of ions in other sites. Identification of the line with Fe^{3+} ions in spinel precipitate form is discussed in section 5.2.f No similar line is observed for anneals above 1,000°C in air. Instead, the concentration of ions in asymmetric sites is observed to decrease slightly, corresponding to an increase in isolated Fe^{3+} ions and the appearance of a line slightly lower in field to the central Fe^{3+} line as shown in Fig. 5.3.c and discussed further in 5.2.f.

5.2.c. The Optical Absorption Spectra of Fe : l.

The form of iron in solid solution in crystal Fe : l may also be monitored by the optical absorption spectra of crystals in the u.v., visible and infrared, as shown in Fig. 5.4. The spectra of reduced crystals is featureless, apart from some absorption in the far u.v. In both the as-grown condition, and the oxidised state a number of other bands are observed, many of which are identifiable with particular defects. Two bands at 2,100 Å and 2850 Å have been associated with the presence of Fe^{3+} in solution as single ions in cubic site symmetry[71]. Other bands are also resolvable at longer wavelengths in as-grown crystals, and after anneals at 1,200°C, at approximately 4570 and 5250 Å. No assignment of these bands has been reported, but it is believed that they are caused by local crystal

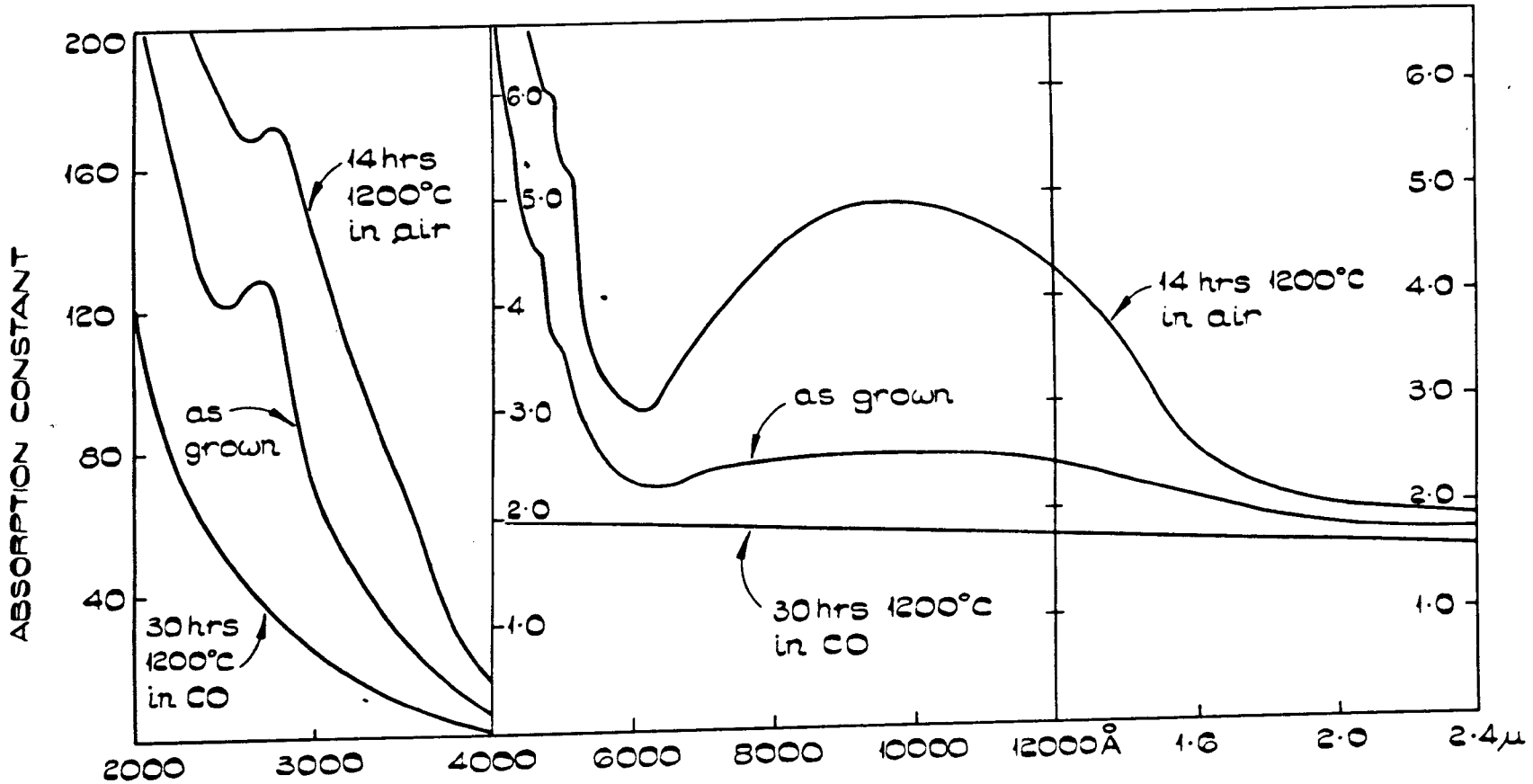

FIG. 5.4

OPTICAL ABSORPTION SPECTRA FOR CRYSTAL Fe:I

AFTER THREE HEAT TREATMENTS.

field asymmetries at an Fe^{3+} ion site due to vacancy association[11]. A broad band centred on 9,500 Å is also evident in the as-grown crystal, becoming more prominent after ageing at 1,200°C in air. This band is not caused by Fe^{3+} ions in spinel precipitate form, since at this temperature the system is in the solid solution phase field (Fig. 2.2.) and, in addition, the intensity is reduced by re-ageing at a lower temperature at which spinel precipitation is expected. In a previous study a tentative identification was made with a cluster of Fe^{3+} ions and vacancies[11], but in the light of the discussion in 5.2.i, and the confirmation of the existence of interstitial oxygen in as-grown and aged crystals described in 5.4. and 5.5., the band is ascribed to a modification of the symmetry at isolated Fe^{3+} ion sites by associated interstitial oxygen ions.

5.2.d. Microstructural Observations

The stages of microstructural development observed in the electron microscope (Fig.5.5.), show a dependence on the depth of the electron microscope specimen from the surface of the initial cleaved and aged section, but no precipitation was ever observed in as-grown crystals.

The main features in the initial period of ageing at 800°C (10-20 hours) is that of a low density of small prismatic loops. A low density of platelet and needle shaped precipitates also develop simultaneously, with edges parallel to ⟨110⟩ and ⟨100⟩ matrix directions.

For longer ageing times (40-60 hours) a higher density of features are noticeable which after further ageing are resolvable as dislocation loops associated with a low density of needle precipitates. Analysis of the nature of the loops has established them to be of vacancy type.

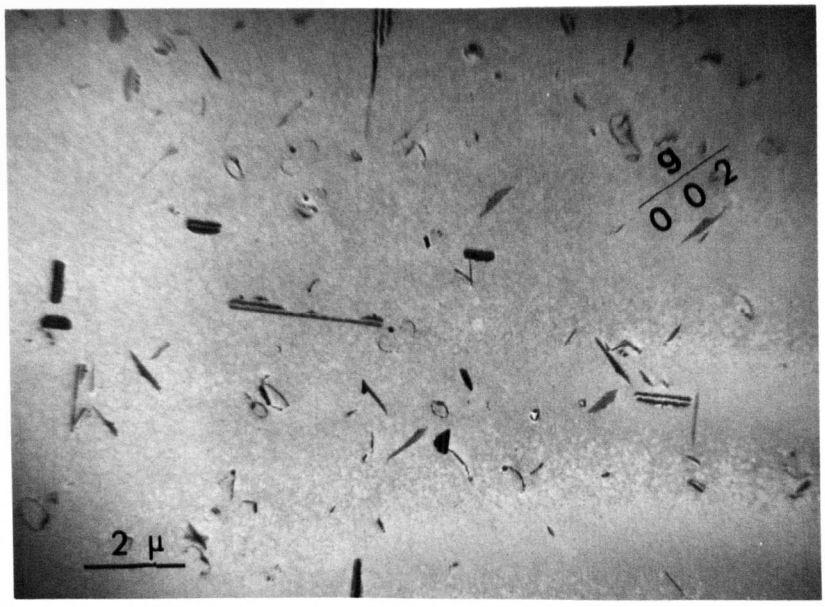

Fig. 5.5.(a)

Fe : 1 aged for 20 hours at 800°C in air.

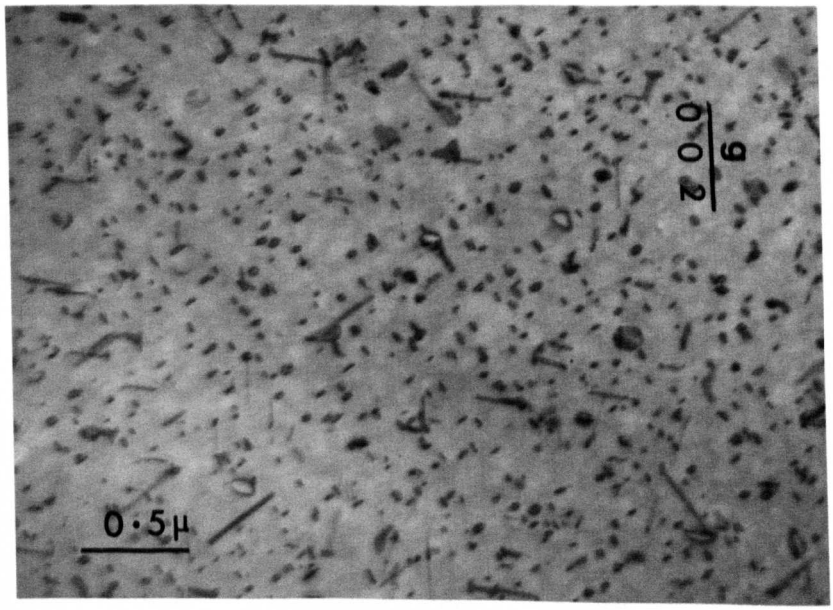

Fig. 5.5.(b)

Fe : 1 aged for 60 hours at 800°C in air.

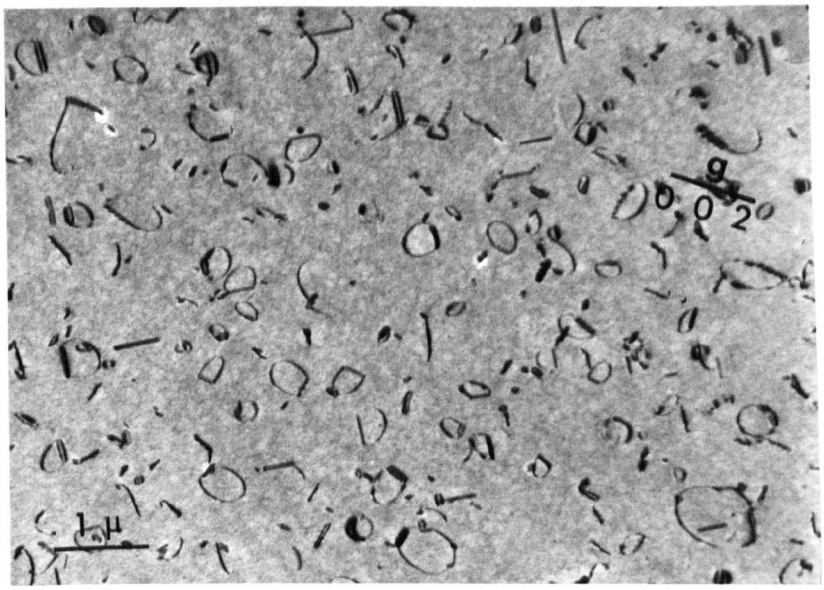

Fig. 5.5.(c)

Fe : 1 aged for 150 hours at 800°C in air.

Loop growth proceeds rapidly by further vacancy condensation at the expense of the loop density, and by the formation of attractive interactions between growing loop segments. Many of the loop segments after 100 hours appear to be anchored by irregular rod-shaped precipitates so that, as a result, a fairly high loop density is retained in the crystal even for anneals in excess of 400 hours. At this annealing stage precipitates showing coherency strain contrast are observable, but the volume fraction of precipitate is not sufficient for identification with the spinel $MgFe_2O_4$ by electron diffraction. The irregularly shaped precipitates, in the absence of detectable precipitate diffraction spots, are believed to be Fe_2O_3. Precipitates of similar form have been extracted from undoped crystals and found to be consistent with this structure[57].

No precipitation was detectable for temperatures above, 1,000°C, as expected from the solid solubility limit for this system[13].

5.2.e. Flow Stress Variations for Fe : 2.

The effect of heat treatment in air on the flow stress of Fe : 2 is illustrated in Fig. 5. 6. The behaviour at this impurity level shows some striking differences to that of Fe : 1.

Two hardness peaks are seen on the isochronal annealing curve, at 600°C and 1,200°C. The expected peak hardness at 800°C is completely absent. At 1,200°C the flow stress may be increased by a factor of two by ageing treatments, reaching a maximum value after 100 hours.

5.2.f. The E.P.R. Spectra of Fe : 2.

An indication of the state of iron impurities in Fe: 2 is given by the E.P.R. spectra shown in Fig. 5.3 (b) and (c). In the as-grown state the lines assigned to simple vacancy-impurity clusters are very

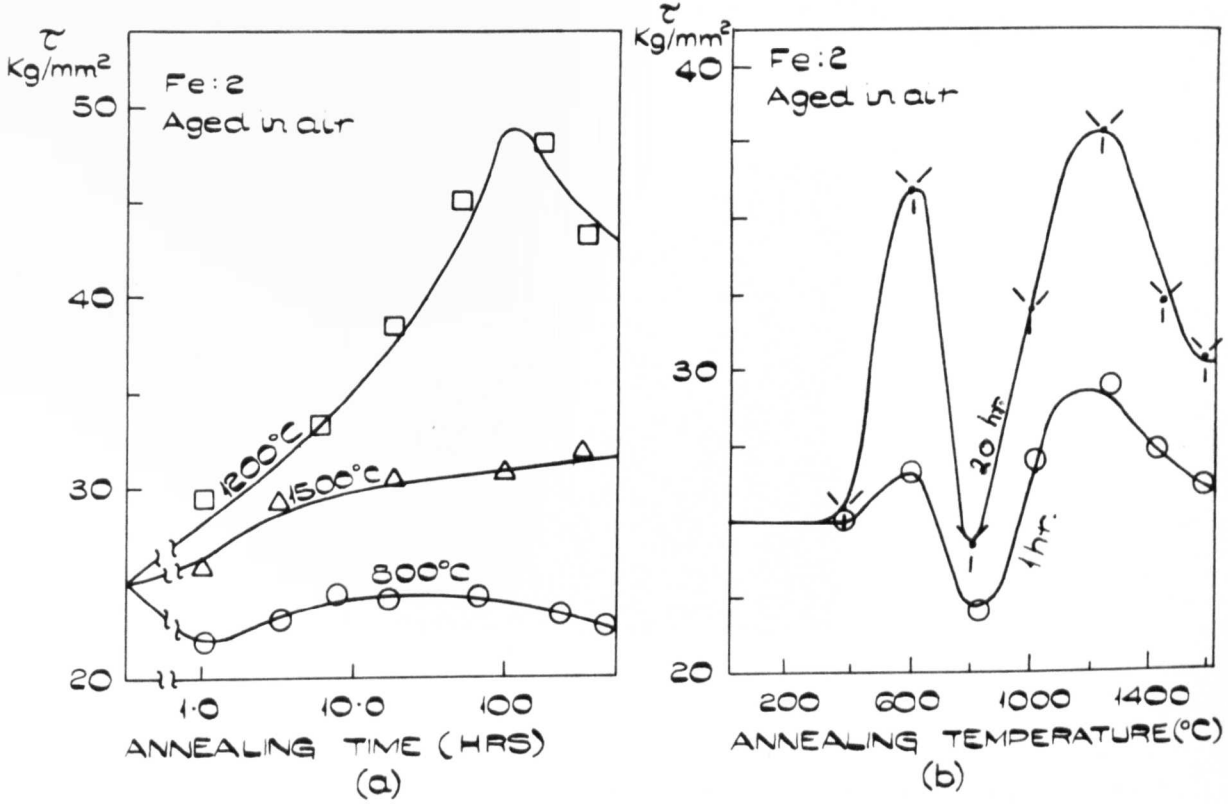

FIG. 5.6

EFFECT OF HEAT TREATMENT ON THE FLOW STRESS OF CRYSTAL Fe:2.

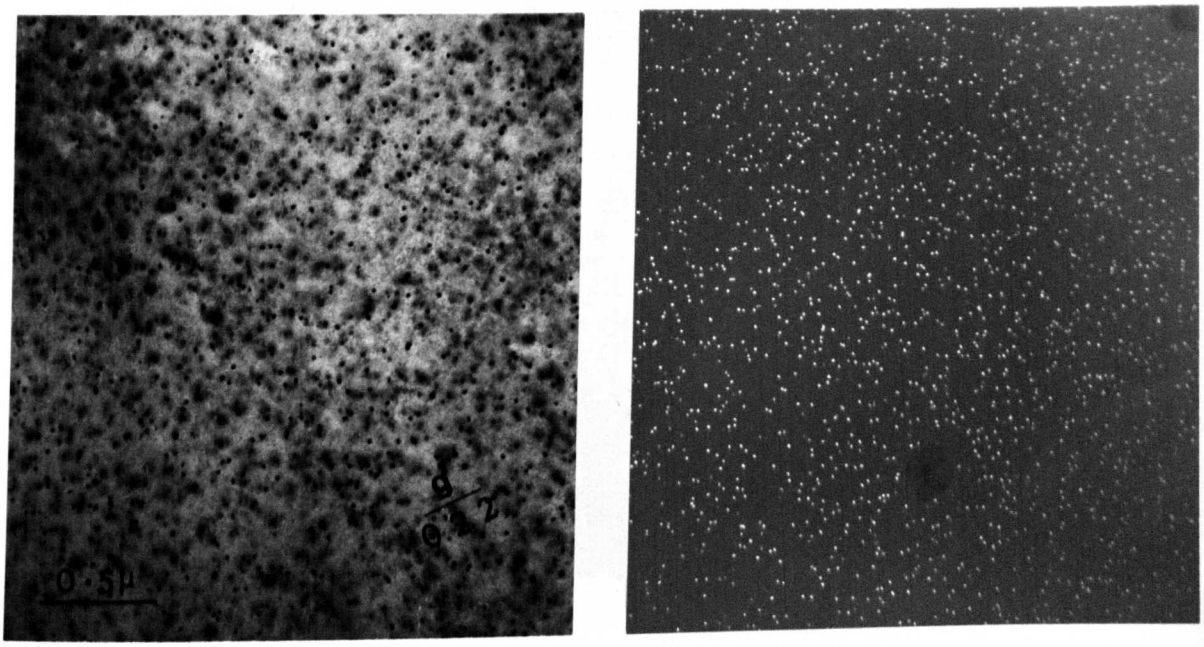

FIG. 5.7

$MgFe_2O_4$ SPINEL PRECIPITATES IN Fe:2 AGED FOR 800 HRS. AT 450° C IN AIR (a) BRIGHT FIELD IMAGE (b) THE SAME AREA IN DARK FIELD USING ONE OF THE REFLECTIONS DUE TO THE SPINEL PRECIPITATE PARTICLES.

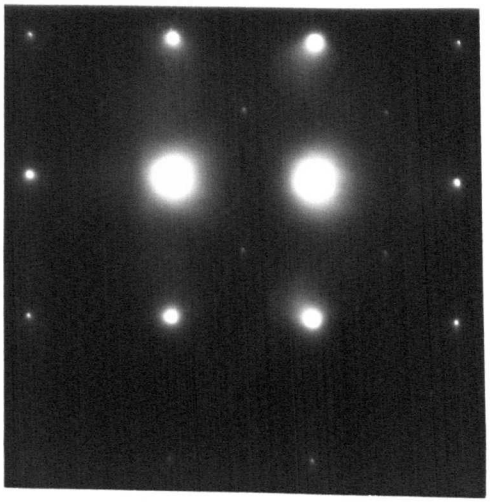

Fig.5.7.(c)

Electron diffraction pattern showing spots due to spinel precipitate $MgFe_2O_4$ (arrowed) and MgO matrix spots.

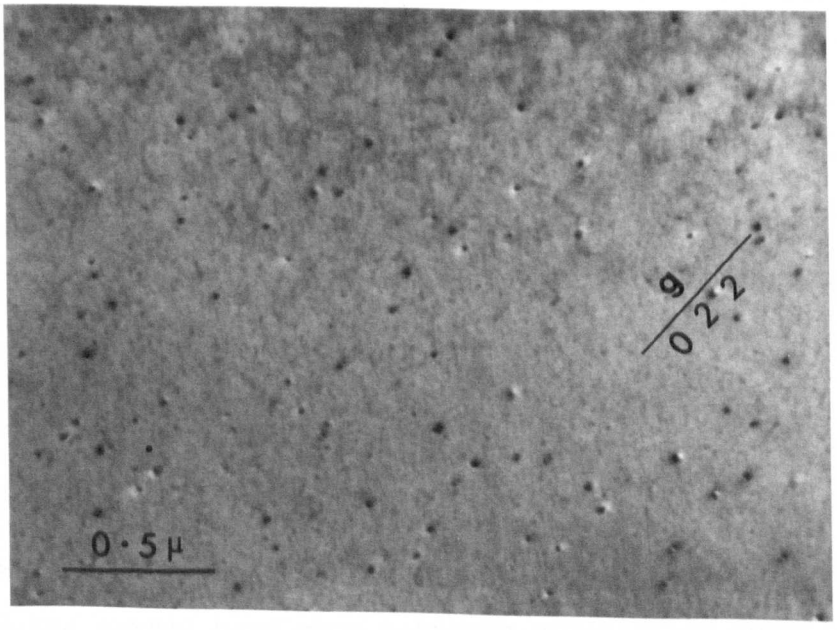

Fig. 5.7.(d)

$MgFe_2O_4$ precipitates showing coherency strain contrast in an Fe : 2 specimen aged for 70 hours at 800°C in air.

weak compared to the predominant lines due to single Fe^{3+} ions and the wide line appearing at high fields. The latter line has already been identified with Fe^{3+} ions in the spinel precipitate structure.

A confirmation of the origin of the precipitate line is provided by its behaviour under heat treatment. For 800°C anneals in air the intensity and line width of the absorption increases dramatically, while heat treatments in air above 1,000°C or in a reducing environment remove the line completely from the spectrum. Further evidence is provided by the orientation dependence of the line width and g-value of the line. The ion spinel $MgFe_2O_4$ structure is of an intermediate form (Table 2.1) in which a proportion of the Fe^{3+} ions are distributed over tetrahedral sites in the oxygen sublattice. Rotation of crystals in the microwave cavity about a cube axis is found to shift the g-value and line width as expected for ions in sites of this co-ordination symmetry, giving coincident symmetry points at 0° and $\pi/2$, $\pi/4$, and $3\pi/4$ orientations with respect to the static magnetic field H_o.

The resolution of precipitates on heating above 1,200°C in air is accompanied by the formation of another line, illustrated in Fig. 5.3 (c), at a slightly lower field than the central line of the Fe^{3+} quintriplet. Although the g-value of this line is insensitive to the static magnetic field orientation, a number of fine structure lines centred on the parent band show a strong orientation dependence.

An assignment of this line is made from the inference of previous investigations, and the observed effect of heat treatment. A method of charge compensation involving interstitial oxygen has been

proposed by other workers on the basis of sharp line luminescent spectra in chromium doped crystals[72]. An E.P.R. signal from an impurity centre concluded to be comprised of interstitial oxygen has also been reported for nominally pure crystals[44]. The appearance of the line in Fe : 2 and Fe : 1 associated with the broad optical absorption band commented on earlier, is enhanced by anneals in air above the solid solution phase boundary, and rapidly decays in a reducing environment. The configuration responsible for this line is therefore proposed to be that of interstitial oxygen symmetrically surrounding an Fe^{3+} site.

5.2 g Microstructural Observations.

The presence of a spinel precipitate dispersion, indicated by the E.P.R. signal of Fe ; 2 crystals is undetectable in the electron microscope in as-grown crystals and up to annealing times corresponding to the overaged state. A development of this precipitate dispersion is shown in Fig. 5.7 (a) and (b) after 800 hours at 450°C in air, and is presented as a bright field - dark field pair of micrographs with the dark field picture taken using one of the reflections associated with the spinel structure as shown (c). The precipitate is hence identifiable with the spinel structure $MgFe_2O_4$, with axes parallel to those of the matrix. The volume fraction of precipitate after this treatment was determined, by counting the size and density of particles falling within a random area, to be 8.0×10^{-4}.

At 800°C precipitates are resolvable after 70 hours, as shown in Fig 5.7 (d). A dispersion of precipitates, identified with the spinel structure, is observed, many of which are imaged by coherency strain contrast. Above 1,000°C no precipitate of resolvable size are detectable.

5.2.h. Effect of Atmosphere on the Annealing Behaviour of Fe : 1 and Fe : 2.

The decay in E.P.R. signal from isolated Fe^{3+} ions, Fe^{3+} - vacancy centres, and precipitates in Fe : 1 and Fe : 2 on reduction in CO is illustrated in Fig. 5.8 (b) and (c). The intensity of these signals falls rapidly over an initial period, and subsequently decays less rapidly as larger clusters and precipitates revert to solid solution as Fe^{2+} ions.

The effect of the disappearance of these centres on the flow stress is represented in Fig. 5.8 (a) and shows a similar form - an initial rapid softening as low order clusters are reduced, followed by a more gradual regime as reduction of larger centres occurs. On reageing crystals of Fe : 2 at 1,200°C in air, (Fig. 5.8 (d)) the flow stress recovers rapidly above its as-grown value, then decays. A similar behaviour is shown at 800°C, with a flow stress peak occurring after 100 hours. The recovery at 1,200°C is characterised by a rapid increase in the proportion of trivalent ions, and is attributed to both reformed Fe^{3+} - vacancy pairs and to interstitial oxygen rediffusion. At 800°C, however, the optical absorption due

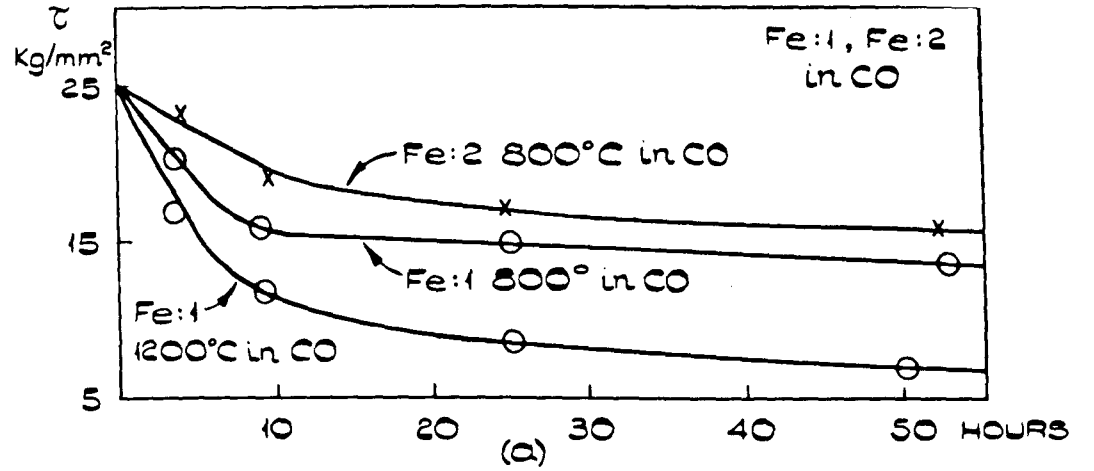

(a)

FLOW STRESS VARIATIONS FOR Fe:1 AND Fe:2 IN REDUCING (CO) ATMOSPHERES

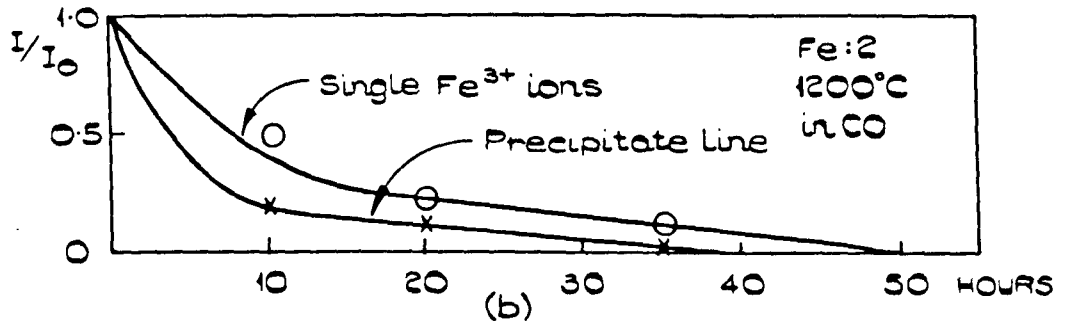

(b)

THE VARIATION IN E.P.R. LINE INTENSITY IN CO FOR Fe:2.

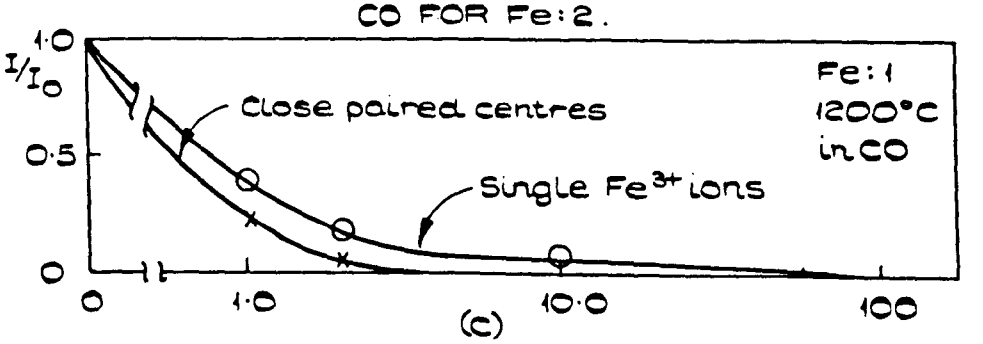

(c)

THE VARIATION IN LINE INTENSITY IN CO FOR Fe:1

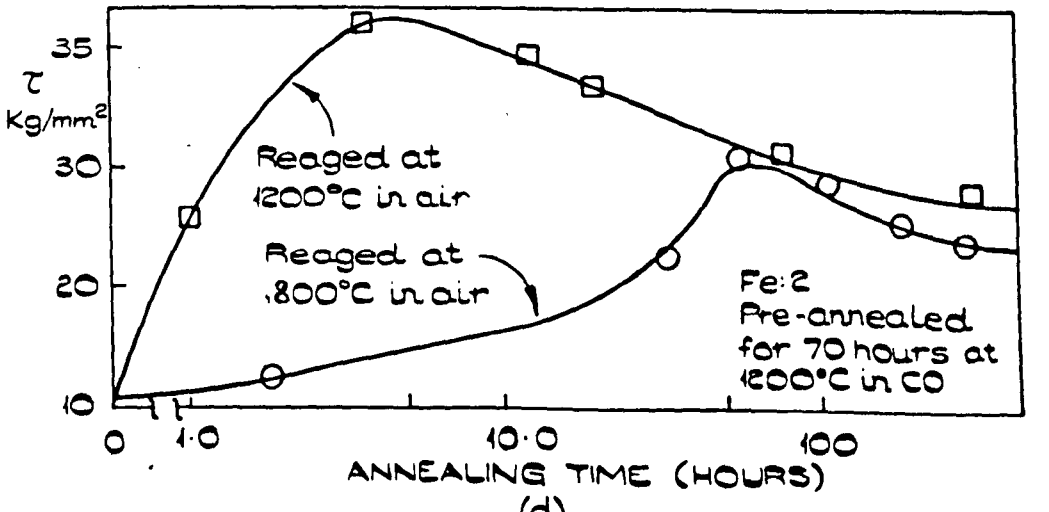

(d)

RECOVERY OF THE FLOW STRESS FOR Fe:2 AFTER A REDUCING TREATMENT OF 70 HOURS AT 1200°C IN CO.

FIG. 5.8 EFFECT OF ATMOSPHERE ON THE ANNEALING BEHAVIOUR OF Fe:2, Fe:1

to Fe^{3+} ions is very small, even after 100 hours, and the flow stress recovery at this temperature is therefore attributed to a precipitation hardening - overageing phenomenon. Precipitate particles are not resolvable up to 200 hours, and it is concluded that the particle dimensions at peak hardness are below the limit of resolution in the electron microscope.

5.2.i Correlation of E.P.R., Optical Absorption and Microstructure for Fe : 1 and Fe : 2

The E.P.R. spectrum of Fe ; 1 crystals indicates that, in the as-grown state, only a fraction of trivalent ions are associated with vacancies, the majority being in solution in essentially octohedral crystal fields in the di-or trivalent state. From a determination of the absolute concentration of Fe^{3+} ions by E.P.R., using a standard graphite sample containing a known number of free spins, the concentration of Fe^{3+} ions is estimated to be 600 p.p.m. The remaining 300 p.p.m. of the total, chemically determined, concentration is assumed to be in the divalent state.

On ageing at 800°C it is the appearance of a new line attributed to the formation of a precipitate lattice, and not the enhanced Fe^{3+} solid solution lines caused by oxidation, which can be correlated with a corresponding flow stress increase.

The effect of the ageing treatment is attributed to the formation of a precipitate lattice from isolated ions by a sequence of the form:- Isolated ions ⟶ Simple Impurity - Vacancy Pairs ⟶ Higher order Clusters ⟶ Precipitates.

Formation of close paired ions and vacancies occurs by direct aggregation, and by an oxidation reaction summarised by the equation

$$2\ Fe^{2+} + \tfrac{1}{2}\ O_2 \rightleftharpoons 2\ Fe^{3+} + [V_{Mg}] + O^{2-}$$

where $[V_{Mg}]$ presents a vacant cation site.

Under reducing treatments the reaction is reversed, giving rise to the observed concentration dependence.

The electron microscope observations, although unsuccessful in identifying the spinel precipitate, do show that the nucleation and growth of dislocation loops of vacancy type is associated with the formation of impurity-vacancy clusters. For short ageing times at 800°C, the flow stress is lowered as pairs of anion-cation vacancies pre-existing in the crystal combine to form larger vacancy clusters, which collapse as vacancy loops. Additional vacancies are also released from impurity-vacancy clusters during the formation of the spinel lattice.

In Fe : 2 the impurity supersaturation is such that vacancies are incorporated in impurity-vacancy clusters, and the free vacancy supersaturation is insufficient for loop nucleation.

Nucleation of the spinel precipitate in Fe : 2, as observed by the strong E.P.R. precipitate line, occurs during melt cooling. Nevertheless, a precipitate dispersion is unresolvable in the electron microscope in as-grown crystals. Anneals at 800°C in air, although enhancing the precipitate line, serve only to lower the flow stress by a coarsening of the dispersion until particles are resolved after 70 hours.

The conclusion that the low temperature peak in the case of both Fe : 1 and Fe : 2 is directly attributable to a precipitation hardening by submicroscopic particles is emphasised by the reharden-ing of Fe : 2 after reduction in a CO environment. The flow stress is found to recover to a maximum value after 100 hours and subsequently decays. During the period up to 200 hours no resolvable precipitates are detected, although only a small proportion of re-oxidised Fe^{3+} ions are present as isolated impurity and impurity-vacancy pairs.

At temperatures above 1,000°C in air, impurity clusters are dispersed, and a separate cluster forms, which is responsible for the marked flow stress peak of Fe : 2 at 1,200°C. This centre is attributed to interstitial oxygen in association with Fe^{3+} ions. The less significant peak at this temperature for Fe : 1 is believed to be the result of a supersaturation of anion vacancies which annihilate directly with the diffusing interstitial species.

5.2.j Conclusions

The defects responsible for the flow stress variations of iron doped crystals may be summarised as:-

1) Fe^{3+} - vacancy pairs and pre-precipitate clusters.

These are important obstacles in as-grown crystals of Fe : 1, but are not believed to be responsible for the ageing peaks in Fe : 1 or Fe : 2.

2) Spinel precipitates.

The flow stress of Fe : 2 is controlled by submicroscopic precipitates in the as-grown state, and precipitates of unresolvable

dimensions are responsible for the low temperature ageing peaks in Fe : 1.

3) Interstitial oxygen

A general behaviour is found for all the systems studied in which the diffusion of an interstitial species, proposed to be oxygen, is responsible for the high temperature ageing peaks in oxidising atmospheres.

4) Anion-cation vacancy pairs.

These defects act as obstacles to dislocation glide in as-grown crystals of Fe : 1, but are incorporated as higher order clusters and are therefore not effective in Fe : 2.

5.3 Titanium

Two different melts were utilised, Ti : 1, containing 1,000 p.p.m., and Ti : 2, containing 500 p.p.m. of the major impurity.

5.3.a. Variations of the Flow Stress with Heat Treatment.

The effect is isochronal and isothermal anneals on the flow stress of crystals Ti : 1 and Ti : 2 is shown in Fig. 5.9 and Fig. 5.10. The annealing sequence over the whole range shows a similar form for each case, the magnitude of the effects depending on the dopant level.

5.3.b. E.P.R. Spectra

The only reported spectrum for the titanium ion, observed at $77^{o}K$, has been attributed to a centre of the type $[Ti^{3+}V]$, in a $\langle 100 \rangle$ orientation[47]. It was maintained in this work that it

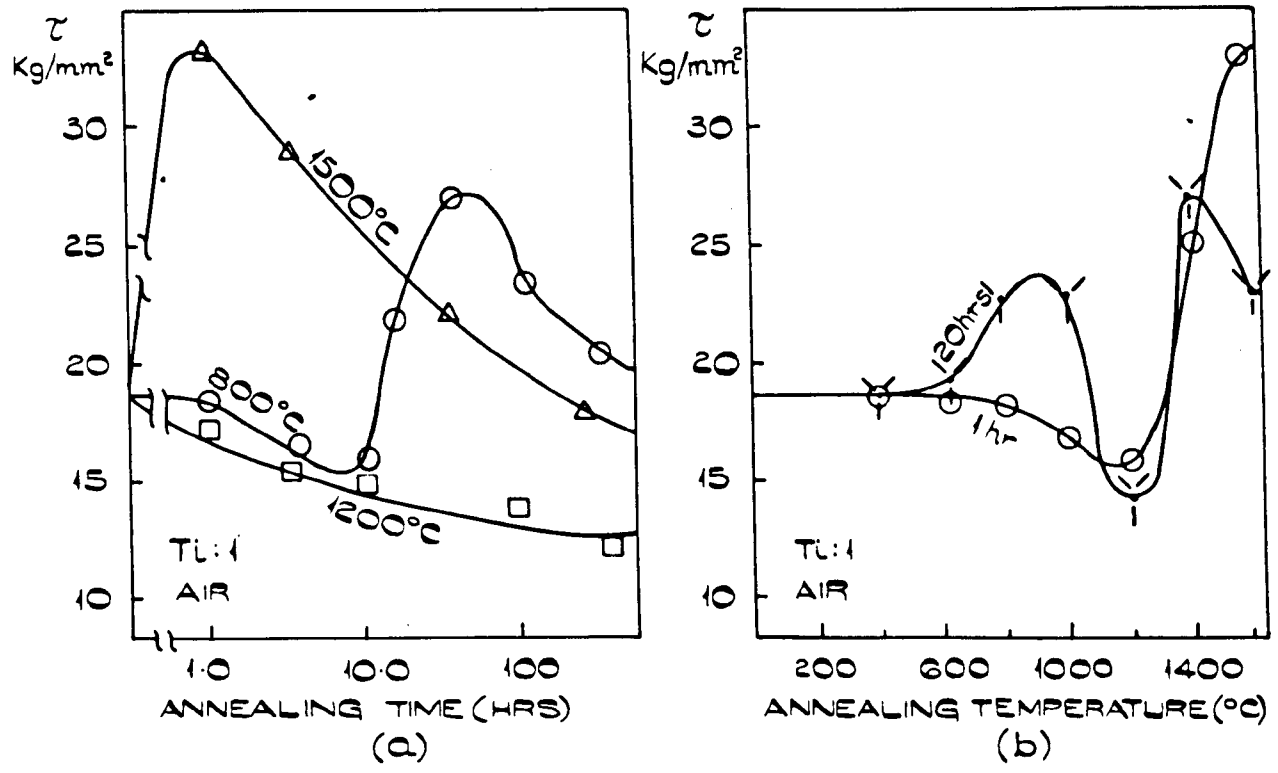

FIG. 5.9

EFFECT OF HEAT TREATMENT ON THE FLOW STRESS OF Ti:1.

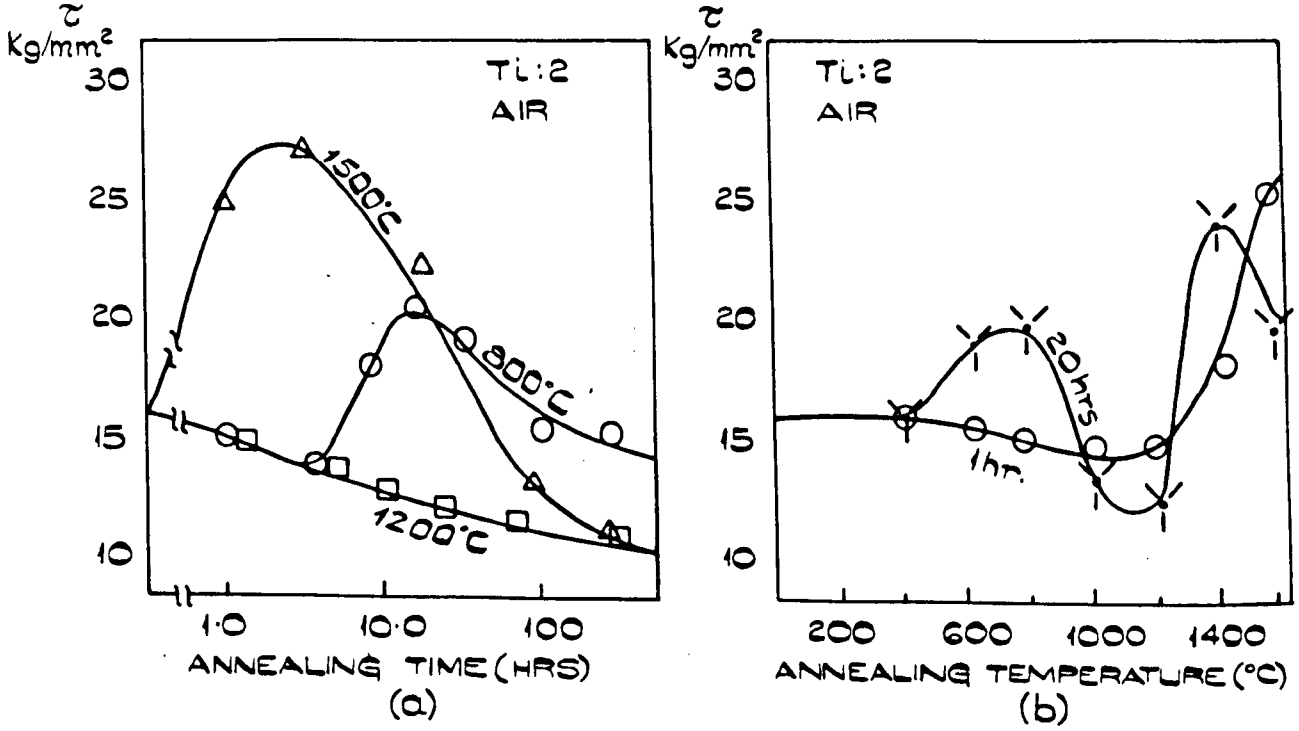

FIG. 5.10

EFFECT OF HEAT TREATMENT ON THE FLOW STRESS OF Ti:2

was possible to induce the spectrum for crystals containing low ionic concentrations by both x-irradiation and reducing anneals at 1,200^{o}C. A more complex background spectra was attributed to associated states of lower symmetry.

An examination of the E.P.R. spectrum of as-grown Ti : 1 at liquid nitrogen temperatures has established that centres of the type described are present in insufficient quantity to be detectable against a background of accidental impurities, and that even after prolonged anneals these centres are not formed in any significant concentration.

In octohedral crystal fields no E.P.R. spectrum is possible, since no first order Zeeman splitting of the ground state orbital triplet of Ti^{3+} occurs in this type of symmetry. Ti^{4+} ions contain an empty 3d shell, and hence cannot be monitored by paramagnetic resonance.

It is concluded from this E.P.R. investigation that the majority of solid solution ions in titanium doped crystals are present as Ti^{3+} ions in isolated or possibly high order complex cluster forms, and as tetravalent ions in both isolated and associated states.

5.3.c. Optical Absorption Spectra.

Additional information on the valence state of titanium ions is possible from a study of the optical absorption spectra of Ti : 1 shown in Fig. 5.11 for three different heat treatments. No previous study of the optical spectra of titanium ions in MgO has been reported, and an identification of optical absorption bands with

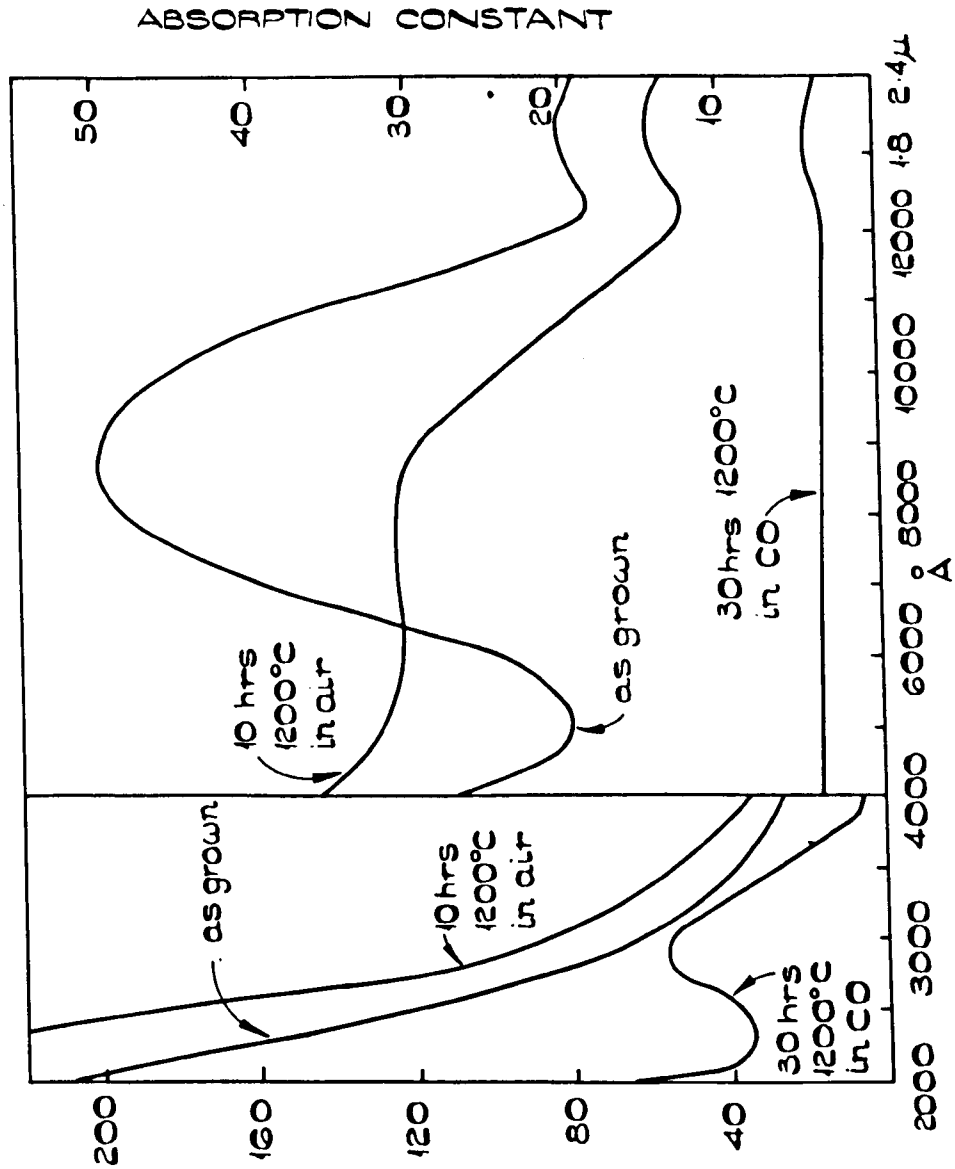

FIG. 5.11
OPTICAL SPECTRA OF CRYSTAL Ti:I FOR THREE HEAT TREATMENTS.

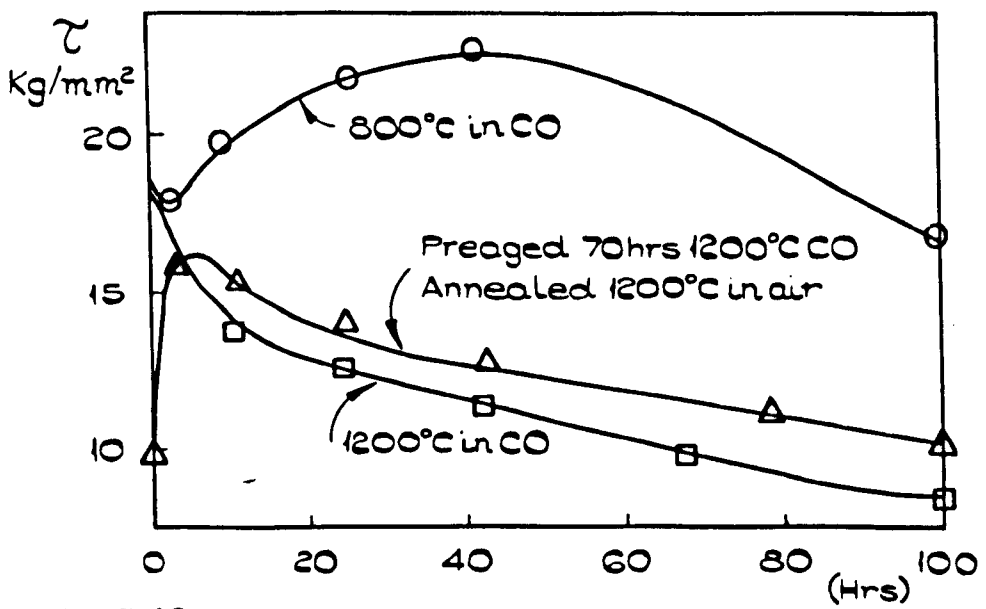

FIG. 5.12
EFFECT OF ATMOSPHERE ON THE AGEING BEHAVIOUR OF Ti:I.

the form of impurity ions is therefore empirical.

The very broad band appearing at 8,500 Å is associated with the deep blue colouration of as-grown crystals, and from its behaviour in reducing atmospheres, is believed to be due to isolated Ti^{4+} ions. Strong reduction e.g. 30 hours at 1,200°C in CO, completely destroys this absorption band, but enhances a band at 2,900 Å, which, from a comparison with the reported E.P.R. behaviour, is the result of reduction of Ti^{4+} ions to the isolated trivalent state. It is concluded therefore that in the as-grown state oxidation of the titanium impurity is virtually complete. Another prominent feature of the optical spectra of as-grown crystals is a broad band in the infra-red, enhanced by oxidising treatments, and decreased by reducing anneals. This band is tentatively assigned to a more complex cluster, possibly arising from Tyndall scattering from precipitate particles.

No other impurity bands due to simple aggregates are resolvable in the spectra, but it seems probable that the form of impurity in as-grown crystals is predominantly that of unassociated Ti^{4+} ions and large complex clusters up to precipitate size.

5.3.d. Microstructural Observations.

In melt Ti #1, precipitates of a size visible in the electron microscope were observed in parts of the melts in as-grown crystals, the result of impurity segregation during growth. Specimens used for ageing treatments were selected from crystals where, as far as possible, visible precipitates did not occur. No precipitates were

visible in the as-received Ti : 2 melt.

The microstructural changes in the titanium-doped Ti : 1 crystals caused by successive anneals at a low temperature (800°C) are shown in Fig. 5.13. The initial development typically observable after 20 hours is of a dispersion of particles 100 - 150 Å in diameter showing coherency strain contrast and associated with a low density of dislocation loops. For longer ageing times the strain contrast lobes disappear and the particles are assumed to have lost coherency. In general particles larger than 400 Å diameter are not resolved by coherency strain contrast. The precipitate density increases with ageing time up to an optimum value after 50 - 70 hours and subsequently coarsens. Electron diffraction spots due to the precipitate may be readily observed after 30 hours, the diffraction pattern corresponding to a spinel lattice with principal axis parallel to that of the matrix. On the basis of the lattice parameter determined later from the particle image width, the precipitate is identified with the inverse titanium spinel Mg_2TiO_4.

The vacancy character of dislocation loops formed during heat treatments at 800°C is evidence for the clustering of a supersaturation of vacancies at low temperatures and the subsequent coalescence of loops after short ageing times. Initially these are mainly of circular prismatic type, lying on {110} planes. Further ageing is found to increase the density of loops, the reduced vacancy supersaturation giving rise to dislocation climb into

Fig 5.13(b) is an electron micrograph taken by Dr. M.H. Lewis from a specimen prepared by B.F. Wicks

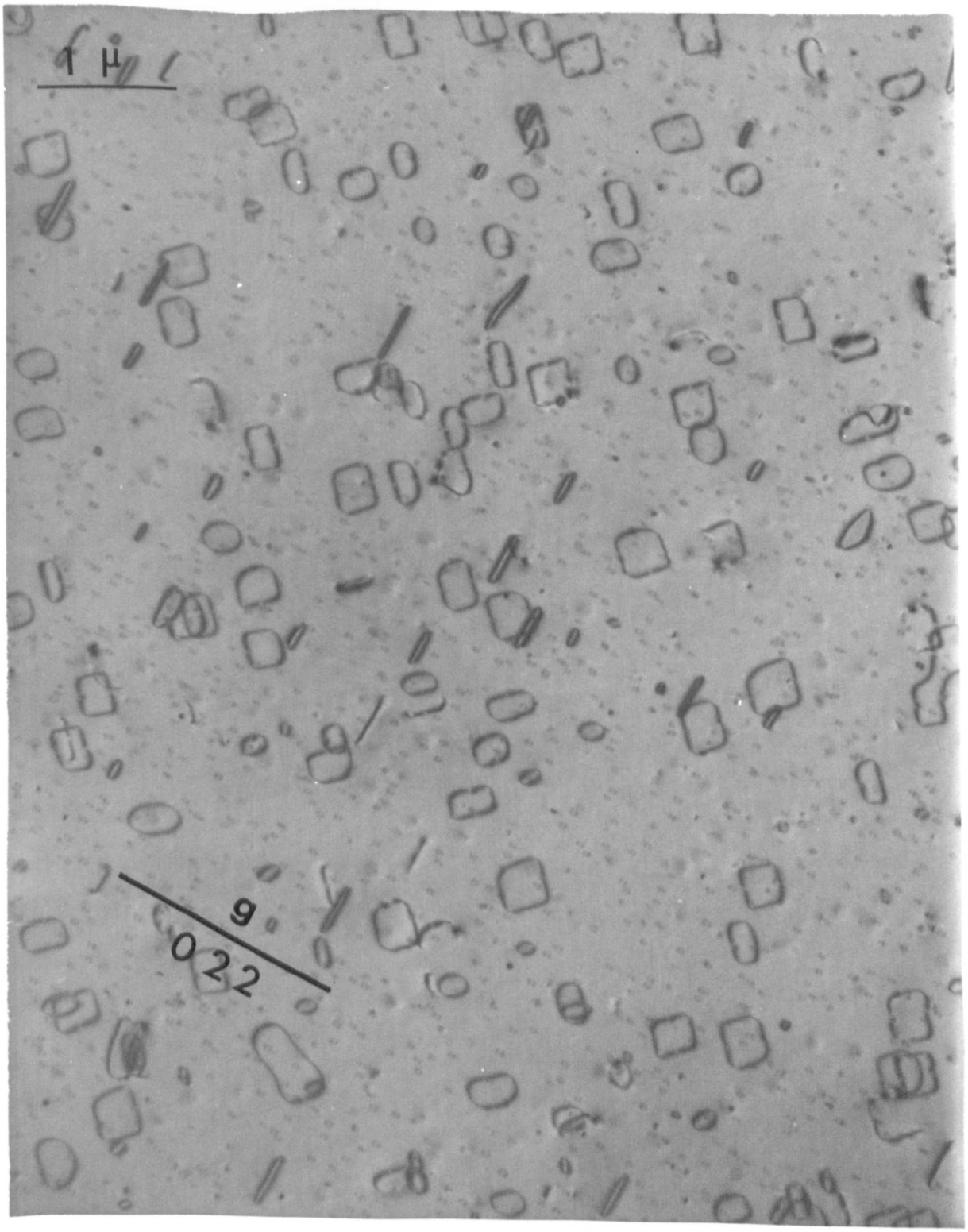

FIG. 5.13 (a)

Ti:I AGED FOR 20 HOURS AT 800°C IN AIR.

(1000 k.v.)

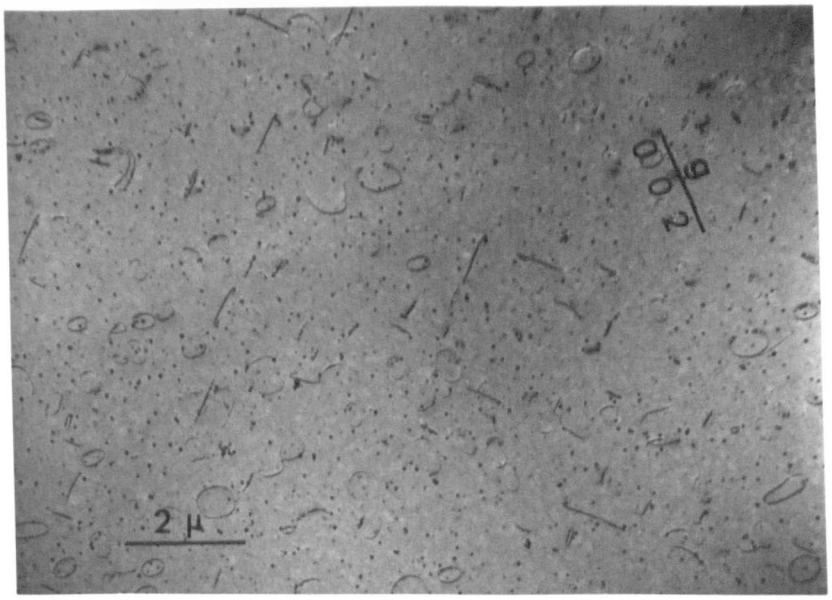

Fig. 13.(b)

Ti : 1 aged for 30 hours at 800°C in air.

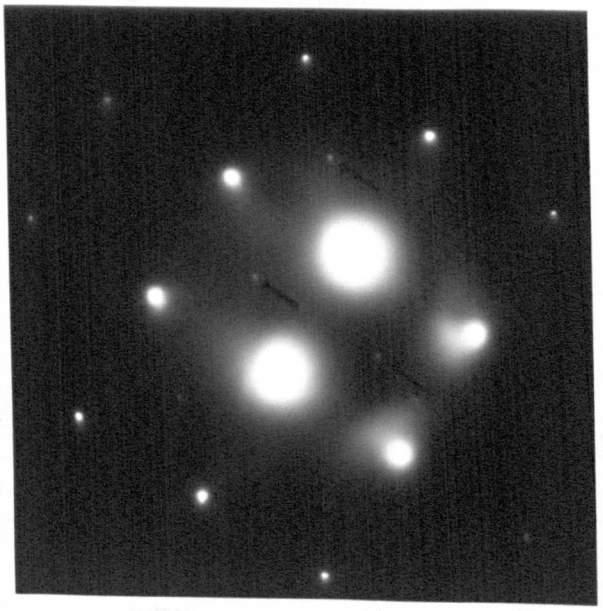

Fig. 5.13 (c)

Electron diffraction pattern showing spots due to spinel precipitates Mg_2TiO_4 (arrowed) and MgO matrix spots.

crystallographic forms with edges parallel to ⟨110⟩ and ⟨100⟩ directions, and a tendency for loops to adopt a preferential {100} planar configuration. After 200 hours the microstructure observed consists typically of a low density of irregularly shaped loops and loop segments pinned by a coarse dispersion of precipitate particles (Fig. 5.13.e).

Loop nucleation and growth is undetected in the aged microstructure of Ti : 2, consistent with a lower titanium concentration and thus, indirectly, a lower concentration of vacancies of both signs. No precipitation is resolvable at the ageing peak for this system, but a low density dispersion is observed at longer ageing times, as shown in Fig. 5. 13 (f).

The microstructure of Ti : 1 at higher temperatures is similar to that formed by extended anneals at 800°C. Fig. 5.13.(g) shows the microstructure after 2 hours at 1,200°C in air. A low density of loop segments is apparent against a coarse background of titanium spinel precipitate.

5.3.e. Effect of Atmosphere on the Annealing Behaviour

The effect of successive anneals in carbon monoxide atmospheres on the flow stress is shown in Fig. 5.12. At 800°C no marked change is apparent, except for a less prominent hardness peak. It is after prolonged anneals, or at higher temperatures that the environmental oxygen partial pressure markedly influences the ageing behaviour. The curve at 1,200°C falls more rapidly than in the corresponding curve of Fig. 5.9 (a) in air, as clusters of Ti^{4+} ions are reduced to Ti^{3+}, and dispersed by this treatment. The lack of an E.P.R. spectrum from Ti^{3+} - vacancy clusters in crystals aged in a

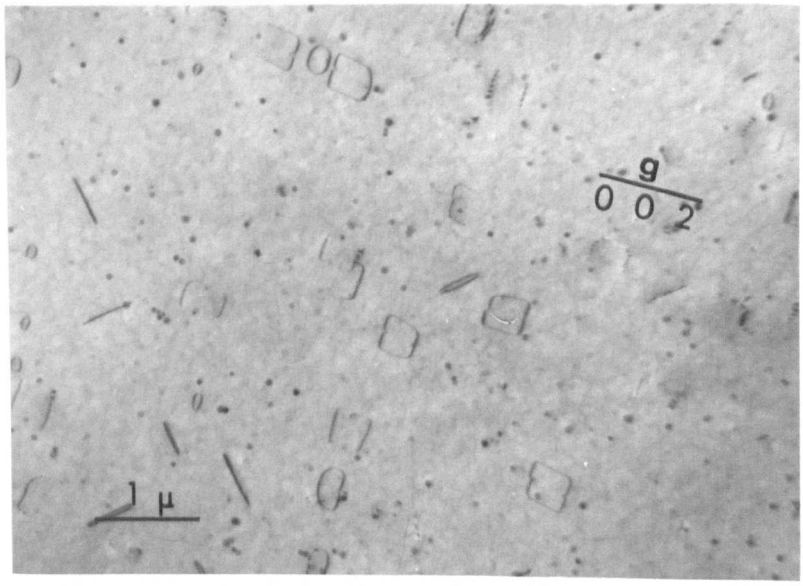

Fig.5.13.(d)

Ti : 1 aged for 70 hours at 800°C in air.

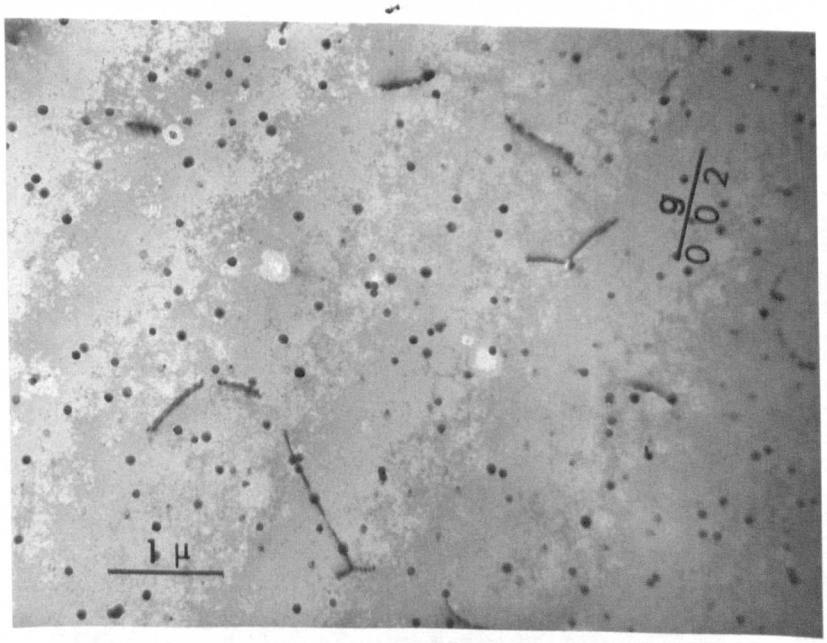

Fig.5.13 (e)

Ti : 1 aged for 200 hours at 800°C in air.

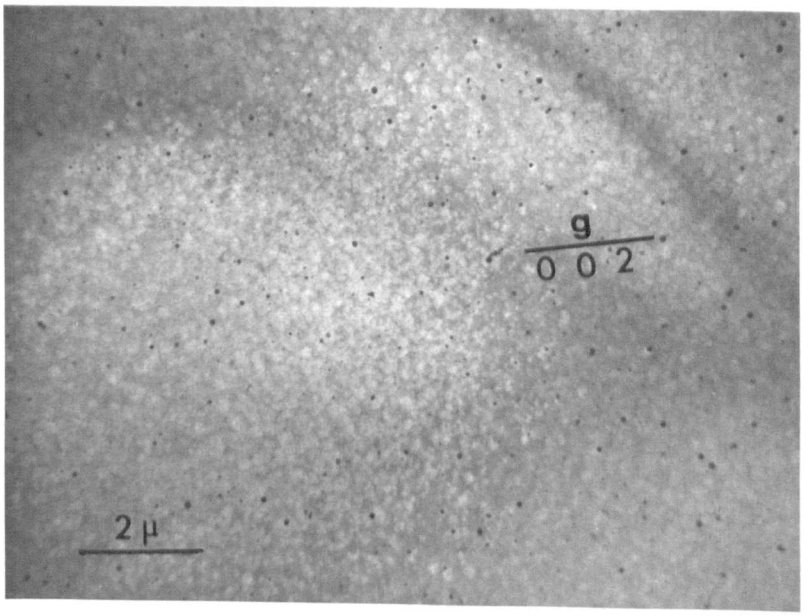

Fig. 5.13. (f)

Ti : 2 aged for 90 hours at 800°C in air.

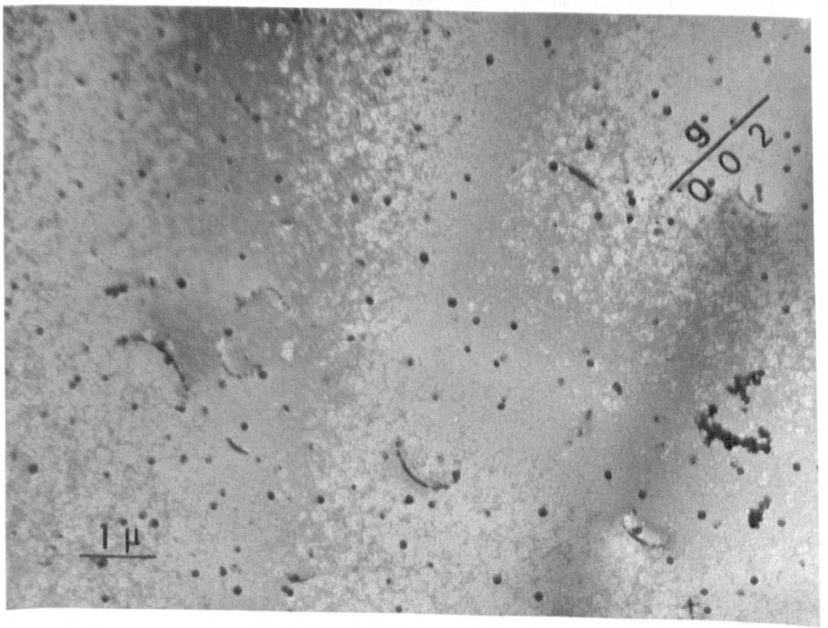

Fig. 5.13. (g)

Ti : 1 aged for 2 hours at 1,200°C in air.

reducing environment, and the growth of an optical absorption band attributed to isolated Ti^{3+} ions leads to the logical conclusion that vacancies are dispersed by this heat treatment, and do not form close associations with trivalent ions in any detectable concentration.

The suppressive effect of reducing atmospheres on precipitation is further emphasised by an examination of the microstructure of reduced crystals by electron microscopy. Fig. 5.14 illustrates a typical micrograph of a specimen aged for 50 hours at 1,200°C in CO_2 showing a low density of titanium spinel precipitate, some in the form of octahedra with {111} facets, and a low density of dislocation segments - the remnants of vacancy loops formed by condensation of vacancies released from impurity - vacancy complexes. The initial precipitate is probably formed either during growth or in the early stages of ageing at this temperature. After prolonged (200 hours) treatment in reducing conditions, impurity ions revert completely to solid sclution.

The result of re-ageing a crystal containing impurity in Ti^{3+} form in air is also indicated in Fig. 5.12. The yield stress recovers very rapidly to a value below its original as-grown value, and subsequently follows the overaged behaviour found for as-grown crystals. No significant increase in the optical absorption band attributed to Ti^{4+} is observed over the whole ageing range, and the formation of precipitate particles during the re-ageing treatment is associated with a corresponding reduction in the Ti^{3+} optical absorption band. The flow stress recovery is evidently attributable to a precipitation phenomenon.

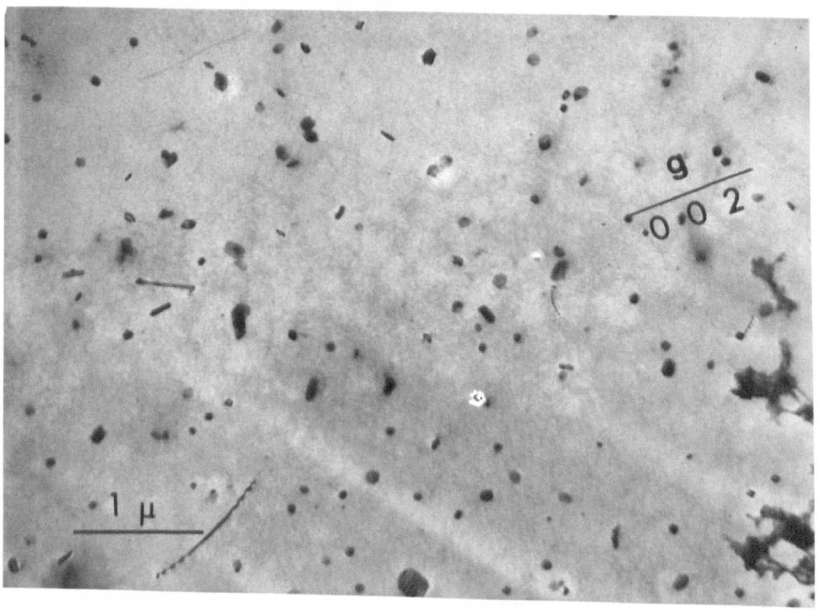

Fig. 5. 14.

Ti : 1 aged for 50 hours at 1,200°C in a reducing (CO) atmosphere.

5.3.f. Correlation of E.P.R., Optical Absorption and Microstructure.

The flow stress curves for temperatures less than 1,200°C show features which are consistent with a precipitation hardening and overageing mechanism.

For short ageing times at 800°C the flow stress is initially lowered as cation - anion vacancy pairs coalesce to form larger vacancy clusters which collapse as vacancy loops. Precipitation occurs more slowly on a sufficient density of nucleation sites to reharden the crystal up to 50 - 70 hours, after which a distinct coarsening of precipitates is discernable.

The marked hardening effect of anneals at 1,500°C in air is believed to be the result of interstitial oxygen diffusion. Electron microscope observations of specimens subjected to this treatment show a coarse precipitate structure, corresponding to an over-aged state. The enhanced high temperature hardness can hence be attributed to the strong interaction between glide dislocations and the large anisotropic strain field around the interstitial oxygen species. The fall in flow stress after longer ageing times is the result of a dynamic equilibrium between interstitial oxygen and free vacancies (and vacancies incorporated in complex clusters) by a direct annihilation process.

The evidence that the flow stress of as-grown crystals is mainly determined by the presence of clusters of tetravalent titanium ions and vacancies of both signs, while precipitate particles are responsible for the ageing behaviour, is reinforced by the results of anneals in a CO atmosphere. At 800°C the

reducing treatment is not sufficient to inhibit impurity-vacancy clustering, and the formation of a spinel lattice. This is illustrated by the flow stress variation over this time. A strongly reducing atmosphere (1,200°C) leads to the destruction of clusters, with the formation of isolated Ti^{3+} ions, and the nucleation of dislocation loops which grow rapidly in the supersaturated vacancy environment. The effect of heating in oxygen, vacuum or a reducing environment may be summarised by the equation:-

$$2Ti^{4+} + O^{2-} + [V_{Mg}] \rightleftharpoons 2\ Ti^{3+} + \tfrac{1}{2}\ O_2$$

The similarity of the behaviour of Ti : 2 suggests that these remarks apply to crystals containing a lower impurity concentration. The low temperature precipitation peak in this case corresponds to a submicroscopic dispersion of precipitates. On ageing further the particles grow to a resolvable size at the expense of precipitate density, corresponding to the overaged portion of the flow stress curve.

5.3.g. Conclusions

The defects responsible for the flow stress of titanium doped crystals after various heat treatments are listed as follows:-

1) Close paired impurities and vacancies, and pre-precipitate clusters.

A high proportion of Ti^{4+} - vacancy pairs and higher order clusters are implied to be present in unaged crystals and these are the most important obstacles to dislocation movement in the

as-grown condition.

2) Cation - anion vacancy pairs.

The existence of a vacancy supersaturation in the as-grown state is responsible for the initial plastic softening during anneals below 1,200°C during which larger clusters are formed.

3) Spinel precipitates.

The difficulty of dislocation movement through the spinel precipitate dispersion formed during low temperature anneals results in the observed hardness peak. For Ti : 1 these precipitates at peak hardness can be observed directly, but for Ti : 2 the obstacles are submicroscopic.

4) Interstitial oxygen.

The diffusion of interstitial oxygen is responsible for the enhanced flow stress observed in oxidising conditions above 1,200°C.

5.4. Vanadium

Only one dopant level of 1,500 p.p.m. vanadium is considered in this section. A uniform green colouration was present throughout this melt, labelled V : 1, indicative of a homogeneous distribution of impurity.

5.4.a Variations of the Flow Stress with Heat Treatment

Typical flow stress curves for air anneals are shown in Fig. 5.15. A behaviour characteristic of a precipitation hardening and overageing phenomenon is observable only for anneals at less than 1,000°C. All other heat treatments cause a lower flow stress than the as-grown value.

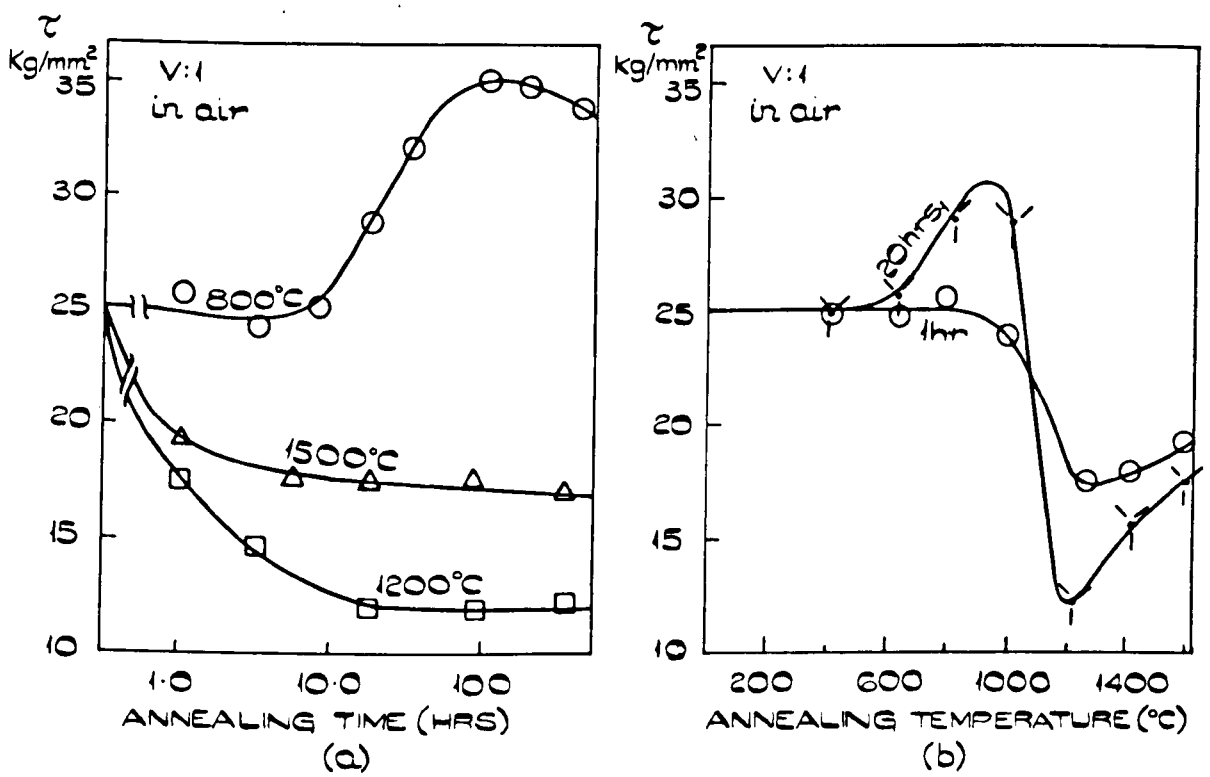

FIG. 5.15

EFFECT OF HEAT TREATMENT ON THE FLOW STRESS OF V:1.

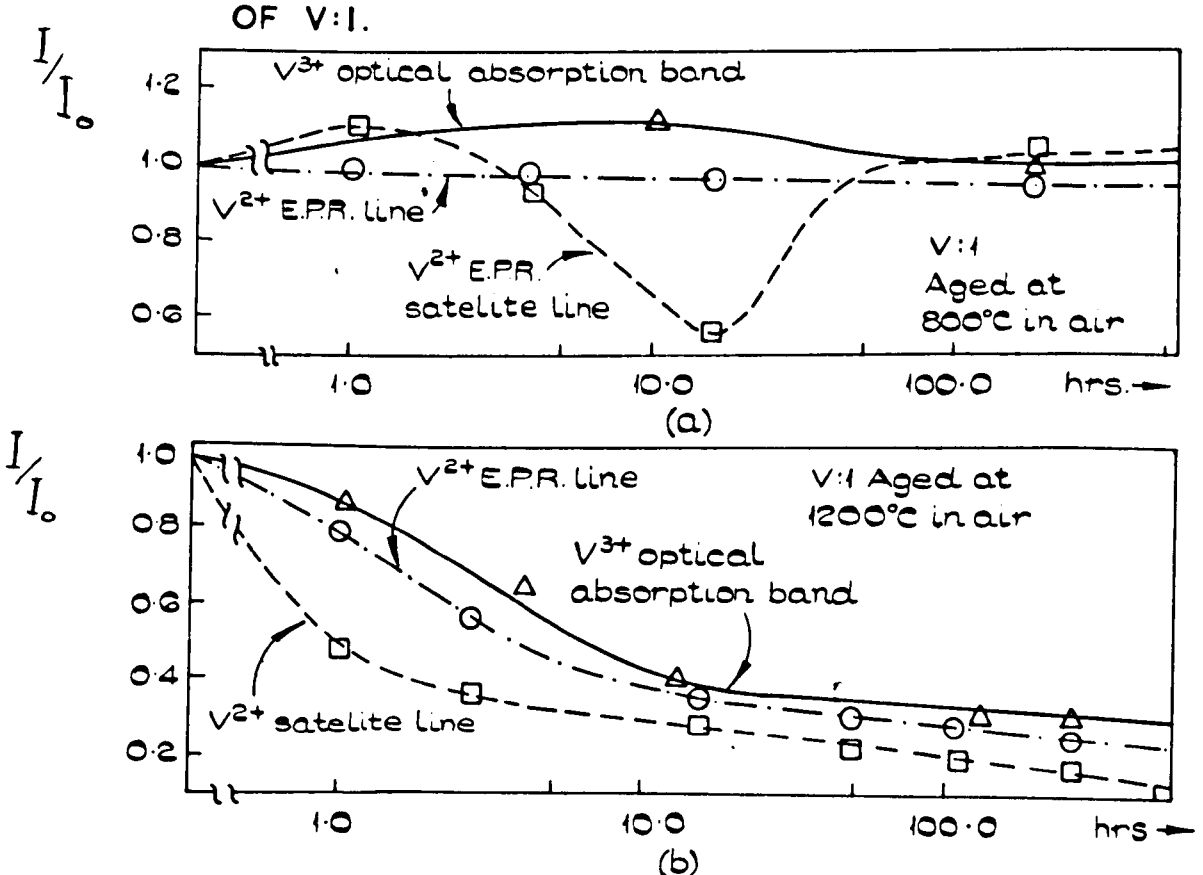

FIG. 5.16

EFFECT OF HEAT TREATMENT ON E.P.R. AND OPTICAL SPECTRA OF V:1 (a) 800°C IN AIR (b) 1200°C IN AIR.

5.4.b E.P.R. and Optical Absorption Spectra.

A selected region of a typical E.P.R. spectrum of vanadium doped crystals is shown in Fig. 5.17 (a), containing the line spectrum of V^{2+} ions. This spectrum consists of eight hyperfine groups due to a nuclear spin of $I = {}^{7}/_{2}$ with $g = 1.975$, each group made up of three fine structure lines. The degenerate levels of the V^{3+} ion are not separated by an octohedrally co-ordinated cubic environment into levels observable at microwave frequencies. Calculations of the energy level splitting in axial fields[73] suggests that the microwave transitions will be relatively weak, and observable only at low temperatures. An E.P.R. spectrum due to V^{3+} ions has never been observed in MgO, and in this study of doped crystals could not be detected at $77^{o}K$. It is concluded, therefore that although a proportion of V^{3+} ions may be in simple dimer configurations, the majority are in isolated octohedral sites and contained in more complex impurity - vacancy configurations which obscure the spectra of a particular ion.

The origin of the two satellite lines at each V^{2+} hyperfine transition is not well established. The strong angular dependence of the line width of the pair has been attributed to small distortions along $\langle 111 \rangle$ directions at the V^{2+} site. Dickey and Drumheller[74] ascribe this distortion to tetravalent vanadium states charge compensated by interstitial oxygen. The relative intensity of these lines with respect to the hyperfine line suggests that the

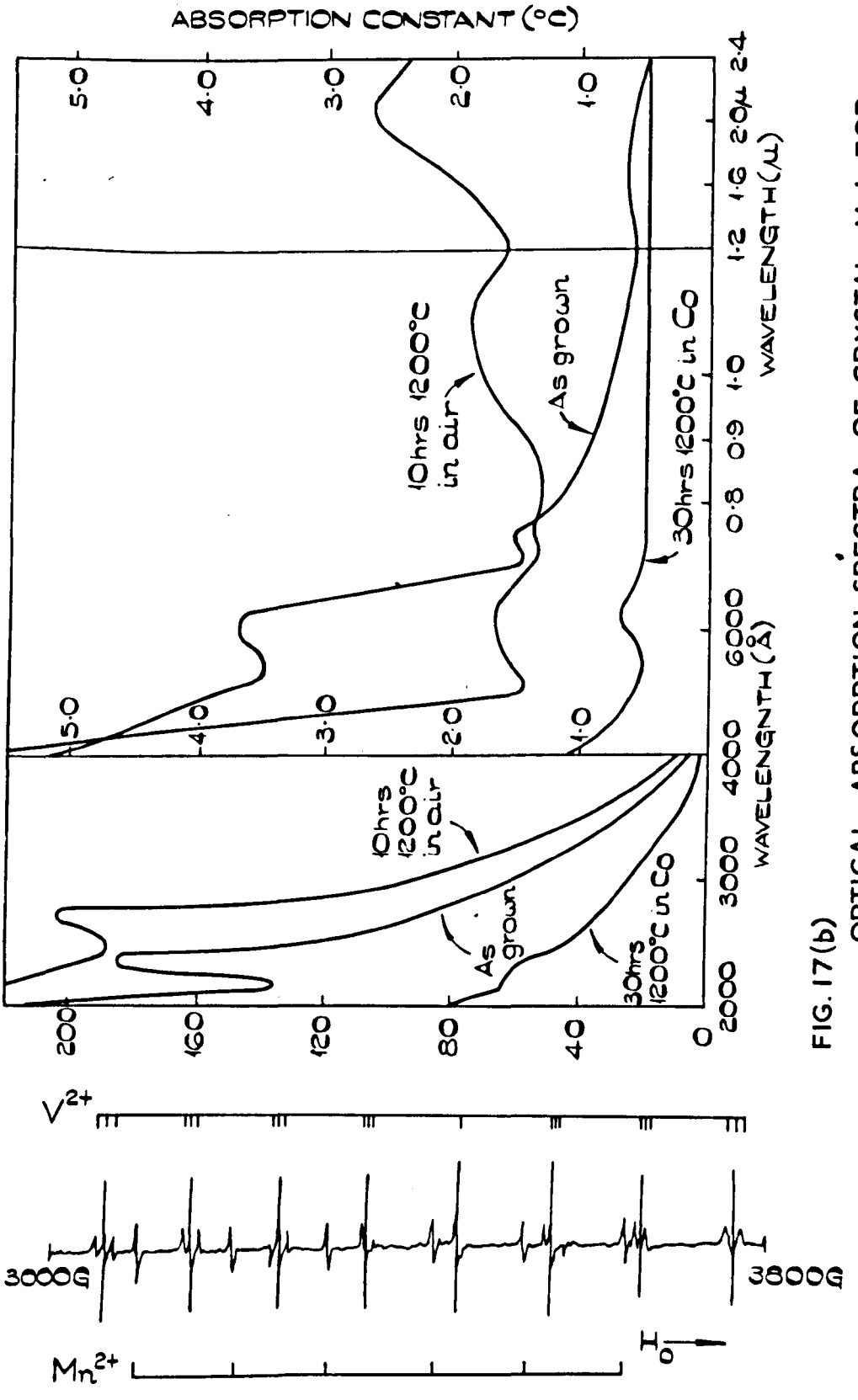

FIG. 17(b)
OPTICAL ABSORPTION SPECTRA OF CRYSTAL V:I FOR THREE HEAT TREATMENTS.

FIG. 17(a)
TYPICAL PARAMAGNETIC RESONANCE SPECTRUM OF V:I CRYSTAL SHOWING ADDITIONAL SATELLITE V^{2+} LINES. H_0 IS PARALLEL TO A CUBE AXIS.

concentration of these centres is less than 100 p.p.m.

The near infra-red, visible and u.v. absorption spectra of selected crystals of V : 1 is shown in Fig. 5.17 (b) after three heat treatments. The prominent absorption bands in the spectrum at 2,700 Å and 6,200 Å are believed to be due to single V^{3+} ions [75]. Absorption by V^{2+} ions is extremely weak, but is linked to the peak at 7,550 Å, which in fact consists of three unresolvable lines. A broad band occuring at 9,500 Å has been attributed previously to Fe^{2+} ions, [75] although this seems unlikely from the behaviour of the band in the annealing conditions illustrated. It is therefore tentatively attributed to a trivalent ion cluster. Another broad band in the near infra-red spectrum shows a behaviour which is consistent with absorption and Tyndall scattering by precipitate particles.

The concentration of V^{2+} ions, evaluated using a standard E.P.R. sample is calculated as 900 p.p.m. The remaining 600 p.p.m. of the total vanadium concentration, determined spectrographically, consists mainly of isolated V^{3+} ions, V^{4+} ions, and ions associated with vacancies.

The E.P.R. and optical spectral changes for crystals aged at 800°C are shown in Fig. 5.16(a), illustrating the variation in intensity of the V^{3+} band and both the hyperfine and forbidden satellite lines. The V^{2+} concentration is seen to show little variation over the annealing range, while the V^{3+} concentration monitored by optical spectroscopy increases up to 10 hours

and subsequently decreases to a value close to the as-grown concentration. The intensity of the lines attributed to interstitial oxygen, however, shows a complicated behaviour. The most logical explanation for the variation in the spectra of the V^{4+} - interstitial centre is that of direct interstitial - vacancy annihilation followed by the rediffusion of atmospheric oxygen at longer ageing times.

The same quantities are plotted in Fig. 5.16 (b) for anneals at 1,200°C in air. The decrease in flow stress in this temperature range can be seen to be associated with the rapid depletion of vanadium V^{2+} and V^{3+} ions in solid solution.

5.4.c. Microstructural Observations.

Spinel precipitates are never observed in any as-grown crystals doped with vanadium Fig. 5.18 shows the microstructural changes in specimens annealed at 800°C in air. In the early annealing stages (20 hours) a low density of features develop which grow in size and density as a resolvable dispersion of prismatic dislocation loops associated with a low density of spiked precipitates lying along ⟨110⟩ and ⟨100⟩ matrix directions. The loop density increases up to a maximum after 70 hours and subsequently decreases with a corresponding increase in loop size, giving rise to a microstructure after long ageing times consisting of a low density of loop segments pinned by spiked precipitates. No precipitate dispersion corresponding to the vanadium spinel was identifiable for ageing treatments up to 500 hours.

Attempts to identify the precipitate structure by electron diffraction were unsuccessful. However, precipitates of a similar

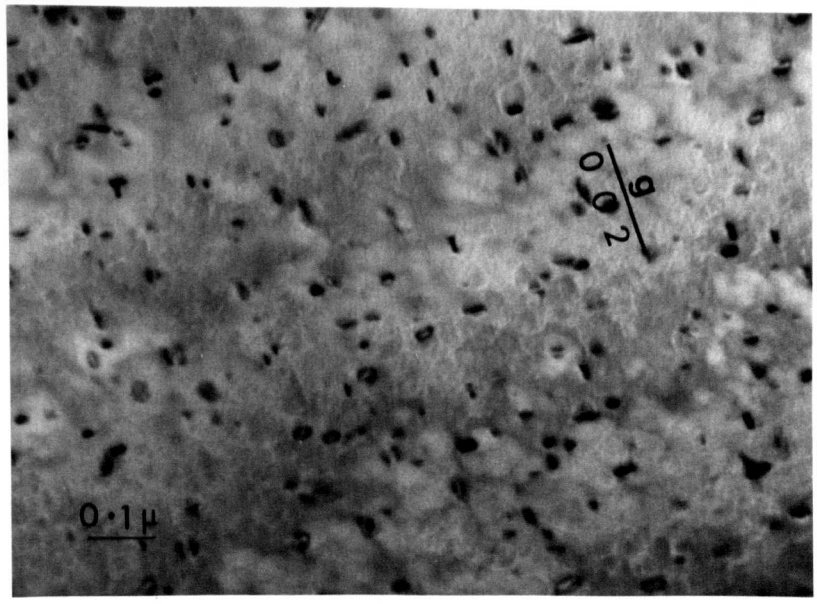

Fig. 5.18 (a)

V : 1 aged for 70 hours at 800°C in air.

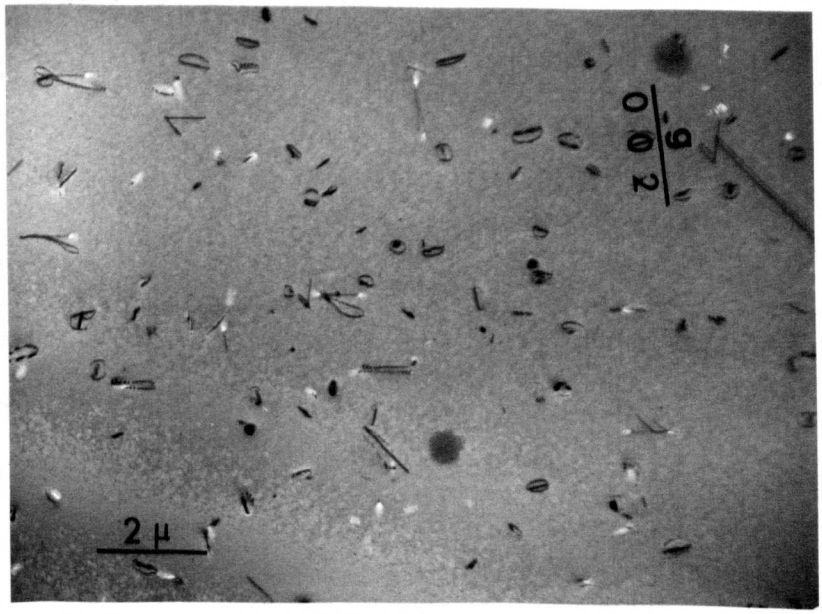

Fig. 5.18 (b)

V : 1 aged for 180 hours at 800° in air.

shape have been extracted from MgO crystals previously, and identified with the perovskite phases calcium zirconate $CaZrO_3$ and calcium titanate $CaTiO_3$. It is therefore proposed that the precipitate observed in V : 1 is the corresponding perovskite, $CaVO_3$. The known concentration of accidental calcium impurity is more than sufficient to account for the observed volume fraction of this phase. The density of the pervoskite precipitate is expected to give rise to a negligibly small contribution to the flow stress.

The microstructural development of vanadium-doped MgO after 1,200°C heat treatments in air is quite different, as shown in Fig.5.19. In the initial stages (1 - 3 hours) a low dislocation loop density is observed which is believed to arise, as for loop formation at lower temperatures, by the condensation of a high supersaturation of vacancies present as clusters in as-grown crystals. An enhanced vacancy mobility at this temperature leads to the development of loops as elongated edge dislocation dipoles, in $\langle 100 \rangle$ crystallographic orientations. The "dendritic" nature of this climb process is emphasised by Fig. 5.19 (c), showing the formation of $\langle 100 \rangle$ dendrite arms on a growing loop segment. This orientation corresponds to the directions of minimum dislocation line energy.

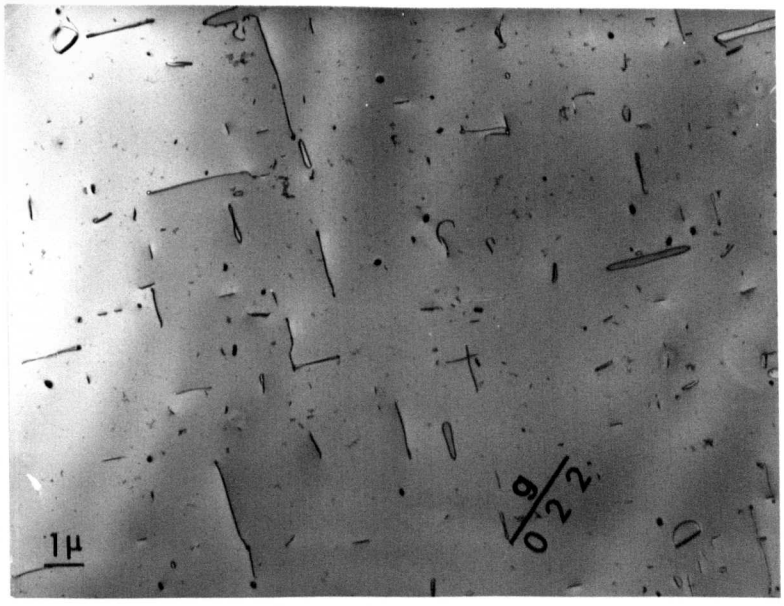

Fig. 5.19 (a)

V : 1 aged for 2 hours at 1,200°C in air.

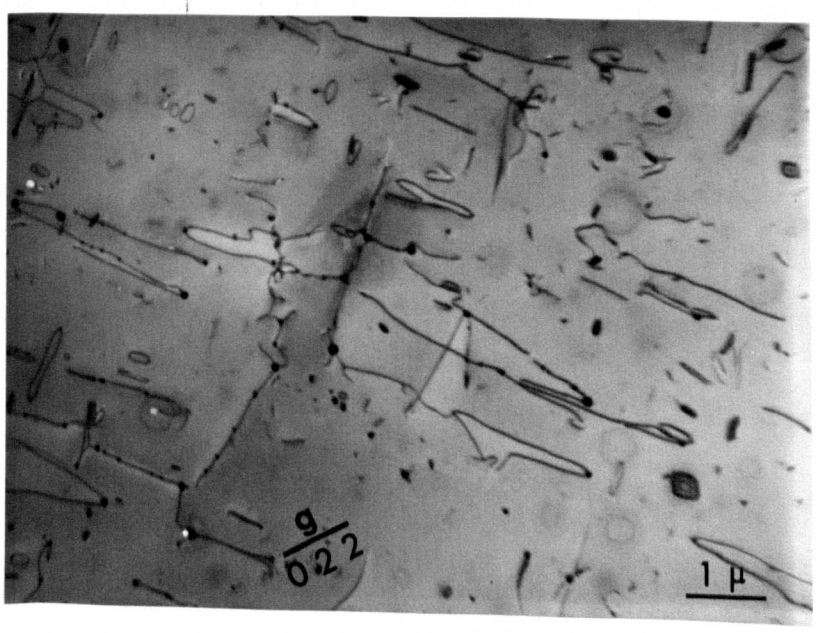

Fig. 5.19 (b)

V : 1 aged for 7 hours at 1,200°C in air.

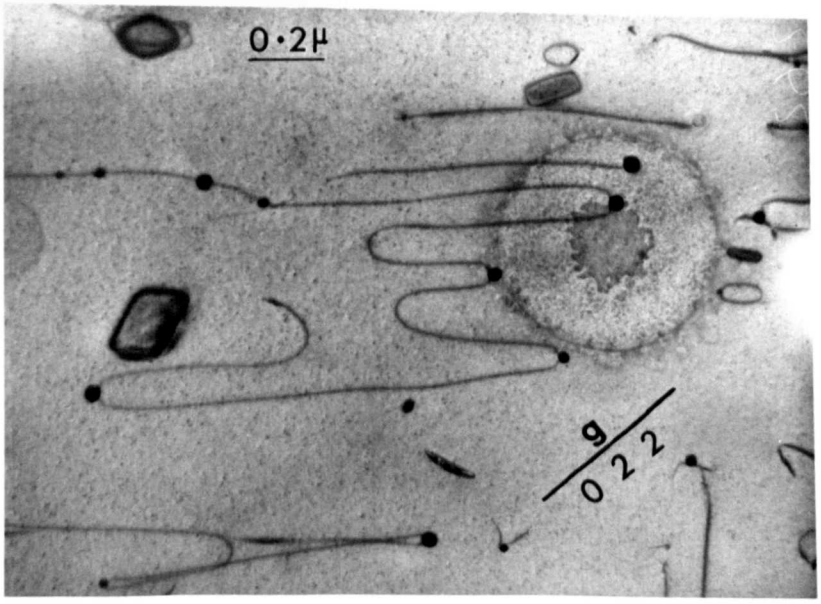

Fig. 5.19 (c)

V : 1 aged 12 hours at 1,200°C in air.

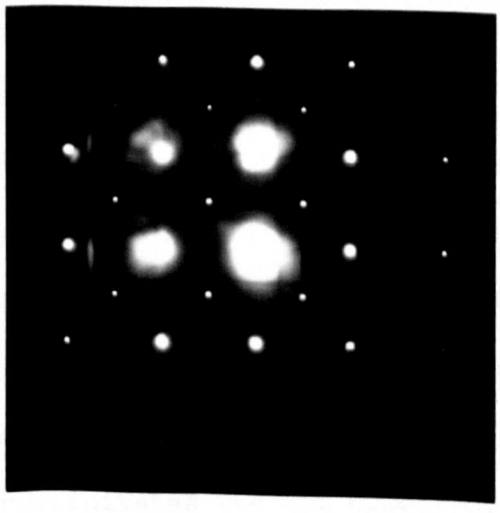

Fig. 5.19 (d)

Electron diffraction pattern showing spots due to spinel precipitates (arrowed) and MgO matrix spots.

The nucleation and growth of the dislocation dipoles at 1,200°C is closely associated with the formation of a precipitate, which is observed initially to decorate the ends, and later the arms of dislocation loops. Continued ageing leads to the appearance of an irregular dislocation network formed by loop interactions and stabilised by spinel particles (Fig.5.19 (b). Diffraction spots from the larger precipitates may be readily observed, as shown in Fig. 5.19 (d). The extra spots in this pattern are consistent with the cubic spinel precipitates Mg_2VO_4 or MgV_2O_4. At higher temperatures (1,500°C) a similar microstructure develops more rapidly.

5.4.d. Effect of Atmosphere on the Annealing Behaviour.

The development of microstructure in vanadium doped crystals is observed to be very dependent on the distance of the final electron microscope specimen section from the original cleaved surface. Sections prepared from near the crystal surface after ageing in air show a much higher growth rate of precipitates and dislocation loops, and the observed microstructure is sensitive to the oxygen partial pressure at the free surface. Fig. 5.20 shows a micrograph of a vanadium doped specimen after 50 hours at 1,200°C in CO, showing a low density of dislocations arranged in edge dipole forms. A low density of a second phase is also visible, presumed to be perovskite. Spinel precipitates are not observed.

Flow stress variations under reducing conditions are shown in Fig.5.21 (a). The initial stages of the annealing process are

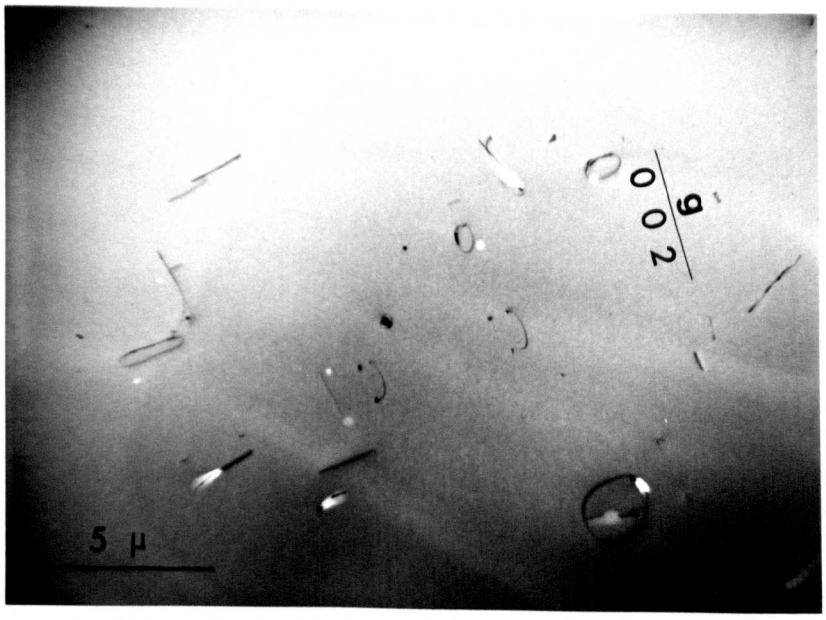

Fig. 5.20.

V : 1 aged for 50 hours at 1,200°C in a reducing (CO) atmosphere.

typified by a rapid drop in hardness, followed by a region in which the flow stress falls off less sharply.

Optical and E.P.R. line intensities after reduction are plotted in Fig. 5.21 (b). Reduction of vanadium ions proceeds rapidly and within 20 hours. at 1,200°C, the majority of the ions are in a divalent state. The V^{2+} satellite line attributed to interstitial oxygen decays very quickly, presumably by direct vacancy annihilation following reduction of the associated V^{4+} ion. The reaction between vanadium ions and oxygen at the free surface may be summarised as:-

$$2V^{2+} + \tfrac{1}{2}O_2 \rightleftharpoons 2V^{3+} + O^{2-} + [V_{Mg}]$$

In the high vacancy supersaturated environment produced by reducing conditions, prismatic loops are nucleated which climb rapidly into edge dipole configurations to give the microstructure observed in reduced crystals.

Under a renewed oxygen environment at 1,200°C, clusters of vacancies and impurities reform, giving rise to the rapid increase in flow stress (Fig. 5.21. (a)) prior to precipitate formation on dislocation segments retained in the reduced crystal. No marked optical absorption from V^{3+} ions is detectable throughout this initial period up to peak hardness, and it can therefore be concluded that impurity vacancy clusters are formed directly at the free surface.

5.4.e. Correlation of E.P.R., Optical Absorption and Microstructure.

The observations presented in this section support the conclusion that the as-grown flow stress is determined by close paired clusters of V^{3+} or V^{4+} with cation vacancies and cation-anion vacancy pairs.

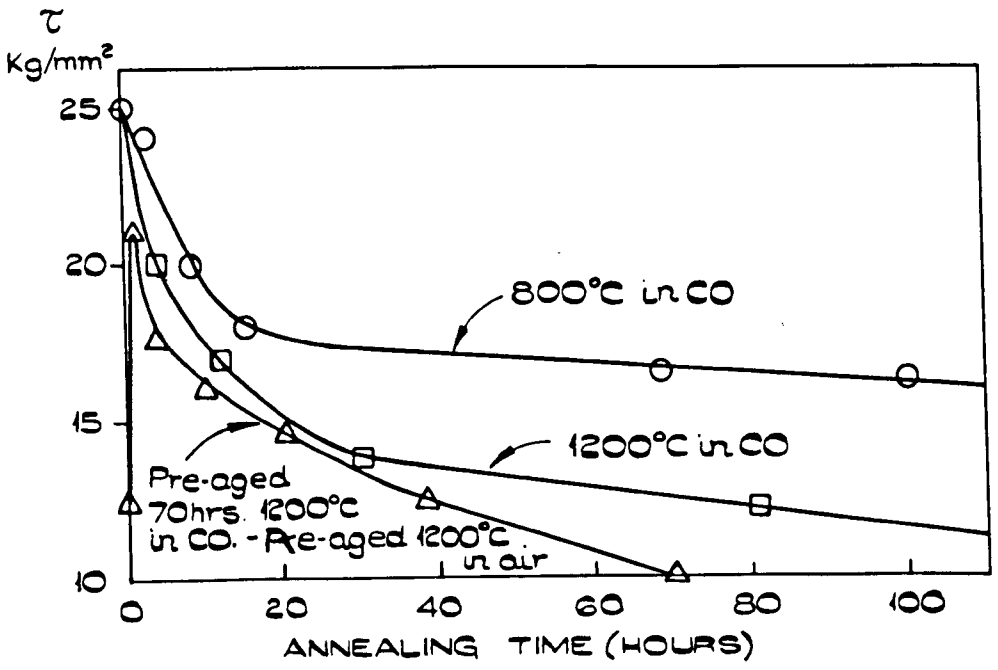

(a)

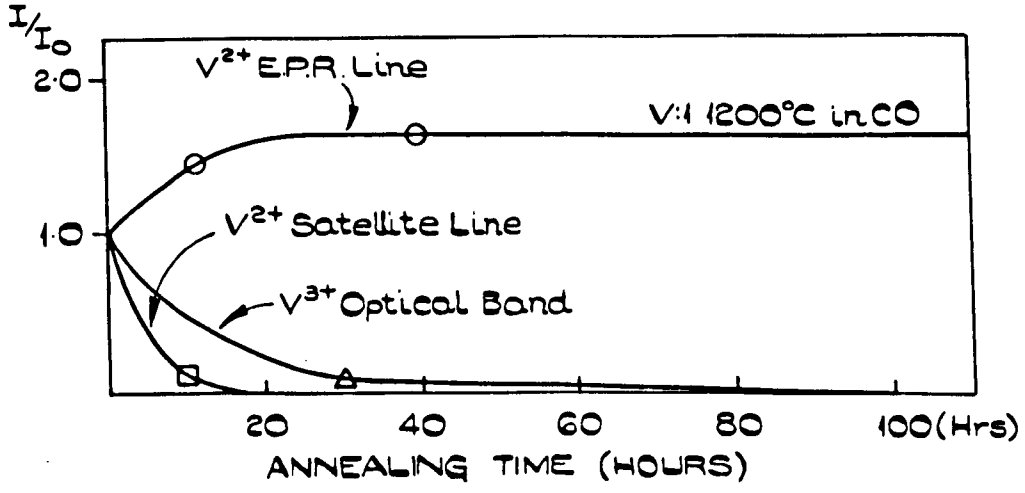

(b)

FIG. 5.21

EFFECT OF ATMOSPHERE ON (a) THE FLOW STRESS, (b) THE IMPURITY STATE OF CRYSTAL V:1

Additional obstacles are also present in the form of interstitial oxygen ions in close association with tetravalent vanadium ions.

The ageing behaviour below 1,000°C is characterised by an increase in concentration of trivalent ions as further clusters form, prior to nucleation of a precipitate lattice, leading to an increased flow stress, and vacancy pair condensation as dislocation loops, leading to an equivalently lower flow stress. The flow stress is thus compensated in this range, and is observed to increase only after 10 hours as a spinel dispersion is formed. The flow stress peak below 1,000°C is therefore attributed to a precipitation hardening-overageing behaviour.

Above 1,000°C the rapid growth of dislocation loops aids the formation of a coarse dispersion of spinel precipitate nucleated on dislocation segments, and the rapid fall in flow stress can then be directly correlated with the removal of obstacles in simple paired form from solid solution, and their incorporation in the spinel precipitate.

Interstitial oxygen diffusion undoubtedly takes place at high temperatures in oxidising atmospheres, but the resulting flow stress change is insignificant compared with the rapid softening associated with precipitate formation.

The effect of reducing anneals on the flow stress behaviour may be most plausibly explained by assuming that it is the simple ion clusters which are most mobile and which afford the greatest obstacle to dislocation glide. Under a reducing environment these clusters are broken up by reduction of vanadium ions to the divalent state,

and a consequent rapid drop in flow stress. Dispersal of more complex clusters, which affect the flow stress relatively less, proceeds more slowly, as shown by the gradual softening observed at longer ageing times.

5.4.f. Conclusions.

The obstacles to dislocation glide for various heat treatments may be listed as follows:-

1) Close paired impurities and vacancies.

These are evidently important obstacles to dislocation movement in the unaged state.

2) Cation-anion vacancy pairs and clusters.

These defects are present in as-grown crystals and are responsible for the initial flow stress behaviour of crystals after heat treatment

3) Precipitates.

The major part of the flow stress peak at 800°C is attributed to submicroscopic spinel precipitates, and the marked softening at 1,200°C is due to precipitation on dislocation dipole loops.

4) Interstitial oxygen

A <111> configuration of an interstitial oxygen ion - V^{4+} associate is partly responsible for the flow stress of as-grown crystals, and also provides a significant contribution to the flow stress at 1,500°C.

5.5. Chromium

Two melts were used:- Cr : 1, containing 600 p.p.m. and Cr : 2 containing 1,300 p.p.m. of chromium.

5.5.a. Flow Stress

The effect of heat treatment on the flow stress of as-grown crystals is shown in Fig. 5.22(a)(b) and Fig.5.22(c)(d) for crystals Cr : 1 and Cr : 2 respectively. It can be seen that the effect of isochronal and isothermal anneals is similar for crystals containing the two dopant levels, although the initial, as-grown, flow stress is much different and is consistent with the general behaviour observed for other systems.

5.5.b. E.P.R. Spectra

A great deal of information has been obtained previously on the charge compensating mechanisms of impurity incorporation for chromium ions in MgO from E.P.R. and optical luminescent spectral analysis. Fig. 5.24 shows typical extended spectra obtained from as-grown crystals of Cr : 1 and Cr : 2 at room temperature. It is apparent that the spectral line width is much wider in Cr : 2 than in Cr : 1, by a factor of three, a result of dipolar broadening at higher concentrations. In each case the spectral lines can be analysed in terms of the crystal lattice symmetry at the impurity site, i.e. octohedral, tetrahedral or rhombic,[45][76][77][78], corresponding to an isolated Cr^{3+} ion and an associated vacancy in (n.n.n.) <100> sites and (n.n.) <110> sites respectively. The lines corresponding to these symmetries are labelled Cr_o, T and R.

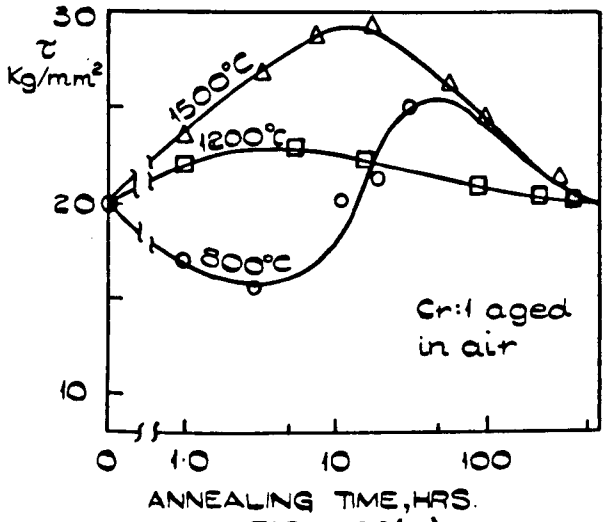

FIG. 5.22(a)

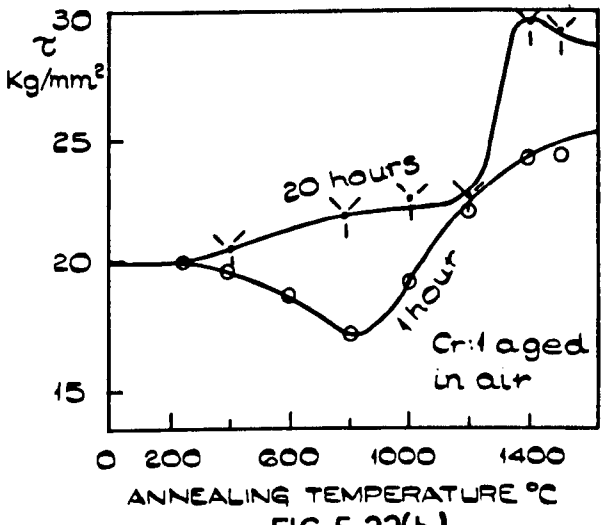

FIG. 5.22(b)

EFFECT OF HEAT TREATMENT ON THE FLOW STRESS OF Cr:1.

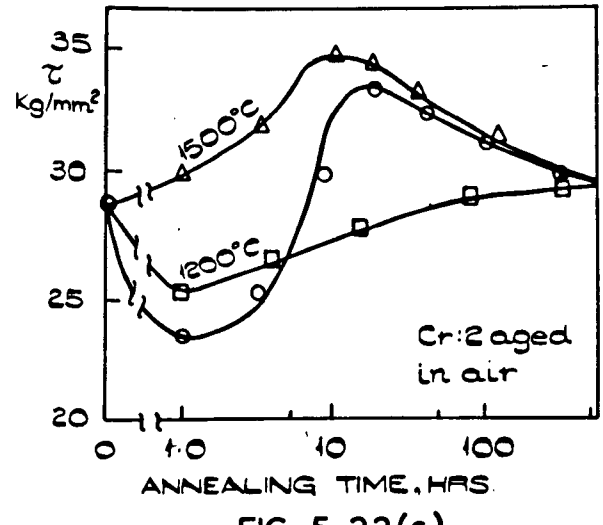

FIG. 5.22(c)

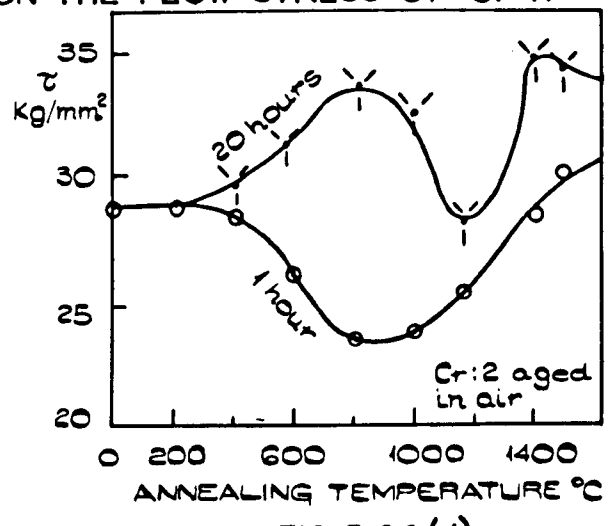

FIG. 5.22(d)

EFFECT OF HEAT TREATMENT ON THE FLOW STRESS OF Cr:2

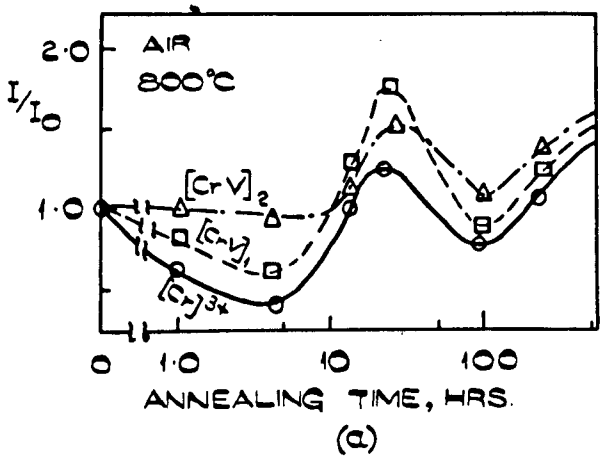

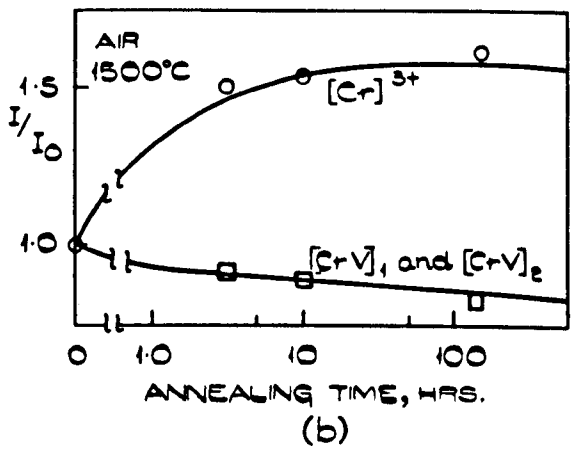

FIG. 5.23

THE RATIO OF THE INTENSITY OF E.P.R. SPECTRAL LINES, I, AFTER HEAT TREATMENT TO I_0 THE SIGNAL INTENSITY OF AS-GROWN Cr:1 CRYSTALS, (a) AT 800° C IN AIR (b) AT 1500°C IN AIR.

The strong central line labelled Cr_o close to g = 1.9797 is due to the isotopes $^{50}Cr^{3+}$, $^{52}Cr^{3+}$, $^{54}Cr^{3+}$ with nuclear spin I = 0 and is surrounded by a hyperfine quartet from the 9.5% abundant ^{53}Cr with I = $^3/_2$, not resolvable on the extended spectra.

In contrast to these isotropic lines due to Cr^{3+} in cubic symmetry, the spectrum due to a $[CrV]_1$ centre consists, in an arbitrary orientation, of nine lines, showing symmetry points about the three principal crystal axes. For an orientation such that a crystal cube axis is parallel to the static field H_o, as shown, the spectrum is composed of lines labelled T corresponding to centres with axes along the other two principal axes and consisting of coincident pairs. An additional line, labelled T' is centred upon g = 1.9782, indistinguishable from Cr_o in the full field spectrum, and correspond to impurity-vacancy pairs having axes along H_o. All these lines show a strong orientation dependence, and by suitably rotating the crystal appropriate coincidences occur at $\pi/4$ and $\pi/2$ symmetries. Each of the nine lines is composed of a hyperfine quartet from ^{53}Cr.

The lines labelled R consist similarly of orientation dependent pairs which are consistent with a defect having <110>type symmetry axes and are identified with $[CrV]_2$ type centres.

In addition to these strong lines, a number of weaker lines may be seen, especially in Cr : 2 crystals. These lines are considerably enhanced by ageing at low temperatures (400°C) for periods of the

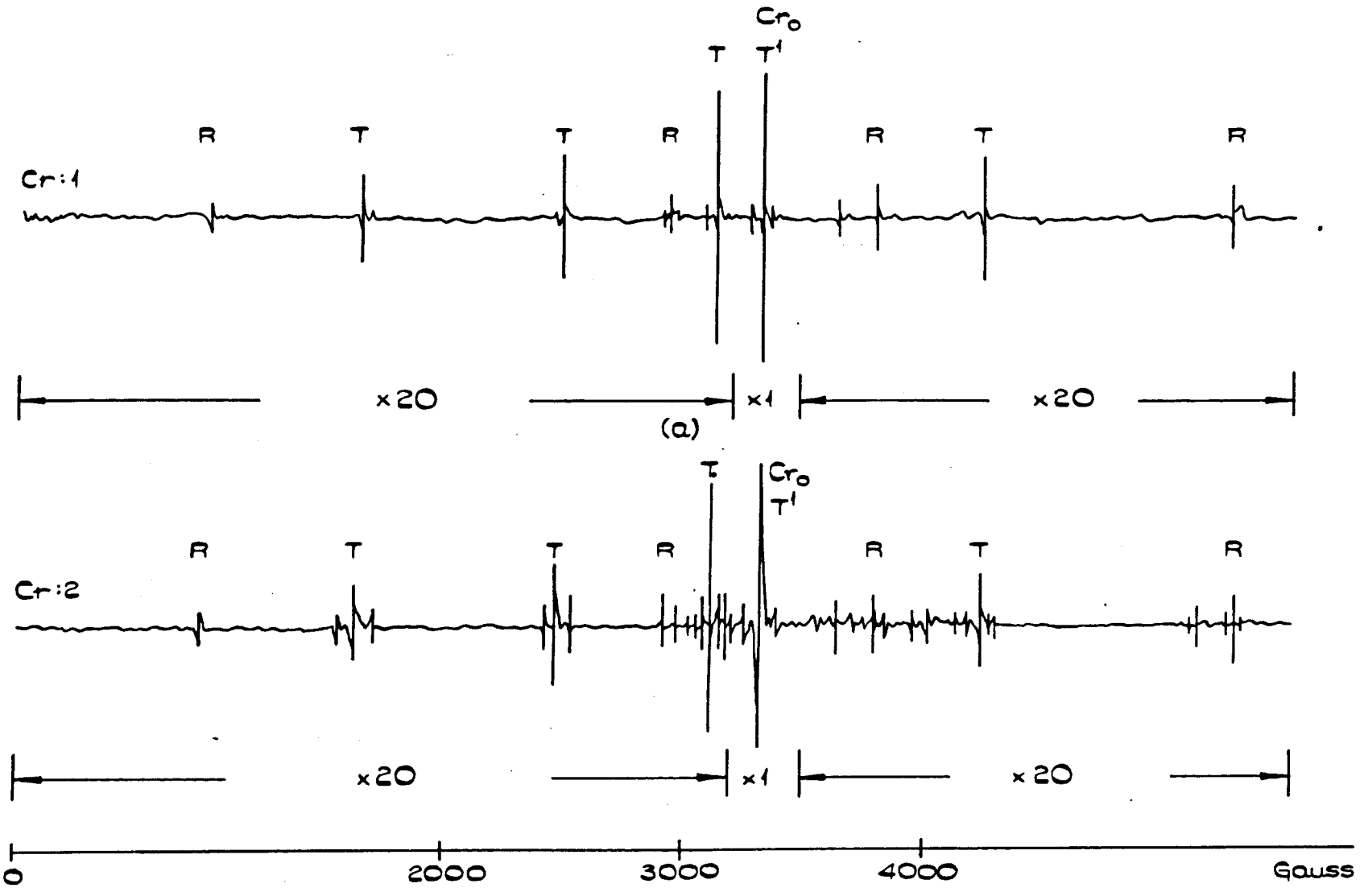

FIG. 5.24 E.S.R. SPECTRA OF Cr^{3+} IONS IN AS GROWN CRYSTALS (a) Cr:1 (b) Cr:2
Cr - CUBIC SYMMETRY IONS. T - TETRAGONAL SYMMETRY IONS.
R - RHOMBIC SYMMETRY IONS.

order of 800 hours, and are removed from the spectrum by ageing at temperatures above 800°C for one hour. The presence of "satellite" lines in the vicinity of the lines due to Cr^{3+} in tetragonal and rhombic symmetry showing a similar response to heat treatments has been previously recognised, and models for the centres responsible have been proposed, involving the association of two impurity ions with a single cation vacancy[46] E.P.R. lines of the type examined here are hence attributed to the centres $[Cr^{3+}VCr^{3+}]$, and $[Cr^{3+}VCr^{3+}]_2$.

It is evident from these spectra that only a fraction of impurity ions are bound in associated states, as observed for other ions. A consideration of the optical absorption spectra for chromium impurity is not worth while, since no previous study of the absorption bands due to impurity-vacancy complexes has been made, and the range of impurity centres is adequately covered by microwave spectroscopy.

5.5.c. Microstructural Observations.

An examination of crystals from both melts by electron microscropy shows that no detectable precipitation is evident in the as-grown state. Nor is precipitation of the spinel $MgCr_2O_4$ observed for heat treatments in excess of 1,000°C, as expected from the position of the solid solubility limit on the $MgO - Cr_2O_3$ phase diagram[79].

The development of a spinel lattice, visible only after 100-120 hours at 800°C is shown in Fig. 5.25 for crystal Cr : 2. These precipitates shown contrast typical of coherency strains and are in platelet or needle form. The total volume fraction of precipitate

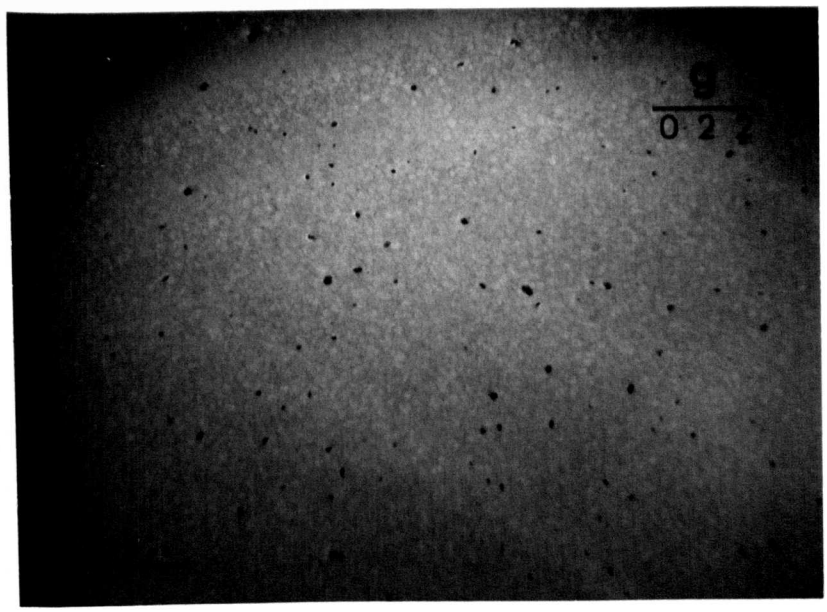

Fig.5.25(a)

Cr : 2 aged for 130 hours at 800°C in air.

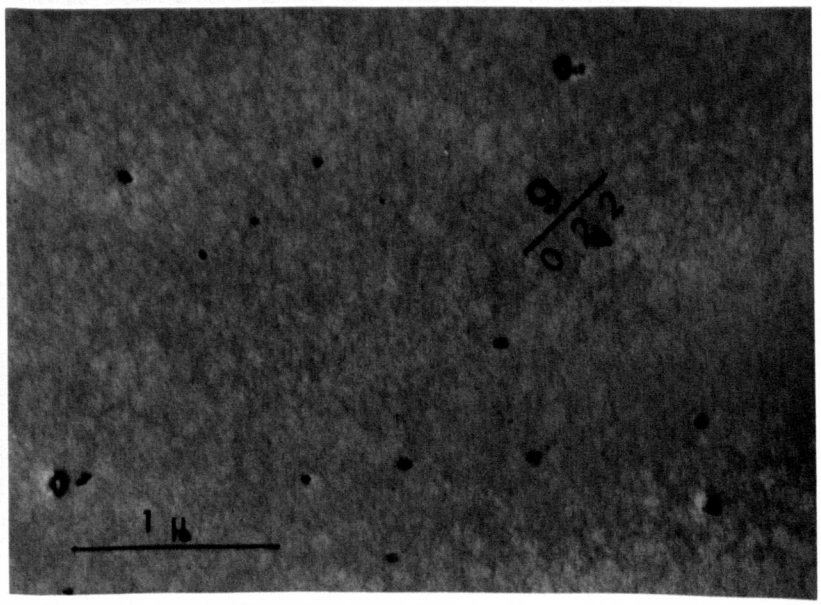

Fig.5.25(b)

Cr : 2 aged for 200 hours at 800°C in air.

is never sufficient in these specimens to allow confirmation of the precipitate structure to be made, but it is deduced to be that of spinel $MgCr_2O_4$, since a much coarser dispersion is detectable in Cr : 1 crystals and the known concentration of accidental impurities in Cr : 2 is not sufficient to produce the observed volume fraction of precipitate.

5.5.d Correlation of E.P.R. and Microstructural Observations

5.5.d (i) The Low Temperature Annealing Behaviour.

The ratio of the intensity of lines due to Cr^{3+} in [Cr], [CrV], $[CrV]_2$ type centres after an 800°C ageing treatment, to the intensity of each line in the as-grown state is shown for Cr : 1 in Fig.5.23.(a)(b) for anneals in air. A close comparison of these variations with the flow stress variations of Fig. 5.21 and Fig. 5.22 show several related features. The initial softening in this temperature range can be correlated with a similar decay in the intensity of emission from each centre, and the subsequent re-hardening with an increase in the intensity of ions in all the crystal field symmetry environments monitored, up to a maximum after 35 hours. The line intensity then decays and redevelops after prolonged treatments of 250-300 hours.

Annealing at low temperatures has a marked effect on the intensity of satellite lines which have been identified with [CrVCr] type centres. Treatment at 400°C for 1,000 hours increases the intensity of these lines by a factor of 15, linked with a proportional decrease in the intensity of lines due to simple asymmetric site ions, while the intensity due to cubic Cr^{3+} remains essentially constant. It

would appear from this that at low temperatures neutral complexes form by impurity association of the type:-

$2[Cr] + [V]_{Mg} \rightleftharpoons [CrV] + [Cr] \rightleftharpoons [CrVCr] \rightleftharpoons$ clusters, which play a predominant role in the formation of higher clusters. A significant increase in flow stress of crystals of Cr : 1 is produced by this treatment, of about 5 kg/mm^2 after 1000 hours at 400°C.

At higher temperatures, at which thermal dissociation of [CrVCr] type centres is observed, precipitate nucleation proceeds by the clustering of individual simple asymmetric centres, without the formation of an intermediate, electrostatically neutral [CrVCr] associate.

Two mechanisms are proposed to explain the initial decay in intensity of the microwave absorption and the decrease in flow stress at 800°C. Firstly a similar flow stress behaviour in other systems discussed has been attributed to the coalescence of anion-cation vacancy pairs present in the as-grown state. Vacancies of both types are expected to be present in doped crystals for charge compensation, and close-paired configurations inducing anisotropic lattice distortions would significantly affect dislocation mobility.

An alternative explanation may also be made in terms of a source of internal reduction incorporated during the growth process, which would also account for the observed spectral line behaviour. The simplest defect of this type is the F-centre, formed by dissociation during growth, giving a reaction of type:-

$$O^{2-} \rightleftharpoons O\ (gas) + \{[V_o] + \bar{\varepsilon}\} + \bar{\varepsilon}$$

During a subsequent annealing period formation of anion-cation

vacancy pairs leads to electron transfer to impurity centres. F - centres have been detected in pure crystals only after irradiation at g = 2.0023[44], but it is thought likely that the mechanism of charge compensation in crystals containing trivalent impurities, in which anion participation is possible, stabilises this defect. A spectrum from this electronic centre would be obscured by paramagnetic impurity lines close to g = 2.0023.

The low temperature flow stress peak apparent at 800°C in air can be correlated with an increase in the concentration of Cr^{3+} ions in both cubic and associated sites, prior to precipitate nucleation following oxidation of Cr^{2+} to Cr^{3+} as:-

$$2Cr^{2+} + O\ (gas) \rightleftharpoons 2Cr^{3+} + [V_{Mg}] + O^{2-}$$

Chromium Cr^{2+} ions are undetectable in the E.P.R. spectrum of as-grown crystals, but there is evidence for their existence in MgO from microwave ultrasonic paramagnetic resonance[80], and the disappearance of the Cr^{3+} ion spectra on solution treatment at 2,000°C in vacuum implies that a proportion of ions are present in this valence state.

The dimensions of pre-precipitate clusters of ions and vacancies formed by this aggregation is expected, from the ease of formation of the spinel lattice in MgO, to be only a few lattice spacings. Growth of the spinel particles continues up to resolvable dimensions after 100 hours. No paramagnetic spectrum from ions comprising a precipitate lattice is detected however, probably because of the close proximity of Cr^{3+} ions in the normal spinel lattice

which broadens the spectrum of individual ions below the limit of resolution through a dipolar interaction.

5.5.d.(ii) High Temperature Annealing Behaviour.

An apparent increase in the chromic ion concentration after extended (300 hours) anneals at 800°C, and an enhanced flow stress at 1,500°C in air is attributed, in addition to direct oxidation of Cr^{2+} ions, to interstitial oxygen diffusion, proposed by other workers[72] to lead to electronic transitions of the type:-

$O + Cr^{2+} \rightleftharpoons O^{-} + Cr^{3+}$ and

$O + [Cr] \rightleftharpoons O^{-} + [CrV]'$,

where $[CrV]'$ represents a [CrV] defect associated with a trapped hole which modifies the crystal field symmetry to give a smaller distortion at the chromium ion site. The second reaction leads to a decrease in the E.P.R. spectral intensity of [CrV] centres, the former gives rise to an enhanced isolated Cr^{3+} content.

The E.P.R. spectra variations for crystals aged at 1,500°C in air, shown in Fig.5.23 (b) indicates that the Cr^{3+} concentration in cubic site symmetry is enhanced by up to a factor of 1.5, while the proportion of ions in associated complexes decreases slightly with time. The high temperature behaviour is hence not attributable to the formation of impurity-vacancy pairs, but rather to the presence of the interstitial oxygen defect which distorts the lattice in the neighbourhood of Cr^{3+} ions, and hence broadens the E.P.R. spectral lines due to isolated Cr^{3+} ions.

The line width of impurity transitions are indeed found to be modified markedly at high temperatures. Short anneals at 2,000°C

in vacuum reduces the line width of the Cr^{3+} cubic transition from an as-grown value for Cr : l of 8 gauss to less than .4 gauss as clusters of ions are dispersed and reduced. Anneals at 1,500°C in air increase the width of the same line to 20 gauss, consistent with the strain produced by an associated interstitial oxygen ion. The green colouration of crystals subjected to this treatment is much deeper, consistent with an overall increase in the concentration of chromic ions.

The decay in the flow stress peak for longer ageing times at 1,500°C is due partly to the dissociation of impurity-cation vacancy centres, and partly to direct vacancy-interstitial annihilation, or alternatively to a clustering of the centres containing interstitials to form larger non-asymmetric clusters.

5.5.d.(iii) Anneals in Reducing Atmosphere

The effect of atmospheric oxygen partial pressure is less marked for chromium impurity than for any others investigated.

After a solution treatment for one hour at 2,000°C in vacuum, the spectra of chromic ions shows a 20% decrease in the concentration of isolated Cr^{3+} ions, while the tetragonal site concentration drops to a half of its original, as-grown value. Coupled with this is a decrease in flow stress of 10 kg/mm^2. The most logical explanation for this is the reduction of chromic ions in the low oxygen partial pressure furnace atmosphere, with an accompanying anion vacancy formation.

$$2\ Cr^{3+} + O^{2-} \rightleftharpoons 2\ Cr^{2+} + [V_o] + O\ (gas)$$

with an observed colour change; from clear green, (due to chromic

ions), to colourless after this treatment.

The effect of heat treatments in CO atmospheres at lower temperatures on dislocation mobility, and the simultaneous variation in spectral intensity of chromic ions is shown in Fig. 5.26 and Fig.5.27 respectively. The decay of the E.P.R. spectral lines with time at 800°C and 1,200°C is consistent with a gradual reduction of Cr^{3+} ions in isolated and associated states, with the exception of the $[Cr^{3+}]$ centre at 800°C up to 100 hours. The anomalous behaviour in this case is possibly the result of electron transfer to accidental impurity ions, e.g. iron, which is obscured by the dominant impurity spectrum.

An electron microscope examination of specimens prepared from crystals aged in CO shows no precipitates of resolvable dimensions are present, even after extended anneals. The reduction of chromic ions evidently suppresses formation of the spinel lattice.

Flow stress variations after reduction are in agreement with the obstacles proposed for as-grown crystals. At 1,200°C the flow stress falls rapidly to a fairly constant value after 10 hours, coupled with a decay in the concentration of asymmetric impurity sites over the same period by reduction of impurities to a divalent state. At 800°C the flow stress falls less sharply, and then recovers, showing a slight reversed dependence up to a maximum after 20 hours. This behaviour is interpreted as the nucleation and growth of spinel precipitates, unresolvable in the electron microscope, from existing trivalent chromium ion clusters. These particles are

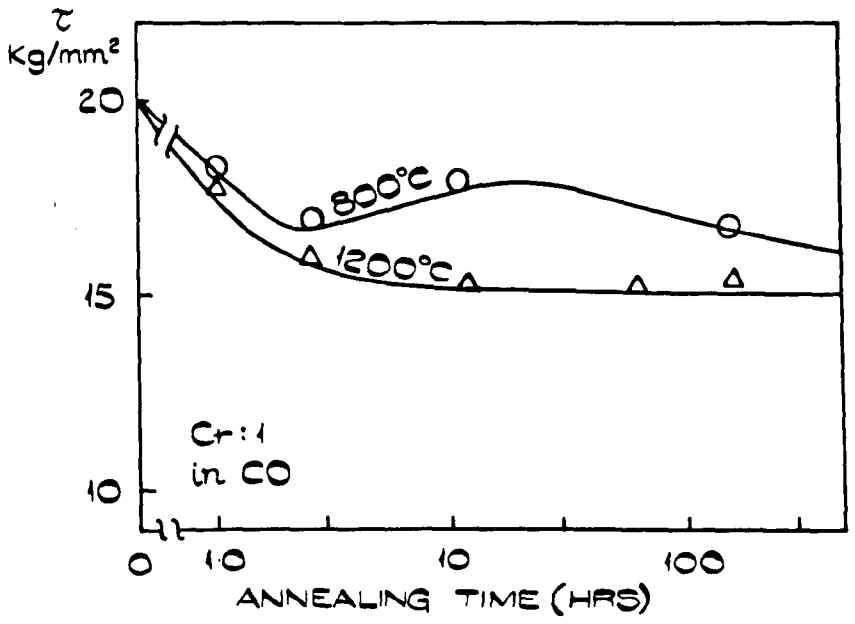

FIG. 5.26

EFFECT OF HEAT TREATMENT IN REDUCING ATMOSPHERES ON THE FLOW STRESS OF Cr:I.

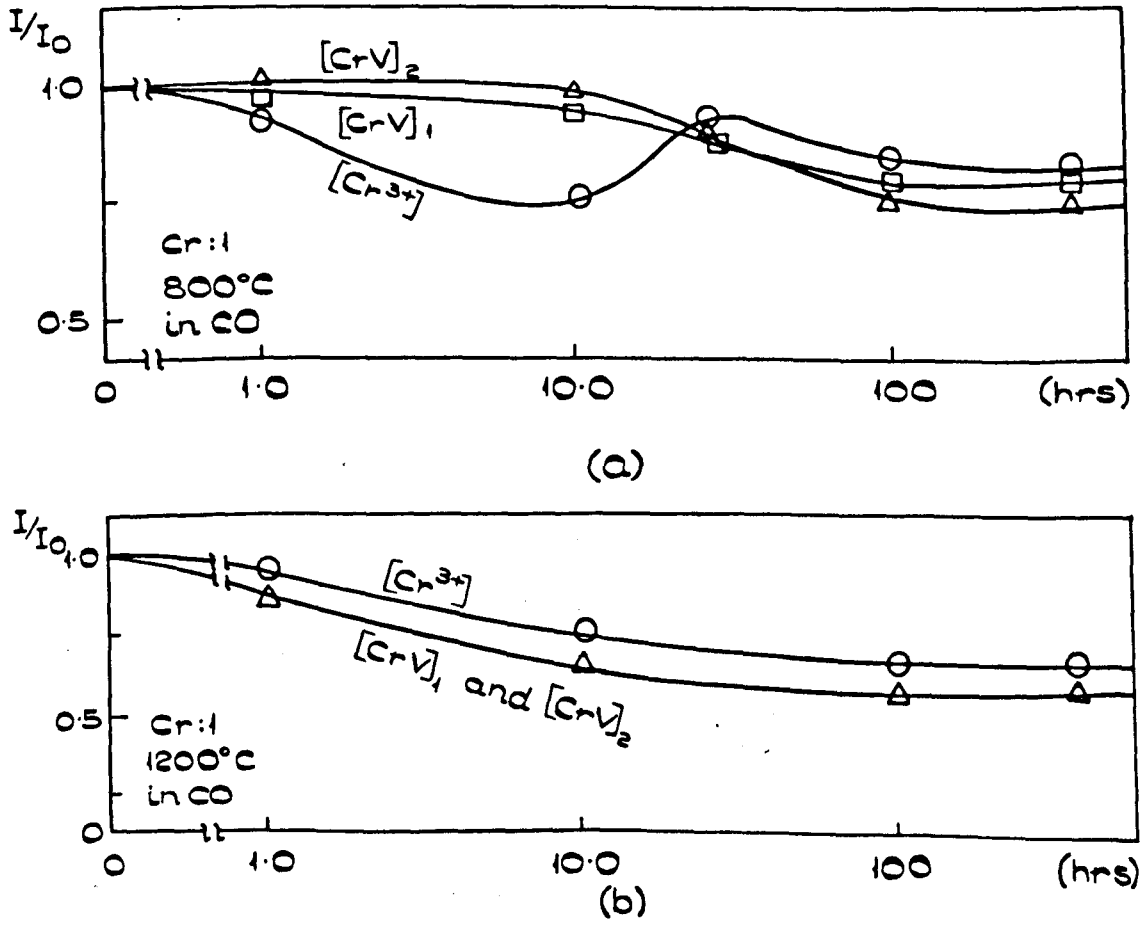

FIG. 5.27

EFFECT OF HEAT TREATMENT AT (a) 800° C (b) 1200°C IN CO THE E.P.R. SPECTRUM OF Cr:I.

redissolved on annealing further by conversion of the trivalent ions in the spinel lattice to the divalent state.

5.5.e. Conclusions

The defects responsible for particular features of the flow stress features of the flow stress behaviour are listed briefly as follows:

1) Impurity-vacancy pairs and simple clusters.

These defects are responsible for a significant portion of the flow stress of as-grown crystals. The flow stress maximum for anneals in air at temperatures less than 1,000°C is also partly caused by cluster formation.

2) Anion-cation vacancy pairs.

Aggregation of vacancy pairs is partly responsible for the initial softening at low temperatures, but the vacancy supersaturation is insufficient for loop nucleation.

3) Spinel precipitates.

The low temperature ageing peak is attributed, in part, to a spinel precipitate dispersion.

4) Interstitial oxygen

The existence of an interstitial oxygen species is in concordance with observed E.P.R. spectra and is believed to be responsible for the high temperature ageing peak in oxidising atmospheres. Under reducing atmospheres, as expected, no similar effect is detectable.

5.6. Pure Crystals

On the basis of the results presented in this chapter it has been possible to identify the defects responsible for the high and low temperature ageing behaviour of crystals containing an intentionally added impurity. These defects are seen to have quite general application, suggesting that similar features in nominally pure crystals may be explained in the same way, in spite of the lack of consistent experimental evidence found in previous work. In this section the conclusions made so far are applied to the problem of the effect of heat treatment at high (1,500°) and low (800°C) temperatures on the flow stress of pure crystals.

Two crystals were used: - P : 1 containing 400 p.p.m. of undetermined impurities, and P : 2 with a purity level of less than 100 p.p.m. The major impurity constituent in P : 1 determined by analyses of other crystals prepared from the same source material, is expected to be calcium (200 - 300 p.p.m), whereas this impurity is present as a trace element only in P : 2.

The ageing behaviour of these crystals is shown in Figs.5.28 and 5.29. In these curves the most notable feature is that the as-grown flow stress of P : 2 is nearly twice that of P : 1, although the impurity level is higher in the latter crystals. The ageing behaviour is also different in the low temperature range. In particular, the marked initial age softening found for crystals of P : 2 at low temperatures is much less noticeable in P : 1.

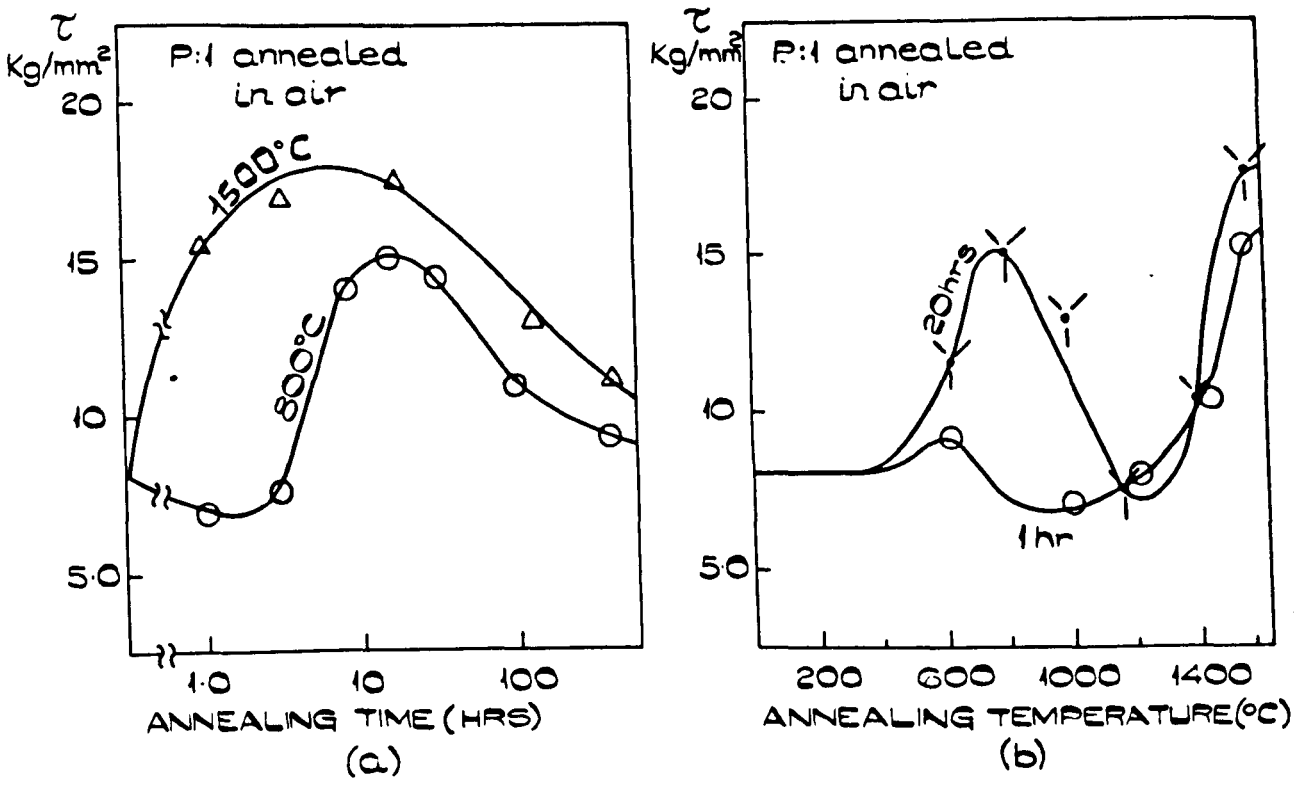

FIG.5.28

EFFECT OF HEAT TREATMENT ON THE FLOW STRESS OF CRYSTAL P:1.

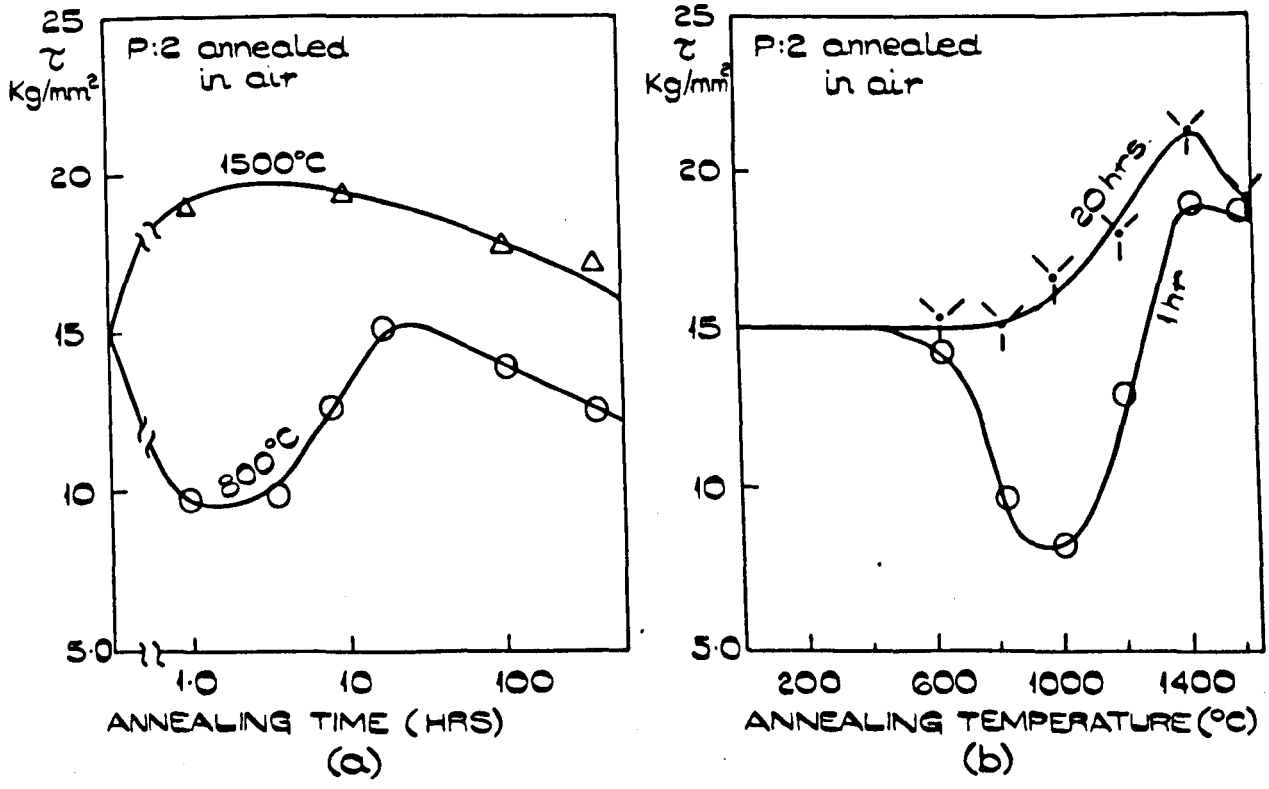

FIG. 5.29

EFFECT OF HEAT TREATMENT ON THE FLOW STRESS OF CRYSTAL P:2.

Nevertheless a low temperature peak is observed in both cases.

In the absence of a chemical determination of the impurities in the crystals supplied a qualitative analysis was made by E.P.R. In crystals P : 1, Fe^{3+} and Cr^{3+} in both octohedral, and in smaller concentrations, asymmetric crystal fields are detectable together with a small proportion of Mn^{2+} ions. In contrast, no trivalent impurities are present in crystal P : 2, although a significant level of V^{2+}, and to a lesser extent, Mn^{2+} is resolvable. Because of the small concentrations of these ions, no consistent variations are found in the intensity of the E.P.R. spectra with heat treatment.

A very low resolvable precipitate density is found after heat treatment of both crystals, definitely not of sufficient density to preceptibly affect the flow stress.

Differences in behaviour of the two crystals can be explained on the assumption that the flow stress of crystal P : 1 is controlled by impurity vacancy pairs and simple clusters, and the flow stress of P : 2 is determined to a large extent by cation-anion vacancy pairs. It is the higher concentration of vacancy pairs in the latter case which is responsible for the high flow stress, in the absence of a significant concentration of trivalent impurities.

On ageing at 800°C, vacancy pair combination occurs, producing the observed plastic softening in P : 2. In both crystals impurity clustering during this treatment as submicroscopic spinel particles

is responsible for the re-hardening after longer ageing times. The magnitude of the precipitation hardening peak is equivalent in the two crystals, and it is concluded that although the volume fraction of spinel precipitates is larger in P : 1. a finer scale of dispersion is nucleated in P : 2 because of the higher vacancy concentration in this crystal. The effect of vacancies on the nucleation of spinel precipitates is discussed further in 6.7.

The high temperature ageing peak at 1,500°C in air is attributed in both cases to oxygen incorporated interstitially in the lattice, in concordance with the conclusions made earlier.

The annealing behaviour of both pure and doped crystals is thus explicable in a qualitative way in terms of the defects proposed. In the next chapter, calculations based on various models for these defects are used to evaluate their relative contributions over the annealing ranges considered.

6. A DISCUSSION OF STRENGTHENING MECHANISMS IN DOPED MgO.

The observations of Chapter 5 confirm the expected 'structure sensitivity' of the flow stress arising from variations in the state of dispersion of impurity ions in MgO. In this chapter theories applicable to various forms of strengthening by dispersed defects are reviewed and, where possible, quantitative estimates of the flow stress, for comparison with the measured values, are obtained by combining the theories with the experimental observations of Chapter 5.

6.1. Obstacles in the form of Substitutional Ions.

A simplification may be made for substitutional ion obstacles by neglecting interaction forces at distances greater than one lattice spacing. This is justified both by the short range nature of the forces involved and, more important, a cancellation of the wide spectrum of background forces of both positive and negative sign when the interactions are averaged over a number of obstacles.

The effective planar obstacle spacing experienced by a dislocation line is not necessarily the average planar interparticle spacing, since sections of a pinned dislocation segment may bow out under the external stress and contact fresh obstacles. The effective spacing S of the pinning points, determined by the extent of dislocation flexibility, is given by the Friedel relation[81].

$$S = \left(\frac{\mu b}{N\tau}\right)^{\frac{1}{3}}$$

where τ is the critical shear stress, N the density of pinning centres

and μ the shear modulus.

Fleischer[33] has pointed out that defects may be classed into two separate catagories as 'gradual' or 'rapid' hardeners depending on the strength of the interaction with dislocations. The magnitude of the interaction is found to be related to the symmetry of the lattice distortion at the defect site. Strong hardeners, having a large dislocation interaction energy, are centres associated with asymmetric strain fields, while gradual hardeners result from symmetrical distortions.

6.1.a. Weak Obstacles

Two separate effects are important in determining the interaction energy of a dislocation with an isolated substitutional impurity atom. The first term involves an interaction between the symmetrical strain field in the region of the misfitting atom and the hydrostatic stress field of the dislocation, which for a screw dislocation is very small. The second interaction is due to differences in elastic properties in the region of the impurity atom which affect the self-energy of the dislocation line.

Fleischer[82] has derived an expression for the increase in flow stress for a dispersion of substitutional centres of this type on the basis of these two effects, which simplifies, if the mismatch of atomic moduli is neglected, to

$$\Delta\tau_{(r)} = \frac{\mu\,\varepsilon_s^{3/2}\,c^{1/2}}{760}$$

where μ is the shear modulus of the matrix (12.2×10^{11} dynes/cm^2)

C the concentration of defects and ε_s is an atomic misfit parameter given by

$$\varepsilon_s = \left| \frac{Rs}{Rm} - 1 \right|$$

where R_s and R_m are the radii of the impurity ion and solvent ion respectively. For all impurities considered in this research, the value of $\Delta\gamma$ may be calculated as $\Delta\gamma \lesssim 0.2$ kg/mm^2, less than the observed flow stress by nearly two orders of magnitude. The effect of a modulus difference in the region of an impurity ion is not expected to affect the conclusion that the contribution of isolated impurity ions may be neglected in a consideration of the flow stress of MgO.

6.1.b. Strong Obstacles.

A strong interaction with both edge and screw dislocations for impurity-vacancy pairs arises from the asymmetric nature of the strain field induced by defects of this type. In the treatment given by Fleischer[6], the dislocation line is considered to be completely flexible up to the radii of curvature comparable with the mean defect spacing. In this case the effective defect spacing S is also the average nearest neighbour spacing L, and

$$S = \frac{b}{\sqrt{2c}}$$

where C is the concentration of tetragonal defects and only defects on either side of the glide plane are considered.

At 0°K, thermal activitation over the flow stress barrier is absent, and the flow stress increment at this temperature is given by:

$$\Delta \gamma_{M(r)} = \frac{F_o}{b\ L}$$

In this equation F_o is the maximum force experienced by the dislocation at the defect, and is derived by maximising the first derivative of the interaction energy with respect to motion along the slip plane. The interaction energy between a dislocation and an anisotropic distortion is calculated by multiplying the stress tensor of a dislocation with the appropriate strain tensor of the defect. For a defect in general orientation this gives:-

$$F_o = \frac{\mu \Delta\varepsilon\, b^2}{a}$$

where $\Delta\varepsilon$ is a measure of the lattice anisotropy and a is a constant depending on the orientation of the defect, with respect to the dislocation line. The value of this quantity is approximately the same for defects in different orientations, and is assumed to be that calculated for $\langle 110 \rangle$ type defects in LiF, where a = 3.86. Hence

$$\Delta \gamma_{m(r)} = \frac{\mu \sqrt{c}\, \Delta\varepsilon}{3.3.} \qquad - 6.1.$$

In this equation the effective spacing of defects on both sides of the slip plane are considered, and two-thirds of the total concentration of defects are assumed to interact strongly with a glide dislocation i.e.

$$S = \frac{b}{\left(\frac{4}{3}c\right)^{\frac{1}{2}}}$$

The relation between the force experienced by a dislocation and its

distance x from the defect was taken by Fleischer to be given by the function

$$F(x) = \frac{Fo}{\left(\frac{x}{b} + 1\right)^2}$$

giving an activation energy required to overcome the obstacle as

$$U = F_o b \left[1 - \left(\frac{\Delta\gamma_F}{\Delta\gamma_M^{(0)}}\right)^{\frac{1}{2}} \right]^2 \qquad - 6.2.$$

where $\Delta\gamma_F$ is the flow stress at a finite temperature which is related to the activation energy by some multiple α of kT. The constant α hence represents the degree to which thermal fluctuations aid the dislocation over the stress barrier, i.e.

$$U = \alpha kT \qquad - 6.3.$$

The temperature dependence of the flow stress may then be written as:

$$\left(\frac{\Delta\gamma_F}{\Delta\gamma_M^{(0)}}\right)^{\frac{1}{2}} = 1 - \left(\frac{T}{T_o}\right)^{\frac{1}{2}} \qquad -6.4.$$

The importance of defects of asymmetric nature in monovalent lattices is well established, and the observed flow stress behaviour has been shown to be in general agreement with the predictions of Fleischer's model at sufficiently low temperatures. The contribution of impurity-vacancy pairs in MgO may be evaluated in a similar way, using the concentration determined by E.P.R. methods and the temperature dependence measured in 6.8, and correlated with the observed flow stress variations. This is carried out in 6.4.

6.2. Electrostatic Interactions

In ionic crystals where the relative concentrations of anion and cation

vacancies differ, an equilibrium line charge is built up on moving fresh dislocations, which is given by the net line density of jogs. It has been established from measurements of surface potential during plastic deformation that the charge is positive for MgO and negative (of magnitude 6.0×10^{-4} e.s.u/cm) for NaCl[83]. A possible source of hardening thus arises from an electrostatic interaction between charged dislocations and impurities or vacancies.

An estimate of the magnitude of this interaction may be made by calculating the stress required to detach a charged dislocation line from a charge-compensating cloud using the treatment of Eshelby et al[84], where the force necessary for detachment from an equilibrium atmosphere is given by:-

$$\Delta\tau_{(n)} = \frac{0.8\sigma^2}{\varepsilon b}\left\{\frac{8\pi e^2 c N}{\varepsilon kT}\right\}^{\frac{1}{2}}$$

where ε is the static dielectric constant for the crystal, e is the electronic charge, c is the concentration of impurity ions, σ is the linear charge density in e.s.u/cm, and in the absence of an experimental determination of this quantity in MgO, the value determined for NaCl is taken to give:-

N the number of cation sites per cm^3

$$\Delta\tau \lesssim 0.2 \text{ kg/mm}^2$$

Hence the electrostatic interactions are of negligable importance in a consideration of flow stress variations in MgO.

6.3. Dislocation Loop Hardening.

Various calculations have been made which are applicable to the hardening by loops and vacancy clusters observed experimentally in MgO.

Kroupa and Hirsch[85] calculated the hardening by a dislocation loop dispersion by estimating the average elastic interaction between a straight dislocation and a loop and applying Freidel's modification for the effective distance between obstacles along the line to derive:-

$$\Delta\tau_{cr} = \frac{\mu b N^{\frac{2}{3}} d}{16}$$

where N the loop density, and d the loop diameter.

Freidel[81] estimated the strength of locking by loop segments of glide dislocations trapped by attractive junction reactions giving:-

$$\Delta\tau_{cr} = \frac{\mu b N^{\frac{2}{3}} d}{8}$$

Both these models give yield stress values which are appreciably lower than the observed flow stresses of loop hardened metals. The detailed movement of a dislocation line through a random array of loops has been studied using a computor simulation programme[86], for a junction locking model consisting of a range of obstacle strengths, and a value obtained for the shear stress as:

$$\Delta\tau_{cr} = \frac{\mu b N^{\frac{1}{2}} d^{\frac{1}{2}}}{4.0} \qquad - 6.6.$$

The most applicable model for small loops in that developed by Fleischer[33], which regards each loop as a centre of tetragonal lattice distortion, for which

$$\Delta\tau_{cr} = \frac{\mu b N^{\frac{1}{2}} d^{\frac{1}{2}}}{3.7} \qquad - 6.7.$$

These latter two models have been found to give values for the critical shear stress consistent with experimental results for quenched and irradiated materials, over a range of loop radii, and are therefore used in this analysis.

For the loops observed in aged crystals e.g. V : 1, the maximum

additional flow stress after 60 hours at 800°C caused by a dislocation loop dispersion of density $N = 1.8 \times 10^{14}/cm^3$, and mean loop diameter $d = 3.5 \times 10^{-6}$ is calculated as $\Delta\tau = 4.9$ kg/mm^2.

6.4. Precipitation Hardening

This section is concerned with obstacles to dislocation motion in precipitate form. The precipitate structure considered is the spinel lattice appropriate to the major impurity of each system. A dislocation may by-pass precipitates in its glide plane by bowing between them or by shearing the precipitate structure. Both mechanisms give rise to an increase in shear stress, the magnitude of which depends on the parameters of the dispersion.

6.4.a. Models for the Flow Stress Based on Particle Shearing.

The effect of a spinel precipitate distribution in impeding slip at room temperature can be conveniently divided into long and short range interactions.

Long range stress interactions due to elastic misfit stresses in the matrix are caused by a lattice mismatch at the particle-matrix interface. An estimate of the significance of hardening from this interaction may be made for a dispersion of coherent spinel precipitates by using the simple theory of Mott and Nabarro[87].

The flow stress is assumed to be controlled by an average lattice strain evaluated at half the average interparticle spacing and given by:-

$$S = 8\varepsilon r_o^3 N.$$

where N is the precipitate density and ε a misfit parameter for a spherical particle r_o. Assuming a value of Poisson's ratio (ν) for

MgO of $\nu = 1/3$, then $\varepsilon = 2/3\,\delta$. In this equation δ is the fractional difference in lattice parameter of the two lattices given by:- $\delta = \left| 1 - \frac{a_s'}{a_m} \right|$

where a_s and a_m are the lattice spacings of the free spinel and matrix structures respectively. The flow stress can then be identified with this mean elastic strain field, giving a critical shear stress:-

$$\Delta\tau_{\bar{s}} \simeq 8\mu\varepsilon r_o^3 N$$
$$= 2\mu\varepsilon f \qquad -6.7$$

where f is the volume fraction of precipitate. In Table 6.1. is given the total volume fraction of spinel precipitate for each major impurity used, and the corresponding flow stress increment using the above equation. This calculation represents therefore the maximum flow stress increment possible from this contribution.

System	Cr : 1	Fe : 1	Ti : 1		Vi : 1	
spinel impurity	$MgCr_2O_4$	$MgFe_2O_4$	$MgTi_2O_4$	Mg_2TiO_4	Mg_2VO_4	MgV_2O_4
f	9.4×10^{-4}	1.4×10^{-3}	1.6×10^{-3}	3.1×10^{-3}	4.8×10^{-3}	2.5×10^{-3}
	7.3×10^{-3}	5.2×10^{-3}	3.8×10^{-3}	1.6×10^{-3}	2.8×10^{-3}	1.03×10^{-3}
$\Delta\tau$ (kg/mm^2)	0.4	0.4	0.4	0.4	0.8	0.2

Table 6.1.

It is clear from this analysis that, although the theory used is an approximation applicable to small particle spacings only, the flow stress of doped MgO is not determined by the stress required to overcome the long range elastic strains caused by precipitates. Long range interaction effects may thus be effectively ignored, and it is necessary to discuss the effect of short range interactions produced when a glide dislocation shears the precipitate.

The geometry of dislocation glide in spinel crystals is known to depend on the extent of deviation from stoichiometry. The prediction of Hornstra[88] that slip at the stoichiometric composition should be of the type $\{111\}\langle 110\rangle$ has been verified by macroscopic plastic flow observations. With increasing deviation from stoichiometry, the flow stress on the system $\{110\}\langle 1\bar{1}0\rangle$ becomes much lower, and glide on this alternative system is observed. Dislocation glide in a number of spinels near the stoichiometric composition and over a range of non-stoichiometry has been analysed by electron microscopy, and the glide dislocations found to be composed of coupled partials of Burgers vector $\frac{a_s}{4}\langle 110\rangle$ [89]. A unit dislocation in the MgO lattice thus becomes a partial inside the precipitate, and the stress necessary to shear a spinel precipitate particle is then determined by the energy of the antiphase boundary produced in the ordered cation sublattice by a unit matrix slip dislocation.

An examination of the phase diagrams for some of the spinel precipitates investigated here e.g. MgO - Fe_2O_3 [13], MgO - Cr_2O_3 [79], MgO - TiO_2 [90], and the observation that deviation from stoichiometry with excess Mg^{2+} ions is rarely observed, suggests that for the ageing temperatures used in

this study ($\leq 1,500^{\circ}C$), precipitation of spinel close to the stoichiometric composition is to be expected. A glide dislocation may either pass through particles on {110} planes as observed in non-stoichiometric specimens or on {111} planes for specimens close to the stoichiometric composition. In the latter case a jog is formed in the dislocation line for each particle sheared.

One possible estimate of the increment in stress for a particle shearing mechanism may be made by using a simple energy balance argument in which the work done in moving a dislocation is equated with the energy of formation of an antiphase boundary.

The separation of the partial dislocations in spinels close to the stoichiometric composition is observed to be of the same order as the dislocation width i.e. 50 - 100 Å. The magnitude of the antiphase boundary energy is then given by the equilibrium between the mutual repulsive force of two coupled dislocations of collinear Burgers vector $\frac{a_s}{4}\langle 110\rangle$, assumed to be in screw orientation, and the surface tension of the stacking fault.

$$\text{i.e.} \qquad \gamma = \frac{\mu b^2}{2\pi D} \qquad - 6.8$$

where D is the width of the stacking fault, and the shear modulus of spinel is given by a representative value for the spinel Fe_3O_4 i.e. 9.7×10^{11} dynes/cm^2.

The antiphase boundary energy is then found to be $\gamma = 140 - 280$ ergs/cm^3.

An upper limit to the antiphase boundary hardening by spinel

precipitates may be calculated for a sufficiently fine dispersion of precipitate for the dislocation to be treated as a rigid line by equating the work required to move the dislocation a distance δ along a slip plane which is intersected by particles of average effective separation $\bar{l}$ and mean diameter $\bar{d}$ to give:-

$$\gamma_A b^2 \frac{\bar{d}}{\bar{l}} = \gamma b \bar{l}$$

where $\bar{l}/\bar{d}$, is the mean fraction of the dislocation length lying within a precipitate[91].

For spherical particles these averaged quantities give the equation

$$\Delta\gamma_A = \frac{\gamma (f\pi)^{\frac{1}{2}}}{b} \qquad -6.9$$

The increase in flow stress due to antiphase boundary hardening using this equation, and assuming that all the impurity is in spinel precipitate form,

System	Cr : 1	Fe : 1	Ti : 1		V : 1	
precipitate spinel	$MgCr_2O_4$	$MgFe_2O_4$	$MgTi_2O_4$	Mg_2TiO_4	MgV_2O_4	Mg_2VO_4
$\Delta\gamma_A$	8.6.	10.2.	11.2.	15.5.	14.0.	18.1

Table 6.2.

is tabulated in Table 6.2 for each impurity, and represents an upper limit for hardening of this type. It is clear that on the basis of antiphase boundary hardening alone, all the precipitate present in aged MgO

is sheared at the experimentally observed flow stress. It should be pointed out that dislocations are mobile in the spinel lattice only at temperatures above 1,600°C at the stoichiometric composition[92]. This is the result of a 'synchro-shear' process proposed for dislocation glide on {111} planes, involving the synchronous movement of cations in the dislocation core to normally vacant sites[88]. A precipitate shearing mechanism at room temperature would therefore be applicable to a consideration of particles of only a few lattice spacings in dimension. It is possible that although a precipitate shearing mechanism may be applicable in some systems in the early stages of ageing, as the dispersion coarsens the mechanism will be that appropriate to dislocation bowing.

6.4.b Dislocation Bowing

The suggestion that for sufficiently wide particle spacings, dislocations could by-pass obstacles by bowing between them, leaving each obstacle surrounded by a dislocation ring, was first made by Orowan[93]. The yield stress is then determined by the stress required to bow dislocations between the particles against the dislocation line tension T up to a radius ρ equal to half the mean interparticle spacing.

The applied stress required to support the dislocation line in this position is then given for particles of spacing $2R_s$ by:-

$$\tau_{or} = T/\rho b = T/bR_s$$

For ~~screw~~ edge dislocations, the contribution of precipitates of radius r_s and average particle spacing $2R_s$ due to Orowan hardening is given, using the more accurate estimate of line tension derived by Nabarro[94] as:

$$\Delta\tau_{b(r)} = \frac{\mu b}{4\pi(1-\nu)} \cdot \frac{1}{R_s - r_s} \cdot \ln\left\{\frac{R_s - r_s}{b}\right\} \qquad \text{- 7.10}$$

where the interparticle spacing on the glide plane $2R_s$ and the mean precipitate radius intersected by a random plane, r_s is related to the total volume fraction f_s of a random precipitate distribution as:-

$$2R_s = 1/2 \cdot \sqrt{\frac{\pi}{f}} \cdot r_s$$

where $r_s = \sqrt{\frac{1}{3}}\, r_v$, the precipitate radius.

The possibility of cross-slip over distances comparable to the particle radius is unlikely at room temperature. In MgO dislocation mobility on the cross-slip planes $\{111\}$ and $\{100\}$ is very low for temperatures less than $1,500^{\circ}C$, since glide on these systems with slip vector $\frac{a_m}{2}\langle 110\rangle$ results in a juxtaposition of like charges, creating a high energy electrostatic fault. The effect of cross-slip at higher temperatures is to increase the term r_s in the Orowan relation, leading to a reduction in flow stress. In view of the above discussion cross-slip is neglected for the purposes of this investigation.

6.4.c Dislocation Configurations in Deformed Crystals.

It has been suggested that in MgO crystals hardened by a dispersed spinel phase, precipitates do not deform with the matrix, and that the observed yield stress increment due to a precipitate dispersion is that predicted by an Orowan mechanism, in which dislocations by-pass precipitates by bowing between them. This results in a dislocation loop being left in the glide plane around precipitate particles after the passage of a glide dislocation. An investigation has been made of the dislocation distributions in strained crystals in the as-grown state, and containing a spinel precipitate dispersion, in order to obtain evidence for Orowan

glide loops remaining after deformation. A considerable difficulty exists in a study of this nature, since MgO exhibits only a limited plasticity in compression at room temperature, (less than 2%), and for small particle sizes precise interactions between dislocations and particles are not clearly observable.

The micrograph in Fig. 6.1 illustrates the arrangement of dislocation in a (100) section of a crystal of Ti : 1 aged at 800°C to obtain a coarse precipitate dispersion. The specimen thickness is 1.2μ, and the dislocation configuration on the inclined (45°) glide band shown is hence likely to be typical of the bulk crystal. The slip band can be seen to consist of a number of narrow elongated edge dislocation dipoles lying parallel to a ⟨001⟩ direction, and showing weak contrast due to overlap of the strain fields of the component dislocations. The presence of unresolvable pairs may in many cases be inferred from the appearance of cusps in otherwise straight screw dislocation lines. A similar dislocation debris is observed in as-grown crystals. The origin of these cusps and trailing dipoles can be attributed to jog formation and accumulation as the parent screw dislocation moves forward.

In deformed cyrstals containing coarse precipitate dispersions additional features are observed, as shown in Fig. 6.1, consisting of small loops which can clearly be seen to encircle precipitates. These observations indicate that particles are not sheared by matrix dislocations, and are consistent with a deformation process in which dislocation movement occurs by an Orowan, or possibly a modified Orowan[95], mechanism. This is in accord with the conclusion made earlier.

Fig 6.1 is an election micrograph taken by Dr. M.H. Lewis from a specimen prepared by B.J. Wicks

FIG. 6.1

INCLINED (45°) GLIDE BAND IN Ti:I CONTAINING A COARSE DISPERSION OF SPINEL PRECIPITATES.

(200 k.v.)

6.5. Correlation of Hardening Mechanisms with the Observed Flow Stress Variations

In this section calculations are presented on the basis of the models discussed in this chapter using some of the experimental observations of Chapter 5. The discussion is centred on diagrams in Fig. 6.2. The flow stress increments in these diagrams have been attributed to (a) $\Delta\tau_F$, the flow stress increment at 20°C caused by impurity-vacancy pair obstacles (b) $\Delta\tau_V$, the contribution of cation-anion vacancy pairs (c) $\Delta\tau_L$, the effect of dislocation loops formed by vacancy condensation (d) $\Delta\tau_O$, the increment in flow stress for an Orowan mechanism (e) $\Delta\tau_i$, an estimate of the contribution of interstitial oxygen. For each dopant, the flow stress increments or decrements are shown with respect to the as-grown value, except for Fe : 2.

(a) Fe : 1.

The effect of obstacles in the form of impurity vacancy pairs may be calculated from the concentration variation of centres of this type observed by E.P.R. From the determination of the absolute concentration of trivalent ions in the as-grown state, the concentration of associated ions is found to be 15-20 p.p.m. During ageing aggregation of impurities and vacancies occurs up to a maximum of 80 p.p.m. In order to evaluate the flow stress increment $\Delta\tau_F$ at room temperature, using equation 6.4. reasonable values for the parameters $\Delta\varepsilon$ and α are taken to be $\Delta\varepsilon = 0.45$ and $\alpha = 10$ (6.8.a.) The contribution of impurity - vacancy and anion-cation vacancy pairs in the other systems is also computed using these

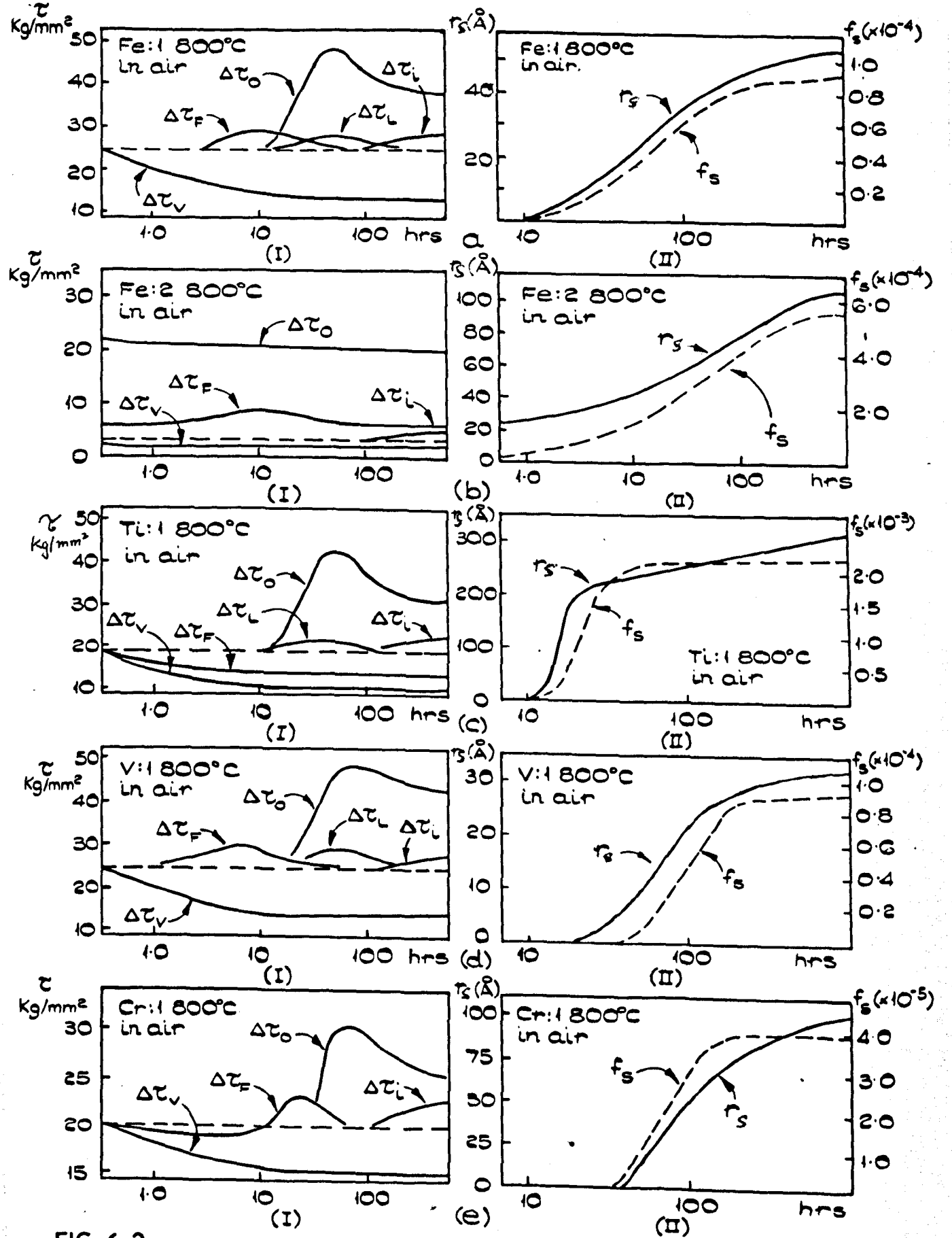

FIG. 6.2

ESTIMATES OF FLOW STRESS CONTRIBUTIONS IN MgO AT 800°C.

values. For Fe : 1, the maximum value of $\Delta\tau_F$ so obtained is τ_F 7.5 kg/mm^2.

For aged crystals direct evidence has been presented for facancy clustering, from which an estimate of the contribution of vacancy pairs, represented by $\Delta\tau_V$ is possible. In order that perfect stacking be maintained on {110} planes the observed dislocation loops must contain equal numbers of anion and cation vacancies lying in the loop plane in two layers. From the integrated areas of these loops a maximum concentration of 100 p.p.m. of vacancies of each sign is detected. On the assumption that the majority of the vacancies are associated as pairs or small clusters, a room temperature flow stress of $\Delta\tau_V$ = 12·0 kg/mm^2 is calculated. An estimate of the increase in hardness due to vacancy loops ($\Delta\tau_L$) may also be made from direct observation of loop densities using the equations given in 6.3. At longer times in air, (100 hours), diffusion of interstitial oxygen is expected, giving rise to a flow stress increment $\Delta\tau_i$ which is difficult to evaluate quantitatively, but which is given a representative value in all the systems of 2 - 3 kg/mm^2.

The quantitative features of the ageing behaviour of Fe ; 1 at 800°C can be seen to be consistent with the calculations made on the basis of these models, espcecially in the early stages. The further use of these calculations is in evaluating the contribution of Orowan hardening at the low temperature ageing peak.

A process is indicated by the E.P.R. results in 5.2 for spinel precipitate nucleation of the form:-

$Fe^{2+} \rightarrow Fe^{3+} \rightarrow Fe^{3+}$ - vacancy pairs → spinel precipitate, from which the total volume fraction of spinel precipitate can be calculated

by measuring the difference between the maximum concentration of associated Fe^{3+} ions and the final value.

This represents the absolute volume fraction of spinel precipitates. The variation of volume fraction (f_s) with time is monitored by the variation in the E.P.R. line due to Fe^{3+} ions in precipitate form, which is observed to be constant after 100 hours. The flow stress variation $\Delta\tau_o$ is taken to be the observed flow stress variation remaining after the contributions mentioned earlier have been subtracted, and hence the variation of mean particle radius with ageing time (r_s) may be calculated for different annealing stages, using equations in 6.4, The purpose of this calculation is to compare the mean particle radius r_y in the ageing sequence with the observed microstructure. In this case no precipitate dispersion is visible throughout the ageing sequence shown, and this is consistent with the calculated radii, which even after long anneals does not exceed 45 Å, and the minimum resolvable particle radius calculated in 6.6.

(b) Fe : 2.

On the assumption that the flow stress of as-grown crystals of Fe : 2 is determined by a "pure" value of 3 kg/mm^2, and a contribution from impurity-vacancy pairs estimated from the observed E.P.R. concentration to be 3 kg/mm^2, the remaining 19 kg/mm^2 may be ascribed to a precipitate dispersion. The volume fractions of spinel precipitate (f_s) in Fig.6.1 (b) is derived directly from a comparison of the spinel precipitate resonances in Fe : 1 over the 800°C annealing range, to give an initial average particle radius r_i as shown. From the development of the E.P.R. spectrum of the concentration of associated Fe^{3+} ions in Fe : 2, the contribution

to the flow stress τ_F may be calculated as presented. The contribution τ_V is expected to be small, since dislocation loop nucleation is not observed. From the experimentally observed flow stress variation at 800°C, and the observed increase in the Fe^{3+} precipitate resonance, values for the mean radius of the precipitate dispersion may be calculated as before. In this case particles are observed after 50-60 hours at 800°C, which is consistent with these calculations, and the visibility limits presented in 6.6. The volume fraction observed experimentally after this time is in agreement with the value obtained using the E.P.R. precipitate resonance.

(c) Ti : 1.

The results presented in 5.3. suggest that in the as-grown state, oxidation of Ti^{3+} ions to the tetravalent state is virtually complete. As precipitation proceeds, therefore, the concentration of Ti^{4+} ions and impurity-vacancy pairs in solid solution is progressively lowered, leading to a decline in the hardening due to τ_F, as shown. The concentration of associated ions assumed in this calculation is taken to be 5% of the total impurity concentration, in agreement with the observations on the other systems. The vacancy pair contribution $\Delta\tau_V$ can also be calculated in terms of the observed integrated loop area in aged specimens to be $\tau_V = 10\ kg/mm^2$.

For this system a direct correlation of the precipitation hardening behaviour is possible on an Orowan mechanism in terms of the observed precipitate radii r_s and volume fraction f_s, given in Fig.6.2.(c) (ii). The magnitude and form of the curve for τ_o is in good agreement with the experimental values, when other contributions to the flow stress are subtracted.

(d) V : 1

The V^{3+} optical absorption band has been calibrated in terms of the E.P.R. absolute concentration determination as 600 p.p.m. in the as-grown state. From the variation of this curve with time, 10% of the total V^{3+} concentration is interpreted to be incorporated in a precipitate lattice, assuming that the oxidation reaction to the trivalent state is an intermediate stage in the nucleation of the spinel lattice. In this case, although the calculated curve in Fig. 6.2.(d) (ii) is likely to be less precise in form than in the case of Fe : 1, the calculated particle radii on the basis of the observed Orowan increment at peak hardness is consistent with the absence of a visible precipitate dispersion, as indicated by the calculations for particle visibility in 6.6. The flow stress curves for $\Delta\tau_F$, $\Delta\tau_V$ and $\Delta\tau_i$ (the contribution from the interstitial oxygen - V^{4+} centre), from which the Orowan estimate is made, are derived as for Fe : 1, on the basis of the observed E.P.R. optical absorption and microstructural changes over the annealing range.

(e) Cr : 1

The variation with time of the intensity of the Cr^{3+} - impurity centre observed by E.P.R. is similar to the case of Fe : 1 and the contributions are calculated in the same way. The absolute concentrations of ions in the trivalent state is determined as 400 p.p.m. and the concentration of associated ions in as-grown crystals is found to be 20 p.p.m. This concentration is increased on ageing as clusters form prior to precipitation, and returns to a similar value after longer ageing times, consistent with development of the low temperature ageing peak. From the observed concentration of asymmetric centres the contribu-

tion $\Delta\tau_F$ may be calculated, and a curve $\Delta\tau_0$, corresponding to the experimentally determined flow stress can be drawn. For the estimated volume fraction of precipitate with ageing time, the resulting mean particle radius is of a size consistent with the visibility calculations of 6.6. and the microstructural observations. The interstitial contribution $\Delta\tau_i$ after long ageing times is not expected to measurably affect the value of $\Delta\tau_0$.

The assumption of non-deforming particles thus allows an interpretation of the form of the flow stress curves which are consistent with experimental observations. Interactions of the Fleischer type are found to modify the flow stress curves only after short ageing times.

No calculations on the basis of the flow stress models presented are made for high temperature anneals, but a qualitative discussion in terms of these models may be given. For ageing temperature greater than 1,200°C, precipitation will not occur for the iron and chromium doped crystals, since for the compositions considered this is above the equilibrium phase boundary. For both Ti : 1 and V : 1 precipitation is observed at both 1,200°C and 1,500°C on a scale which, for V : 1 produces a negligible contribution to hardening on an Orowan mechanism, and for Ti : 1 results in a small hardening contribution. Variations in the scale of precipitate dispersion with temperature between different systems is discussed in 6.7. Since the marked hardening at high temperatures is common to all systems, it is clearly not associated with precipitation,

but the spectroscopic observations indicate that a centre associated with interstitial oxygen is responsible for this behaviour. A quantitative estimate of the flow stress for a distribution of sites of this type is not possible, but a Fleischer-type of interaction between dislocations and the asymmetric strain field at the centre is expected.

The rapid reductions in flow stress observed in reducing atmospheres is due to valence changes in the impurity ion caused by reactions of the type:-

$$2\ Fe^{3+} + [V_{Mg}] + O^{2-} \rightleftharpoons 2\ Fe^{2+} + \tfrac{1}{2}O_2$$

On reageing reduced crystals in air at temperatures below the solid solution phase boundary, (e.g. Fe : 2 at 800°C and Ti : 1, V : 1 at 1,200°C) the flow stress recovery is explicable in terms of a precipitation hardening mechanism. For reageing temperatures above the equilibrium phase boundary (e.g. Fe : 2 at 1,200°C), recovery is promoted by the formation of impurity-vacancy pairs and centres involving interstitial oxygen ions.

6.6. Visibility Limits for Spinel Particles.

The flow stress calculations, made on the basis of various dispersed defect models, indicate that the most important contribution to the flow stress at low temperatures is that of precipitation hardening. In a number of cases the precipitate dispersion is invisible at the flow stress maximum; nevertheless there is strong evidence, in the case of Fe : 1, for the existence of a dispersion. Calculations to establish the limiting radii for visibility of various spinel particles are particularly important as a means of substantiating the above conclusions.

A discussion of the two contrast effects by which spinel particles are expected to be detectable by electron microscopy, i.e. coherency strain contrast and structure factor contrast, has been given in 3.5.

The minimum resolvable radii of the spinel precipitates under consideration are listed in table 6.3. for assumed spherical particles of radius r_o imaged by coherency strain contrast in different reflections ($\underline{g}$). The lattice mismatch parameter δ in each case is calculated from the free lattice spacings of stoichiometric crystals.

Diffracting Vector $\underline{g}$	MgO extinction distance (Å)	r_o (Å)				
		$MgFe_2O_4$	Mg_2TiO_4	$MgCr_2O_4$	Mg_2VO_4	MgV_2O_4
(200)	461	60	140	46	80	Invisible
(220)	662	56	100	43	81	129
(400)	1033	58	103	45	76	147
(420)	1201	59	120	48	81	143

Table 6.3.

For two cases in which spherical precipitates are identifiable, i.e. Ti : 1 and Fe : 2, the validity of this misfit estimate can be tested by measuring the image width of the strain fields observed by diffraction contrast for a known diffracting vector. For titanium spinel, the mean value of δ, calculated using the analysis of Ashby and Brown[48], is found to be $1.3 \pm 0.3 \times 10^{-3}$ using a (220) reflection, and $1.7 \pm 0.3 \times 10^{-3}$ using a (240) reflection. This is in good agreement with the quoted value of the

misfit parameter for the inverse titanium spinel Mg_2TiO_4 of $\varepsilon = 1.6 \times 10^{-3}$, and confirms the spinel structure suggested by the phase diagram for this system. A similar analysis for coherent precipitates in Fe : 2 gives an estimated misfit parameter of $5.0 \times 10^{-3} \pm 0.3 \times 10^{-3}$ using a (220) reflection, consistent with the misfit parameter of $MgFe_2O_4$ of $\varepsilon = 5.2 \times 10^{-3}$.

A comparison between the visibility limits quoted in Table 6.3 and the corresponding radii predicted in Fig. 6. 2 confirms that for Fe : 1 and V : 1 precipitates of resolvable dimensions need not be present in order to explain the 800°C ageing behaviour. In the other systems i.e. Cr : 1, Ti : 1 and Fe : 2, resolvable precipitates are predicted for (1) $MgCr_2O_4$ after 90 - 110 hours, (2) Mg_2TiO_4 after 15 - 20 hours, (3) $MgFe_2O_4$ after 50 - 60 hours. These figures are in good agreement with the earliest ageing times for which a spinel precipitate dispersion is resolvable as given in Chapter 5.

Precipitates may also be detected by differences in structure factor of the matrix and spinel precipitate. A discussion of the way in which this factor can affect the transmitted intensity and a criterion for particle visibility, is given in 3.5. The results of calculations based on this treatment are therefore simply presented in Table 6.4, for both inverse and normal spinels as (a) the appropriate extinction distance for two different reflections in each spinel, (b) the particle radius $\Delta t/_2$ corresponding to a detectable variation in the background intensity, assumed to be 10%.

Spinel		Spinel Reflection	
		(400)	(440)
$MgFe_2O_4$	ξ_g (Å)	940	620
	$\Delta t/2$	7	113
Mg_2TiO_4	ξ_g (Å)	1550	850
	$\Delta t/2$	5	24
$MgCr_2O_4$	ξ_g (Å)	880	610
	$\Delta t/2$	7	61
Mg_2VO_4	ξ_g (Å)	1500	840
	$\Delta t/2$	5	25
MgV_2O_4	ξ_g (Å)	945	640
	$\Delta t/2$	7	160

Table 6.4.

It can be seen from this table that for high order reflections the limiting radius increases rapidly, and that best visibility is obtainable with a (200) MgO reciprocal lattice vector.

Detection of small particles is most readily accomplished at the edge of an electron microscope specimen, where the transmitted intensity is a rapidly varying function of thickness. The positions of maximum visibility under these conditions occur at values of $\frac{h}{\xi_g} = 1/4, 3/4, 5/4$ ---------

where h is the thickness of the section, i.e. in the regions of thickness fringes. For chemically polished sections, however, in the regions near the extreme edge where structure factor contrast is applicable, the surface

is inevitably irregular on a microscopic scale. The contrast from an etch pit, obtained by putting $\xi^s_g = \infty$, is of the same nature as the spinel precipitate contrast, and shows an identical transition from black - to- white contrast on either side of a thickness fringe. Visibility of precipitates by structure factor contrast is therefore obscured by the more prominent surface contrast; the visibility criterion adopted in Table 6.4 is therefore unrealistic.

In view of the importance of coherency strains in the detection of small spinel precipitates, it is necessary to consider the critical particle dimensions at which coherency is lost at the interface between the matrix and each spinel precipitate. This interface is initially fully coherent with respect to the anion lattice, and any mismatch of lattice parameters is accommodated completely as lattice strain. As the particle grows, the interfacial area increases up to a point at which the misfit can no longer be constrained elastically, and the lattice strain may then be relieved by the introduction of structural dislocations at the boundary.

This can occur by a prismatic loop punching mechanism if the shear stress on the slip planes immediately outside the particle becomes greater than the theoretical shear stress of the matrix. For a spherical particle in a state of pure dilation, the shear stress on a slip plane (p_s) has been computed to be [96],

$$p_s = 2/3\ \mu\ \varepsilon$$

The magnitudes of the misfit parameters for the spinels considered are insufficient to satisfy the condition for loop punching, and it is

concluded that the nucleation of an interfacial dislocation is possible only by the collapse of a vacancy cluster as a dislocation loop in the vicinity of a particle, and the subsequent absorption of this loop at the interface. The critical particle radius at which this loop is stabilised is determined by an equilibrium between the line tension effect of the loop, causing the loop to shrink, and an interaction with the stress field of the precipitate, tending to expand the loop. Two critical radii have been derived from this condition by Brown et al.[97]. The first, obtained by equating the two forces on the dislocation loop is given by:-

$$r_{crit} = \frac{b}{16\pi\varepsilon(1-\nu)}\left[\ln\left(\frac{8r_{crit}}{b}\right) + \frac{3-2\nu}{4(1-\nu)}\right] \quad - G.11$$

A second critical radius at which the coherent state becomes metastable with respect to the incoherent state is given by equating the energy terms:-

$$r^* = \frac{b}{8\pi\varepsilon(1-\nu)}\left[\ln\left(\frac{8r^*}{b}\right) - 1 + \frac{3-2}{4(1-\nu)}\right] \quad - G.12$$

Table 6.4a gives the critical radii for coherency loss for the relevant spinel precipitates, in terms of these two radii

Spinel	r_{crit} Å	r^* Å
$MgFe_2O_4$	113	216
Mg_2TiO_4	450	850
$MgCr_2O_4$	75	144
Mg_2VO_4	234	445
MgV_2O_4	725	1430

Table 6.4a

It can be seen that detection of small precipitate particles by coherency strain contrast is possible for the limiting radii calculated earlier up to the critical radii presented here.

6.7. Nucleation of Spinel Precipitates.

Electron microscope and flow stress observations presented in Chapter 5 suggest that the scale of dispersion of precipitates produced by various heat treatments is largely controlled by the concentration and distribution of vacancies. A noticeable feature observed in all specimens containing a precipitate dispersion is a wide precipitate-free-zone at dislocation sub-grain-boundaries, shown typically in Fig. 6. 3, for a region of a titanium doped Ti: 1 crystal after an ageing treatment at 800°C for 20 hours. The absence of substantial precipitation on the boundary indicates that impurity depletion is not responsible for the absence of precipitation adjacent to the boundary, and it is proposed that vacancy absorption by the dislocations forming the boundary during cooling from the melt results in an insufficient supersaturation for nucleation of spinel precipitates during the subsequent ageing treatment. In the micrograph of Fig.6.3 most of the dislocations constituting the boundary are in screw orientations and are observed to climb into helical configurations as a result of vacancy absorption. The long screw dislocation attached to the boundary has also climbed into a helical form, and is itself in a region in which precipitation is absent. Further from the boundary a precipitate dispersion can be seen to be associated with a vacancy supersaturation sufficient for loop nucleation (5.3.d) The vacancy profile at the sub-boundary vacancy sink is shown schematically in Fig. 6.4.(a). It can be seen from this diagram that no precipitates are expected in the region adjacent to the boundary up to a

Fig 6.3 is an electron micrograph taken by D. M.H Lewis from a specimen prepared by R.J.W.Hay.

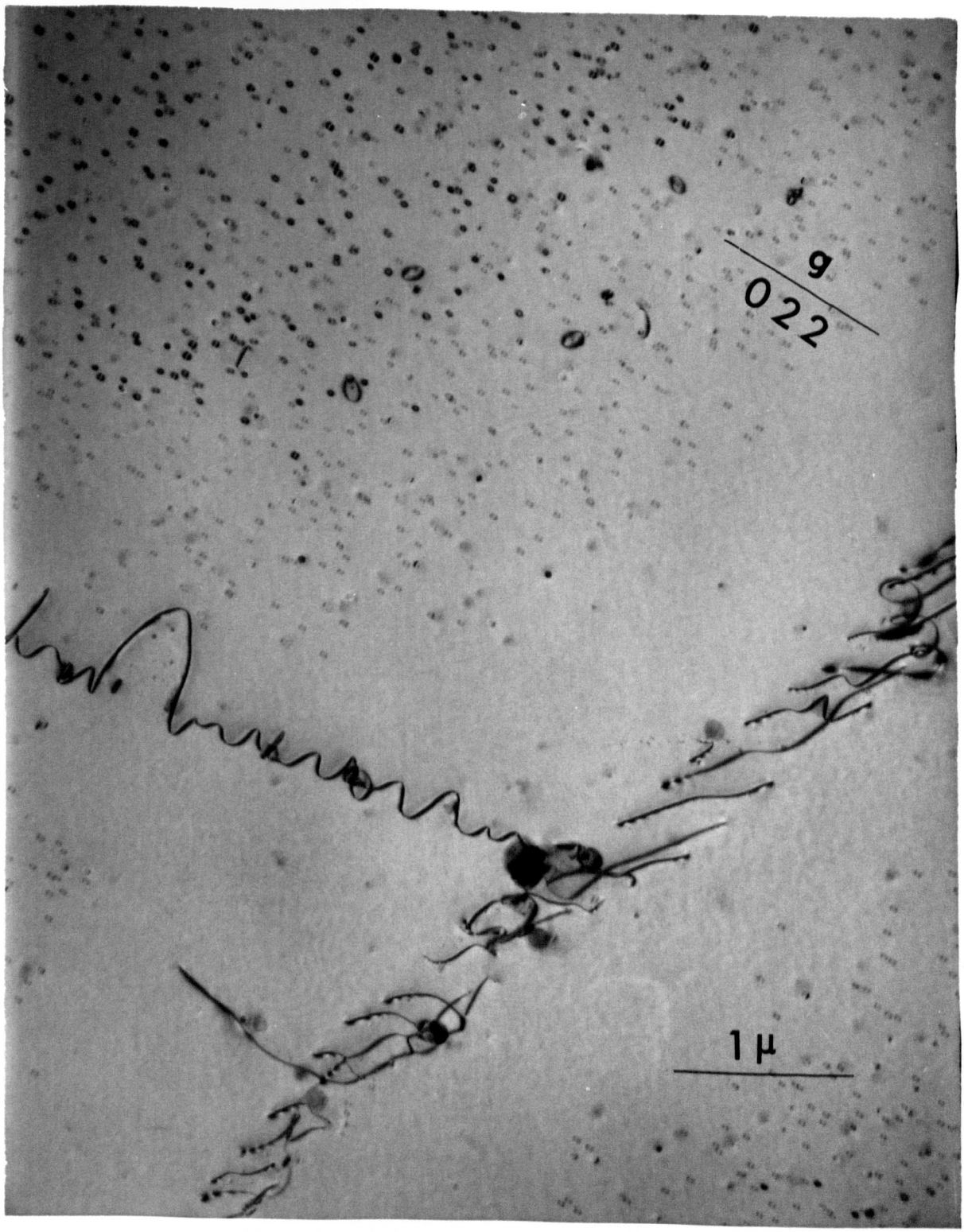

FIG. 6. 3

Ti:I AGED FOR 20 HOURS AT 800°C IN AIR, SHOWING A PRECIPITATE DENUDED ZONE AT A DISLOCATION SUB-GRAIN-BOUNDARY.

(1000 k.v.)

critical vacancy concentration C^{T}_{crit}, but nucleation can occur quite readily within the sub-grains.

This suggestion of vacancy aided nucleation is similar to that proposed for precipitation hardening in aluminium based alloys. In particular, a theory has been developed on the basis of observations in Al - Zn - Mg in which it was first suggested that the effect of vacancies on the nucleation of precipitates could occur in two distinct ways[98]. An explanation was first attempted in terms of a thermodynamic model, in which the existence of vacancies in association with pre-precipitate clusters has the effect of increasing the effective supersaturation, thereby decreasing the critical nucleus size, for a particular ageing temperature. The effect of a vacancy supersaturation on the free energy changes accompanying nucleation is illustrated further in Fig. 6.4.(b). Later work on this system[99] suggested that the formation of a precipitate free zone at grain boundaries during an ageing treatment was caused by a reduction in the total diffusive flux near the boundary due to vacancy depletion. This had the effect of lowering the size of nuclei formed either during cooling after a solution treatment or at a lower holding temperature, such that at the ageing temperature the nuclei were of a sub-critical size and hence redissolved.

Precipitation of spinel may be readily explained on the basis of either model. On a kinetic nucleation model, the existence of a supersaturation of both cation and anion vacancies is expected to aid the transport of ions to nucleation sites as suggested. The earlier thermodynamic explanation is also relevant to a supersaturation of cation vacancies, since for all

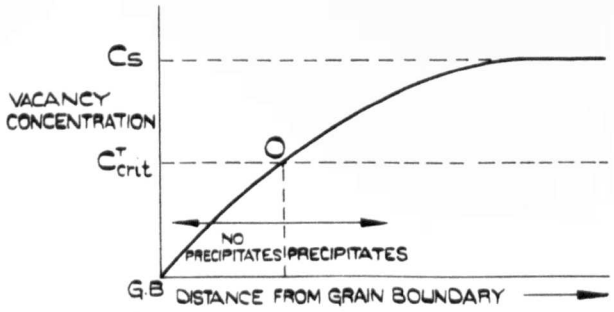

A SCHEMATIC ILLUSTRATION OF THE VACANCY CONCENTRATION PROFILE FORMED ON QUENCHING. C^s IS THE EQUILIBRIUM VACANCY CONCENTRATION AT A SOLUTION TEMPERATURE T_s AND C^T_{crit} IS THE CRITICAL VACANCY CONCENTRATION REQUIRED TO NUCLEATE PRECIPITATES AT AN AGEING TEMPERATURE T.

FIG. 6.4(a)

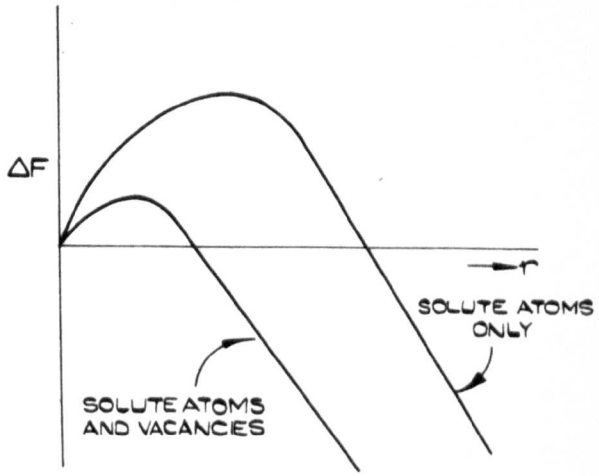

POSSIBLE CURVES FOR THE FREE ENERGY CHANGE (ΔF) AGAINST NUCLEUS SIZE (r) AT AN AGEING TEMPERATURE, T, FOR (I) CLUSTERS OF SOLUTE ATOMS ONLY, (II) CLUSTERS OF SOLUTE ATOMS AND VACANCIES. THE CRITICAL NUCLEUS SIZE AND THE ACTIVATION ENERGY FOR NUCLEATION IS REDUCED IN THE LATTER CASE.

FIG. 6.4(b)

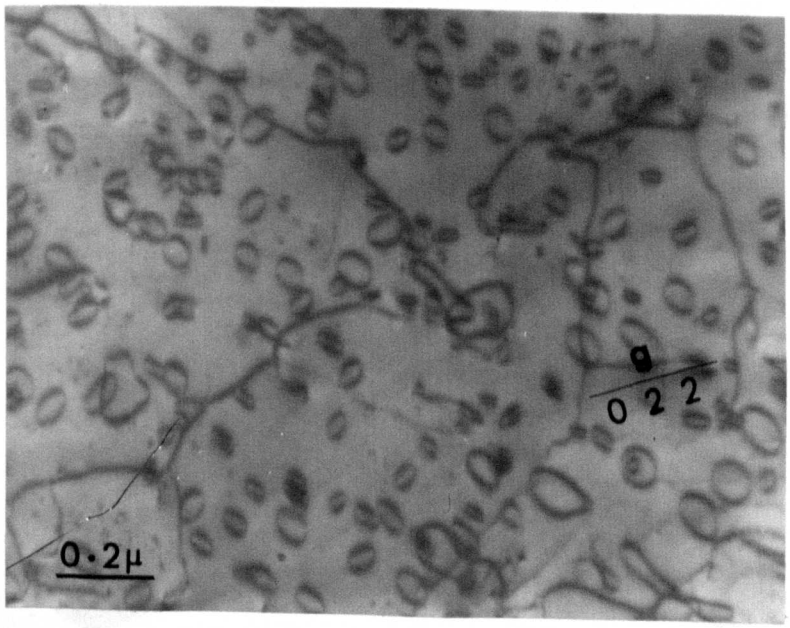

FIG. 6.5

PRISMATIC LOOPS FORMED IN CRYSTAL Fe:I AFTER PULSE HEATING IN THE ELECTRON BEAM.

the spinel structures considered, only half the octahedral sites in the anion sub-lattice are occupied, and cation vacancies may therefore be regarded as a chemical constituent of the spinel phase. It is proposed that the nuclei for all the spinel precipitates are formed from impurity-cation vacancy pairs, and that growth proceeds by the aggregation of further close paired impurity ions and vacancies. The evidence for this suggestion is particularly clear in the case of Fe : 1, where an unambiguous interpretation of the E.P.R. results is possible in terms of a pre-precipitate cluster of this form.

The nature of the dispersion formed at different temperatures and after different thermal histories can be explained by an application of the models described to spinel precipitates. An important factor which must be considered is the arbitrary cooling rate experienced by different crystal melts, which affects both the concentration and distribution of vacancies.

For ageing temperatures above 1000°C in air the iron and chromium impurities are all in solid solution, above the equilibrium phase boundary. The systems V : 1 and Ti : 1 are below the phase boundary at this temperature, and a coarse dispersion is produced, often associated with dislocation loops. The observed difficulty of nucleation is explicable in terms of the low impurity and vacancy supersaturation, which gives rise to a low nucleation rate at high ageing temperatures. For Ti : 1 the supersaturation is sufficient to form a dispersion which produces a small hardening effect at 1,200°C, but for V : 1 precipitation is observed to be almost completely associated with dislocation loops, giving rise to a negligible precipitation hardening.

Differences in the low temperature ageing behaviour of Fe : 2, Fe : 1 and Ti : 1 are especially noticeable. In crystals of Fe : 2 nucleation occurs during melt cooling when the temperature of the melt falls below the equilibrium phase boundary, and nuclei continue to form throughout the remainder of the cooling period. In as-grown crystals therefore a size distribution of nuclei exists which is determined principally by the cooling rate. On re-ageing at 800°C all nuclei below the critical size for this temperature re-dissolve, while a stable dispersion of nuclei above the critical size persists and subsequently grows. The total volume fraction of precipitate is insufficient for detection of individual particles except after extended anneals. In the melt Fe : 1 the impurity supersaturation is low, and fewer nuclei are formed during cooling. A high rate of nucleation is produced by ageing at 800°C in the existing vacancy supersaturation after an initial incubation period, during which precipitate nuclei are formed by impurity-vacancy aggregations. A similar thermal history is attributed to the vanadium and chromium doped melts. For Ti : 1 the impurity supersaturation and cooling rate is such that nuclei are present in the as-grown crystal. On ageing at 800°C a much higher volume fraction of precipitate is formed than in other systems, giving rise to an observable dispersion after short ageing times.

The important role of vacancies in controlling both the nucleation and growth rate of spinel particles is also manifest in the re-ageing behaviour of reduced crystals. During the reducing treatment the vacancy concentration is lowered as anion-cation vacancy pairs cluster to form dislocation loops, diffuse to the free surface, or are absorbed at low angle dislocation boundaries. The precipitate distribution formed on

re-ageing in air is typical therefore of a much lower vacancy supersaturation, determined by the re-oxidation of the divalent impurity ions. For Fe : 2 this gives rise to a peak flow stress at 800°C which is much less than would be expected from the ageing behaviour of as-grown crystals.

There is a good evidence for a non-equilibrium concentration of vacancies in as-grown crystals from direct observations of electron microscope specimens pulse heated in the electron beam by removing the condenser aperture. The precise nature of the thermal cycle involved is not known, but in some cases it is sufficient to cause coalescence of existing anion-cation vacancy pairs at a rate much higher than that corresponding to a normal ageing treatment at 800°C - 1500°C. The high density of prismatic loops produced in this way is shown in Fig. 6.5. for on Fe : 1 specimen. Under similar conditions loops have also been produced in V : 1 crystals. Further evidence for the existence of a vacancy supersaturation in the as-grown state is given in 6.8.c.

6.8. Investigations of the form of Dispersed Obstacles other than Precipitates.

Discussion of the hardening mechanisms so far has centred mainly on precipitation hardening, but in the course of the correlation, reference has necessarily been made to other contributions to the hardening which are believed to be important in as-grown crystals (with the exception of Fe : 2). The nature of obstacles suggested previously as giving rise to the flow stress of crystals in the as-grown condition is analysed here by means of observations on the temperature dependence of the flow stress. Further evidence of the nature of these obstacles is presented finally in an investigation of the interaction of these pre-existing defects with defects produced by neutron irradiation.

The results of the temperature dependence experiments are applied to a Fleischer model for the interaction potential (6.1.b), which is thought to be applicable in view of the anisotropic nature of obstacles in the unaged state. The temperature variation of the flow stress due to these obstacles may be conveniently discussed in terms of two temperature intervals (1) 0 - 400°K, in which a strong temperature dependence is observed (2) 400 - 1800°K, in which the temperature sensitivity is lost.

6.8.a. Low Temperature Flow Stress.

Variations

The temperature dependence of the flow stress measured over the low temperature range for crystals Cr : 1, Fe : 1, Ti : 1, V : 1 in the as-grown condition is shown in Fig. 6.6. It can be seen that the data from these low temperature tests show a very good fit to a relationship of the form $\tau^{\frac{1}{2}} \propto T^{1/2}$ (where T is the absolute temperature) at sufficiently low temperatures, as predicted by the Fleischer model for asymmetric distortions.

In an absence of a knowledge of the strain tensor of the defect centres responsible for the strong temperature dependence in MgO, it is assumed that the treatment given by Fleischer for impurity-vacancy pairs as $\langle 110 \rangle$ distortions is applicable. The flow stress increment $\Delta\tau_f$ for asymmetric distortions in this theory may be written as $\Delta\tau_f = \tau - \tau_s$, where τ is the flow stress measured at a particular temperature and τ_s is the friction stress for MgO containing a vanishingly small impurity concentration. A limiting value for τ_s is taken to be 5 kg/mm^2.

The parameters defined previously in 6.1.b are listed for Cr : 1 and Fe : 1 in Table 6.5. These parameters have been calculated from the

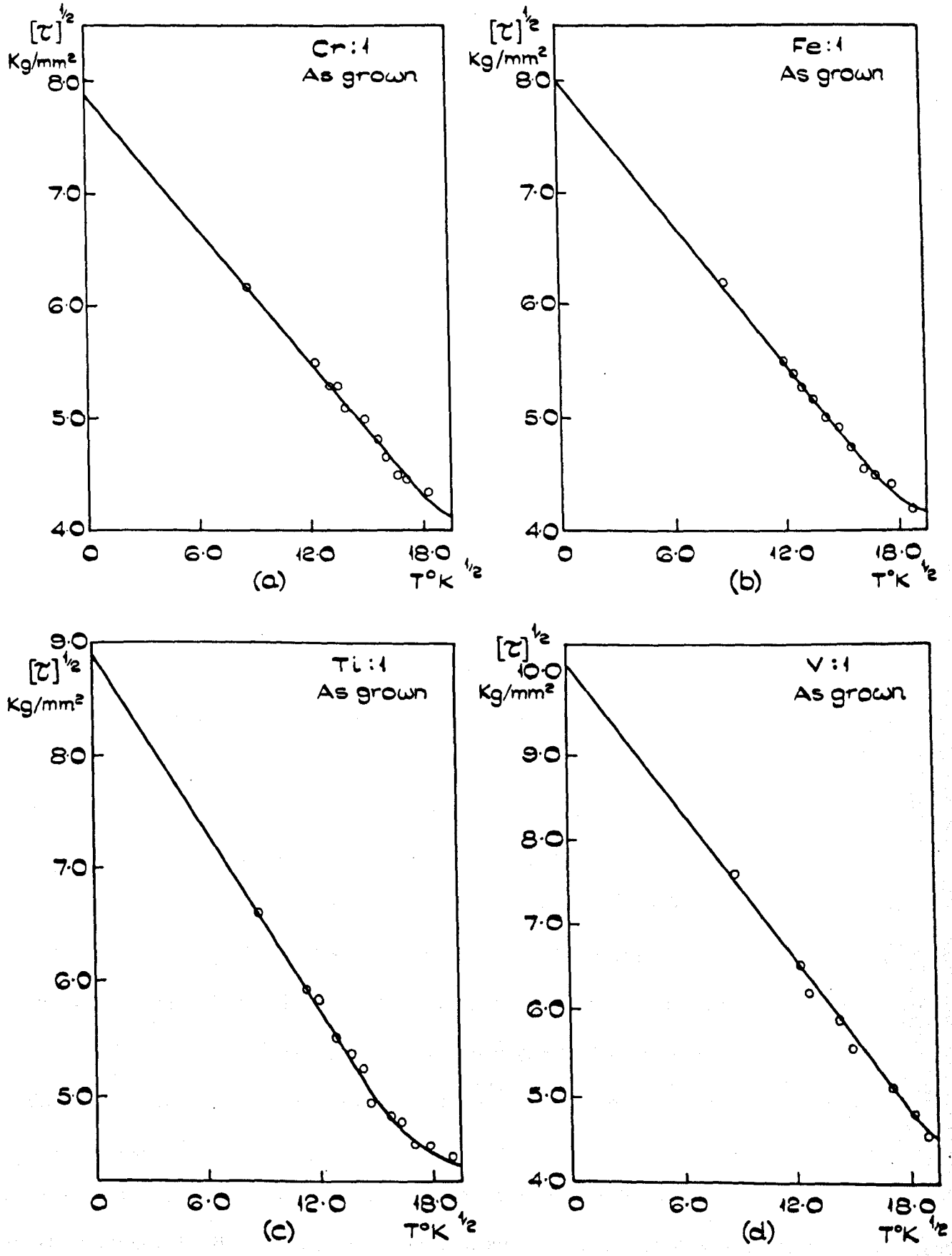

FIG. 6.6

TEMPERATURE VARIATION OF THE FLOW STRESS FOR Cr:1, Fe:1, Ti:1, V:1 BELOW ROOM TEMPERATURE.

experimental data by extrapolating the observed flow stress to absolute zero, and by using the experimentally determined concentration of impurity-vacancy pairs.

Systems	concentration of pairs (p.p.m)	$\Delta\tau_M$ kg/mm^2	$\Delta\varepsilon$	U_o (e.v)
Cr : 1	20	57	2.6	9.0
Fe : 1	20	59	2.9	9.3

Table 6.5.

The values of $\Delta\varepsilon$ tabulated in column four represent the difference in longitudinal and transverse strains at the defect, are seen to be completely implausible (greater than unity) compared to the reasonable values obtained for similar dispersed centres in other systems, e.g. $\Delta\varepsilon = 0.55$ for interstitials in copper[100], $\Delta\varepsilon = 0.41$ for carbon in iron[101], and $\Delta\varepsilon = 0.44$ for magnesium in LiF[33]. The interaction energy between a dislocation and the defects present, U_o, has also been estimated from the activation energy U in the absence of an applied stress, i.e. by putting $\Delta\tau_F = 0$ in equation 6.2. The elastic interaction energy between an impurity ion-cation vacancy pair in a (n.n.) configuration has been computed for Ca^{2+} ions in NaCl to be 0.4 - 0.5 eV[102]. It can be seen that the values for similar defect centres are in complete disagreement with this value. The implication of these results is that additional undetected centres are present in MgO having similar symmetry to impurity-vacancy pairs. The concentration of these centres may be derived by assuming reasonable values for $\Delta\varepsilon$, and re-calculating the defect concentrations on the basis of

the temperature dependence. This is shown for the systems investigated in Table 6.6. for two extreme values of $\Delta\varepsilon$ (i.e. 0.3 and 0.7) between which the values for other asymmetric defects have been found to lie.

System	Total impurity concentration (p.p.m.)	$\Delta\gamma_M$ Kg/mm^2	Concentration of defects (p.p.m.) for $\Delta\varepsilon$ = 0.3 - 0.7
Cr : 1	600	57	630 - 120
Fe : 1	900	59	680 - 128
Ti : 1	1,000	74	1060 - 200
V : 1	1,500	97	1840 - 340

Table 6.6.

It follows that for the defect concentration shown, values for the interaction energy can be derived which are consistent with the reasonable values quoted previously. This agreement with other systems found by using this calculated concentration in the place of the impurity concentration, is logically explained by the existence of asymmetric centres other than impurity vacancy pairs in the as-grown state, and it is suggested that these are in the form of anion-cation vacancy pairs. It can be seen that the predicted concentration of vacancies shows a rough proportionality to the total impurity concentration for the systems considered. This observation is not thought to be entirely fortuitous, since a substantial binding energy exists, not only betwen impurities and vacancies, but also between vacancies of opposite sign.

It is instructive to consider analyses of this type with other models

for the force-distance curves which have been proposed for other types of defect. In Fig. 6.7 the data for Fe : 1 has been re-plotted on the basis of the temperature dependence predicted by other theories. Alloys in which the yield stress is determined by the force to cut pricipitates have been shown to give a good agreement with a parabolic force-distance relationship between dislocations and precipitate obstacles, equivalent to a flow stress-temperature function of the form $\tau \propto T^{2/3}$. The flow stress of NaCl : Mn^{2+} has been interpreted from this linearity to be determined by the cutting of clusters in the form of trimers[103], and the graph (a) shows a similar agreement for Fe : 1. The plots in (b) and (c) represent square-well and triangular interaction potentials respectively. The $\tau^{1/3} - T^{1/2}$ plot in (d) represents the predicted relationship on a Fleischer model when the Friedel relationship is included[104]. In terms of these axes the results show an even better fit to a linear function. It can be seen from these plots that there is a reasonable fit to all the forms of interaction potential used, which indicates that it is not possible to assign a particular model for the force-distance relationships to the defects from an analysis of this nature. The distortion at the defect site, measured from the temperature dependence, is assumed to be of the form given in the Fleischer model, but the particular asymmetry cannot be accurately obtained from these observations. These remarks are applicable to other systems, especially those of the NaCl structure, from which values for $\Delta\varepsilon$ have been obtained on the basis of linear $\tau^{\frac{1}{2}} - T^{1/2}$ plots.

6.8.b. High Temperature Variations

Fig. 6.8 shows the temperature dependence for the as-grown crystal P : 1, in the temperature range 0 - 1,500°C. The form of this curve is

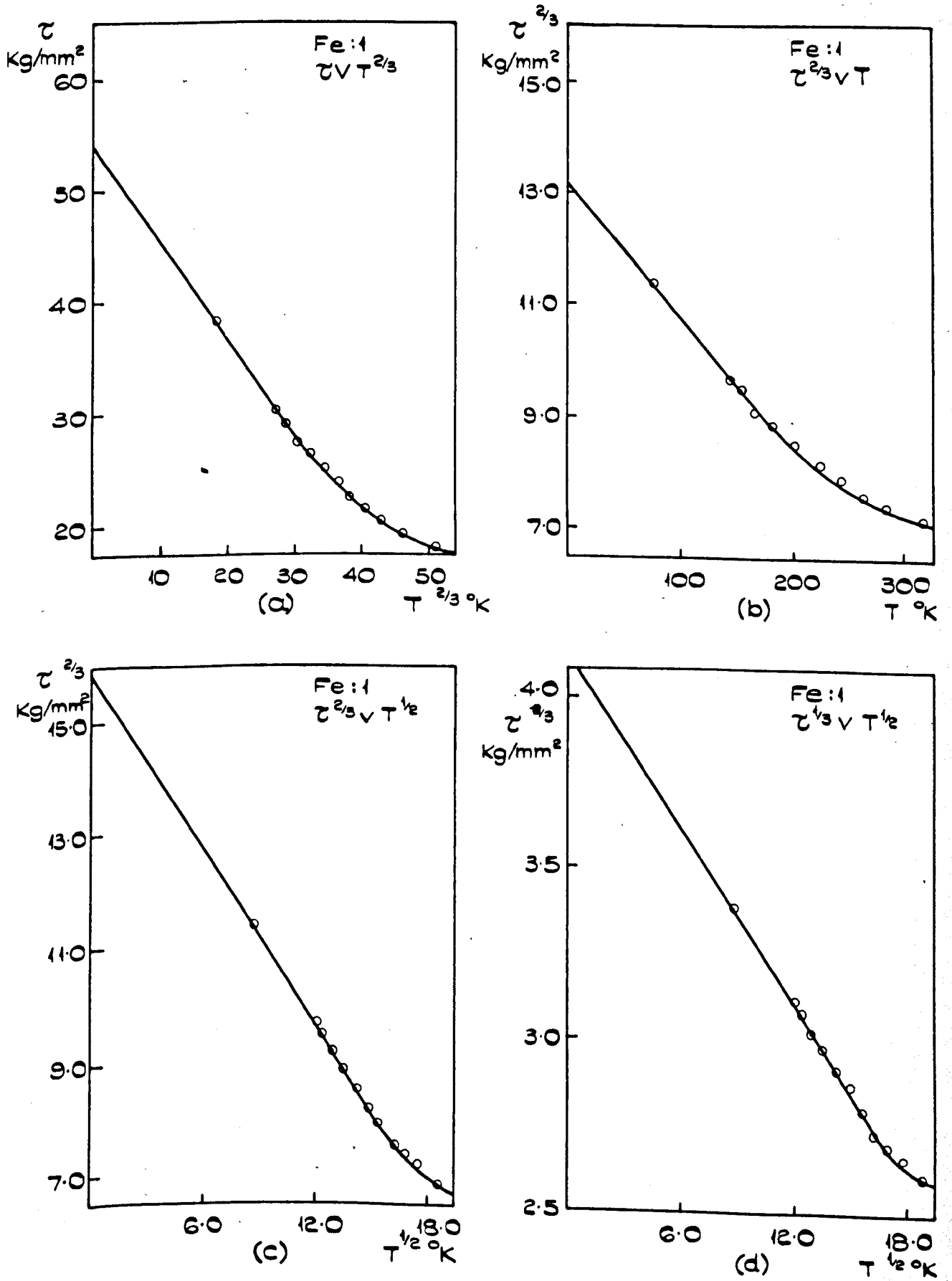

FIG. 6.7

TEMPERATURE - FLOW STRESS PLOTS FOR Fe:1 FOR VARIOUS RELATIONSHIPS.

similar to previously reported curves of undoped crystals[40][62][105]. The temperature dependence of as-grown crystals Ti : 1, V : 1 and Fe : 1 have also been investigated in this research, and the curves obtained for these crystals show an identical behaviour to undoped crystals. To avoid repetition a discussion is therefore given of characteristic features of the temperature dependence in the high temperature range with reference to the representative curve of P : 1 only.

From 0 - 350°C, the marked temperature dependence of the load required to deform the crystal in three-point-bending is controlled by the degree to which thermal fluctuations enable gliding dislocations to overcome the short range rigid energy barriers discussed earlier.

Above 350°C the curve exhibits a reversed temperature dependence up to a maximum value at 800°C, followed by a further softening in the higher temperature ranges. In the temperature range 350 - 1,000°C the shape of the stress-strain curve is characterised by repeated yield drops, shown in Fig.6.8 as representative stress-strain curves for particular temperatures. In the lower part of this range, the initial jerky flow disappears on continued deformation, but at the flow stress maximum, serrated yielding is visible up to large plastic strains. Yield drops were found to be reproducable by resprinkling the crystal with silicon carbide powder during test to introduce fresh dislocations.

The upper curve in Fig. 6.8. was determined by using the upper yield point load as a measure of flow stress. The lower, flatter, curve was determined by basing the flow stress on the lower yield point. The difference between these two curves is a measure of the contribution of dynamic impurity locking effects. Miles[106] has noticed that very large

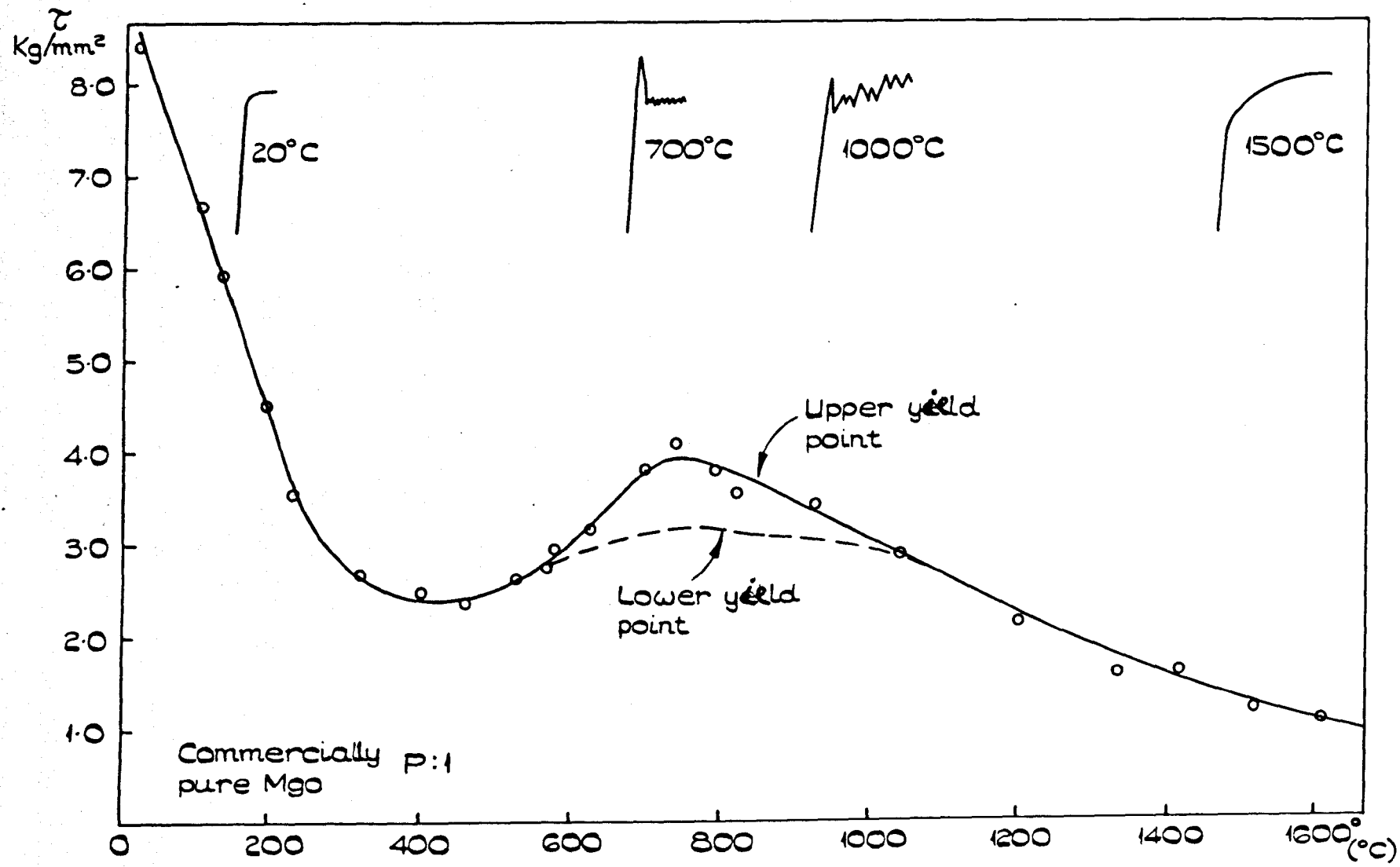

FIG. 6.8

TEMPERATURE DEPENDENCE OF THE FLOW STRESS OF CRYSTAL P:1.

errors are involved in a calculation of the stress levels in three-point-bending under these conditions, since an account must be taken of movement of the neutral axis during test, as fresh dislocations are continuously introduced at the compression face by contact with the loading knife edge.

The prominence of yield drops and a pronounced strain ageing behaviour in the region of this reverse temperature dependence is consistent with increased impurity diffusion rates, which imposes a drag on moving dislocations by the diffusion of impurities and impurity-vacancy pairs to the dislocation core. Yield drops then a rise from the thermally activated unpinning of dislocation line segments from their impurity environment.

A second type of interaction which must also be considered, is that involving the re-orientation of asymmetric centres in the elastic stress field of a gliding dislocation[34]. Although this type of interaction is capable of explaining the loss of temperature sensitivity, the strong dislocation locking effect implied by yield drops is not possible. It is likely, in view of the range of defect centres involved, that the observed behaviour is caused by the simultaneous operation of both mechanisms in this temperature range.

The recurrence of a further negative temperature dependence about 900°C is the result of increasing dislocation mobility on the primary gliding plane as impurity drag becomes less effective. The flow stress is also influenced by the increasing efficacity of climb and cross-glide on {100} and {11} planes to avoid the stress fields of obstacles[107].

6.8.c. Recovery of Fast Neutron Radiation Damage in Doped MgO Crystals.

The results presented earlier in this section may be interpreted in terms of the presence of a concentration of anion - cation vacancy pairs

approximately equal to the total impurity concentration. A study of the effect of these defects on the annealing behaviour of doped, neutron irradiated, crystals is used to support these conclusions.

Homogeneous samples cleaved from each of the melts V : 1, Ti : 1, and Fe : 1 were irradiated in two conditions - an as-grown state (A-G), and a reduced state (R) following anneals in a carbon monoxide atmosphere for 100 hours at 1,200°C. The specimens were then irradiated in the Harwell reactor B.E.P.O. at a temperature of less than 100°C (>1 MeV) to three doses - 9.2×10^{13}, 1.72×10^{16}, 9.3×10^{17} n.v.t. All subsequent heat treatments were carried out in air, and the flow stress measured from an evaluation of the dislocation flow around a microhardness indent. The results of these measurements showed a high degree of similarity for each impurity, and only the results appropriate to V : 1 are discussed here.

An estimate of the concentration of radiation induced defects is possible from a simple Kinchin-Pease model[108], in which the fraction (f) of ions displaced by a neutron flux ϕ is calculated from

$$f = \frac{\sigma_s \phi E_i \left[2 - \frac{Ei}{E_{max}}\right]}{4 E_d}$$

where E_d is the atomic displacement energy, assumed to be 25 eV, and Ei is the ionisation energy of a matrix ion. The required scattering cross-section σ_s is not known and the total cross-section σ_T is used instead. This calculation, evaluated for the highest dose level used, gives the number of displaced ions to be 3.9×10^{19} anion interstitials/cm^3 and 8.3×10^{19} interstitial cations/cm^3. Chanelling and focusing collisions[109], are expected to reduce the production of displaced ions at the primary knock-on site. Extensive work on pure neutron irradiate

crystals using E.P.R.,[110] cold neutron scattering[11] and macroscopic growth measurements[112], indicate that for the doses used this damage is predominantly in the form of isolated interstitials and vacancies with a small amount of clustering at the highest dose level. The total number of He and Ne gas atoms generated at the highest dose level, calculated from nuclear cross-section data, is only $3.0 \times 10^{14}/cm^3$ and is neglected in this investigation. For every system, the total impurity concentration is in excess of $10^{19}/cm^3$, and the existence of a similar vacancy pair concentration proposed earlier is expected to markedly influence both the accumulation of damage and the effect of post-irradiation annealing.

A surprisingly small increase in flow stress of as-irradiated crystals is shown for a given radiation dose, compared to previous measurements of pure MgO for which completely brittle behaviour is found for doses of $>10^{19}$ n.v.t.[113]. This is directly attributed to the role of the pre-existing vacancy concentration, suggested earlier, in absorbing damage during irradiation by direct interstitial vacancy annihilation processes. The results are also expected to be affected by an increased fracture stress, which would give a misleading indication of dislocation mobility around the indent. The effect of initial impurity valence state on the accumulation of damage with dose is shown in Fig. 6. 9. An empirical relationship can be formulated between the dose ϕ and flow stress γ as:-

$$\gamma = \gamma_o + S\phi^{\frac{1}{2}}$$

where γ_o is the unirradiated flow stress, and S is a constant related to the rate of accumulation of damage. It can be seen that this is markedly reduced for crystals irradiated in the as-grown state.

The recovery behaviour of the flow stress for each radiation dose is

shown in Fig. 6.10. A measure of the remanent radiation strengthening may be made most simply from a comparison of the difference in flow stress at the highest and lowest dose levels. It is apparent that recovery of as-grown crystals is effectively complete after 1 hour at 600°C, and the damage in reduced crystals is much more resistant to annealing.

No observable radiation damage was visible in the electron microscope for any of the crystals in the as-irradiated state, or for as-grown irradiated crystals after heat treatment. Short anneals at 800°C for reduced crystals resulted in the formation of a low density ($2.0 \times 10^{11}/cm^3$) of prismatic loops shown in Fig. 6.11. The sizes of the loops were insufficient to determine their sense by an accurate analysis, but the loops were assumed to be of interstitial type, in line with previous loop determinations in irradiated crystals[114].

It is generally accepted that irradiation hardening in the alkali halides is due mainly to interstitials[115]. If only single interstitials are considered for the doses investigated, the linearity of a $\gamma - \phi^{\frac{1}{2}}$ plot then immediately follows from an assumption that the hardening is proportional to the square root of the interstitial concentration. The dose dependence and observed annealing behaviour may be explained in terms of the vacancy content in each state. For as-grown crystals both anion and cation vacancies are present. Estimates of the vacancy concentration from the integrated areas of loops observed in unirradiated annealed crystals give values of 10^{18} vacancies/cm^3 of each kind and the total concentration is expected to be much greater than this. Recovery of

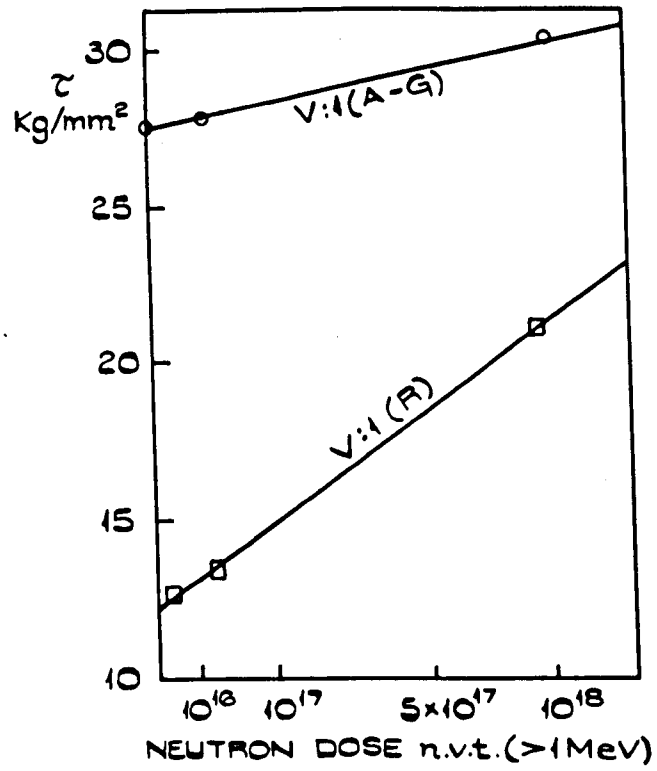

FIG. 6.9

VARIATION OF THE FLOW STRESS OF IRRADIATED V:I WITH NEUTRON DOSE.

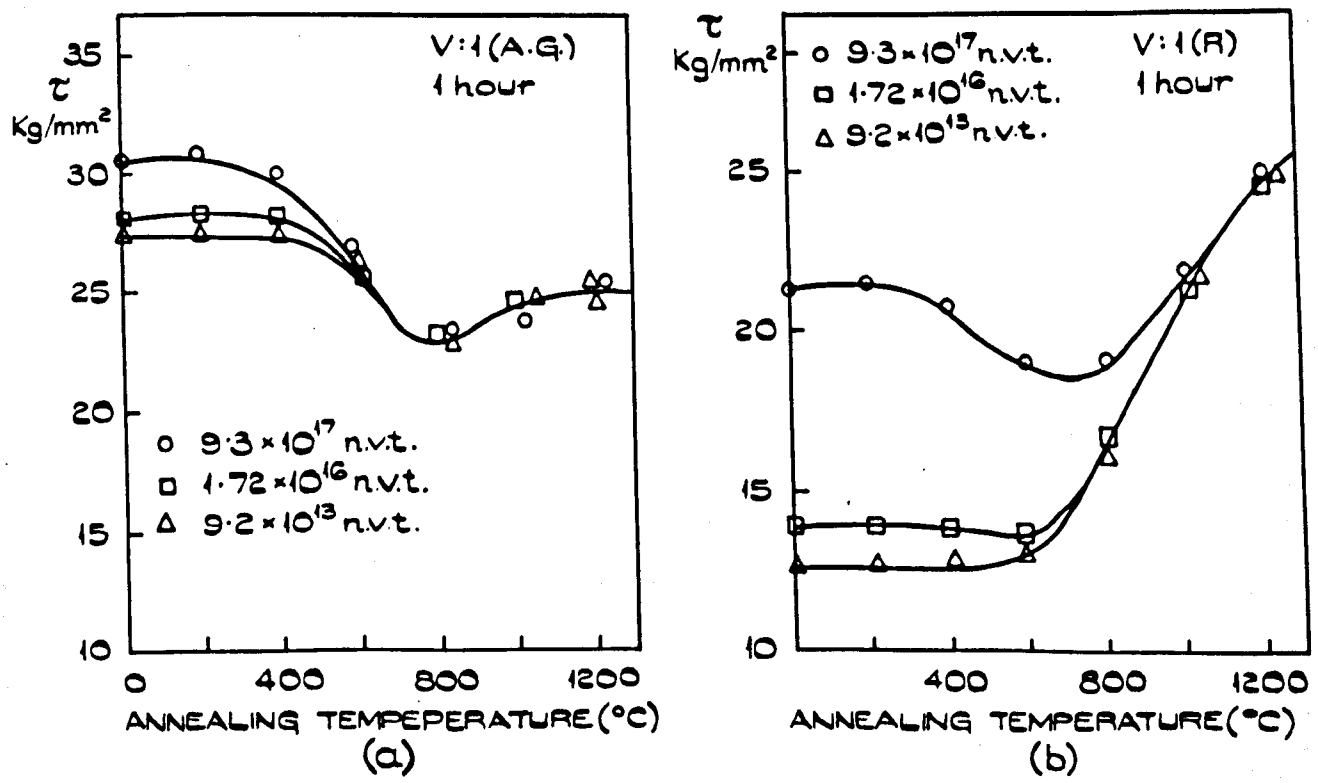

FIG. 6.10

EFFECT OF ISOCHRONAL HEAT TREATMENT FOR 1 HOUR IN AIR ON THE FLOW STRESS OF V:I IN THE AS GROWN (A.G) AND REDUCED (R) STATE.

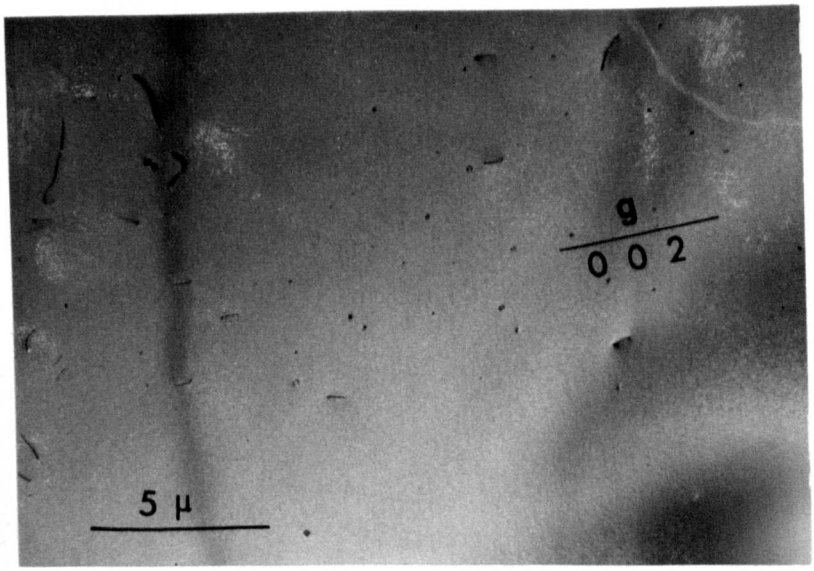

Fig. 6.11

Micrograph of a section of Fe : 1 irradiated in the reduced state to a dose of 9.3×10^{17} n.v.t. and subsequently annealed for 1 hour at $800^{\circ}C$ in air.

interstitial damage during irradiation and post-irradiation annealing is facilitated by direct recombinations for a vacancy supersaturation of this magnitude. In the reduced state, vacancies required for charge compensation diffuse out of the crystal, and cation-anion vacancy pairs cluster to form dislocation loops. The net result is a small excess of vacancies, which, on irradiation, is insufficient to assist direct recovery processes by reactions between vacancies and interstitials.

The results of this investigation lend support to the suggestion, made earlier, of the nature of the obstacles present in as-grown unirradiated crystals.

7. CONCLUSIONS.

In the work described in the foregoing chapters a detailed investigation has been made of the characteristic features of the ageing behaviour of doped magnesium oxide. Comprehensive experimental measurements support the conclusion that the flow stress arises from a superposition of several distinguishable contributions, and it has been found possible to correlate these effects with the observed flow stress for heat treatments over the range 0 - 1,800°K. In the experiments described the number of defect centres which must necessarily be considered justifies the care exercised in selecting experimental techniques which are sensitive to the state of impurity in the crystal.

Conclusions derived on the basis of the work presented in this thesis are listed below. The initial remarks apply to the advantages and limitations experienced in the techniques and systems used for study, followed by a summary of the main conclusions of this work.

1) The flow stress of doped crystals is markedly affected by heat treatment, but an interpretation in terms of particular defects requires a precise knowledge of the prior thermal history, and concurrent studies of the state of ions in solid solution and precipitate form. An accurate and convenient measure of the bulk flow stress has been found to be the extent of dislocation movement away from the region of a microhardness indent, provided that homogeneous samples are used and a comprehensive calibration is made over the whole flow stress range. The test is also sensitive to other physical properties of the crystal, (e.g. work of fracture), and is there-

fore only significant if the orientation is carefully controlled, and identical conditions are maintained for each test.

2) Optical and microwave absorption studies of the paramagnetic impurities used are essential in ascertaining the concentration and state of association of defects with heat treatment. In many cases, however, a direct knowledge of all the valence states is lacking, and the distribution of impurity must then be inferred from the effect of heat treatment on the detectable states.

3) Direct microstructural observations by electron microscopy are necessary in order to determine the parameters of a visible precipitate dispersion and to identify the precipitate structure. In this study, precipitates were found to be most readily detected by coherency strain contrast, and in many cases the precipitate dispersion corresponding to maximum hardness occurred for particle dimensions below the visibility limit.

4) A considerable advantage in the host lattice used is the range of techniques applicable to this study. A picture of the important portion of the thermal history during melt growth is lacking however, and the results obtained stress the need for further experimental studies in which both the cooling rate and impurity conditions are more carefully controlled.

5) The results presented support the conclusion that under normal circumstances the rate of cooling following melt growth is sufficient to retain a high supersaturation of vacancies of both signs in the crystal. In the as-grown state, vacancies are present as closely associated pairs and represent therefore a significant contribution to the flow stress of

unaged crystals. During subsequent heat treatments vacancy coalescence as dislocation loops is reflected in the initial plastic softening.

6) A large proportion of tri-and tetravalent impurities have been found to be isolated from charge compensating vacancies in the as-grown state. During ageing at low temperatures in air, oxidation of impurities and subsequent vacancy association is a necessary intermediate stage to the formation of a precipitate structure.

7) Superimposed on all impurity contributions at long ageing times at low temperatures, and predominating at high temperatures in air, is the contribution from a centre consisting of an interstitial oxygen ion in association with impurities. For extended anneals at high temperatures this centre is destroyed by interstitial-vacancy recombinations, or by coalescence to form larger centres which do not interact strongly with dislocations.

8) A low temperature ageing peak observed in all systems studied is attributed to the formation of a spinel precipitate dispersion. The experimental measurements support the conclusion that in the initial stages of yielding these particles do not deform with the matrix, and that an Orowan model for dislocation glide is applicable for precipitates with dimensions of only a few lattice spacings.

9) Nucleation of spinel precipitates is aided by the high vacancy supersaturation present in melt-grown crystals. The rapid nucleation rate

in this environment results in a fine precipitate dispersion which, because of the observed difficulty of dislocation glide in the spinel structure at room temperature, produces a marked hardening peak for even a low volume fraction of precipitate. The particle dispersion corresponding to the maximum in the flow stress in some systems is unresolvable in the electron microscope.

10) The contributions to the flow stress determined in this study could be more clearly distinguished if crystals containing a larger supersaturation of impurity were available. In this case precipitation hardening would be more readily defined, and a resolvable precipitate dispersion could be studied.. This would only be possible if a more satisfactory method of crystal growth was available for introducing higher concentrations of impurity ions.

11) This study has indicated the way in which ceramic crystals having a wide range of mechanical strengths could be produced. Low flow stresses are most easily achieved by annealing in reducing atmospheres. Extremely strong crystals may be formed by doping with high concentrations of tri-or tetravalent impurity ions, followed by annealing at high temperatures in air to enhance interstitial oxygen diffusion. Alternatively a correspondingly high vacancy supersaturation could be formed by heat treatments close to the melting point, followed by rapid cooling to room temperature to suppress spinel precipitate nucleation. By reageing crystals prepared in this way at a lower nucleating temperature a fine precipitate dispersion is expected, and extremely high flow stress could hence be attained.

Although the operation is made technically difficult by the rapid dissociation of magnesium oxide above 2,000°C, it could feasibly be performed under pressure.

REFERENCES

1) Joffé, A. and Lewitsky, M. 1925. Z. Physik. 31, 576.

2) Gorum, A.E., Parker, E.R., and Pask, J.A. 1958. J.Am. Ceram.Soc.41,161

3) Johnston, W.G. and Gilman, J.J. 1960. J. Appl. Phys. 31, 632.

4) Cottrell, A.H. Dislocations and Plastic Flow In Crystals. 1953. (O.U.P.) 58.

5) Johnston, W.G. 1962. J. Appl. Phys. 33, 2050.

6) Fleischer, R.L. 1962. J. Appl. Phys. 33, 3504.

7) Kroger, F.A. The Chemistry of Imperfect Crystals. 1964 (New-Holland) 201.

8) Dryden, J.S. 1963. J. Phys. Soc. Japan 18, Suppl. 3. 129.

9) Cook, J.S. and Dryden. J.S. 1962. Proc. Phys. Soc. 80, Pt.2, 479.

10) Dryden, J.S, Setsu Morimoto and Cook J.S. 1965, Phil. Mag. 12, 379.

11) Davidge, R.W. 1967, J. Matls. Sci. 2, 339.

12) Day, R.B. and Stokes, R.J. 1967. J. Am. Ceram. Soc. 50, 445.

13) Phillips, B, Somiya, S. Muan, A. 1961. J. Am. Ceram. Soc. 44, 169.

14) Lewis, M.H. 1968. Phil. Mag. 17, 481.

15) Manning. J.R. 1959. Phys. Rev. 116,69.

16) Hanlon. J.E. 1960. J. Chem. Phys. 32, 1492.

17) Keneshea, F.J. and Fredericks, W.J. 1965. J. Phys. Chem.Solids.26, 501.

18) Ronge, G. and Wagner, C. 1950. J. Chem. Phys. 18, 74.

19) Lidiard. A.B. 1957. Handbuch der Physik. 20, 246.

20) Dreyfus, R.W. and Nowick, A.S. 1962. Phys. Rev. 126, 1367.

21) Nowick, A.S. and Heller, W.R 1965. Adv. in Phys. 14, 101.

22) Petiau, J. 1963. J. Phys. 24, 564.

23) Burnstein, E, Davisson, J.W, and Sclar, N. 1954. Phys. Rev. 96, 819.

24) Haven, Y. 1955. Defects in Crystalline Solids (Bristol). The Physical Society 261.

25) Schneider, E.E. and Caffyn, J.E. ibid. 74.

26) Watkins, G.D. 1959. Phys. Rev. 113, 79.

27) Symmons, H. F. and Kemp. R.C. 1966. Brit.J. Appl. Phys. 17, 607.

28) Edner, A. 1932. Z. Physik, 73, 623.

29) Metag, W. 1932, Z. Physik 78, 363.

30) Schonfeld, H. 1932. Z. Physik, 75, 442.

31) Newey, C.W.A. 1963. Trans. Brit. Ceram. Soc. 62, 739.

32) Johnston, W.G. 1964. Bull. Am. Phys. Soc. 9, 271.

33) Fleischer,R.L. 1962. Acta. Met. 10, 835.

34) Pratt, P.L. Chang,R, and Newey. C.W.A. Appl. Phys. Letters 3, 83.

35) Johnston, W.G., Nadeau, J.S. Fleischer, R.L. 1963. J. Phys.Soc.Japan Suppl. 1, 18, 7.

36) Newey, C.W.A. Harrison,R.P. and Pratt, P.L. 1966. Proc. Brit. Ceram. Soc. 6, 305.

37) Lewis, T.J. and Wright, R.J. 1968. Brit. J. Appl. Phys.1, 441.

38) Southgate, P.D. 1966. J. Phys. Chem.Solids. 27, 1263.

39) Dahlberg, P. Carnahan, R.D. and Brittain, J.O. 1962. J. Appl. Phys. 33, 3493.

40) Stokes, R.J. 1965. J.Am. Ceram. Soc. 48, 60.

41) Bowen, D.H. Clarke, F.J.P. 1963. Phil. Mag. 8, 1257.

42) Pauling, L. The Nature of the Chemical Bond. (Cornell Univ.Press) 511.

43) Low. W. Paramagnetic Resonance in Solids. Solid State Physics. Suppl. 2 1960.

44) Wertz, J.E, Orton, J.W. and Auzins, P. 1962. J. Appl.Phys.33, 322.

45) Wertz, J.E. and Auzins, P. 1957. Phys. Rev. 106, 484.

46) Wertz, J.E. and Auzins, P. 1967, J. Phys. Chem. Solids 28, 1557.

47) Wertz, J.E. Saville, G.S. Hall, L and Auzins, P. 1964. Proc.Brit. Ceram. Soc. 1, 59.

48) Ashby, M.F. and Brown, L.M. 1963. Phil. Mag. 8, 1083.

49) Ashby, M.F. and Brown, L.M. 1963. ibid 8, 1649.

50) Venables, J.D. 1963. J. Appl. Phys. 34, 293.

51) Henderson, B. 1964. Phil Mag. 9, 153.

52) Bowen, D.H. 1963. Trans. Brit. Ceram. Soc. 62, 771.

53) Miles, G.D. 1965. J. Appl. Phys. 36, 1471.

54) Lang, A.R. and Miles, G.D. 1965J.kAppl. Phys. 36, 1803.

55) Lewis. M.H. 1966. Phil. Mag. 13, 777.

56) Stokes, R.J. and Li, C.H. 1964. Disc. Faraday Soc.38, 233.

57) Matkin, D.I. and Bowen. D.H. 1965. Phil. Mag. 12, 1209.

58) Stokes, R.J. 1962. Trans. A.I.M.E. 224, 1227.

59) Gorum, A.E. Luhman, W.J. and Pask, J.A. 1960. J. Am. Ceram. Soc 43, 241.

60) Brown, L.M. and Pratt. P.L. 1963. Phil. Mag. 8, 717.

61) Gilman, J.J. 1959, Acta. Met. 7. 608.

62) Miles, G.D. Clarke, F.J.P. Henderson, B. and King, R.D. 1966. Proc. Brit. Ceram Soc. 6, 325.

63) Groves, G.W. and Fine, M.E. 1964. J. Appl. Phys. 35, 3587.

64) Liu, T.S. Stokes, R.J. and Li.C.H. 1964. J. Am. Ceram.Soc.47, 276.

65) Clarke, F.J.P. and Sambell, R.A.J. 1960. Phil Mag. 5, 697.

66) Westwood, A.R.E. Goldheim, D.L. and Lye, R.G. 1967. Phil. Mag.16, 505.

67) Keh, A.S. Li, J.C.M. and Chu.Y.T. 1959. Acta Met 7, 694.

68) Washburn, J, Groves, G.W. Kelly, A. and Williamson, G.K. 1960. Phil. Mag. 6, 991.

69) Low, W. 1956. Proc.Phys. Soc. B.69, 1169

70) McMahon, D.H. 1964. Phys. Rev. 134A, 128.

71) Soshea, R. W, Dekker, A.J. and Sturtz, J.P. 1958. J. Phys.Chem. Solids. 5, 23.

72) Glass, A.M. and Searle, T.M. 1967. J. Chem. Phys, 46. 2080

73) Abragam, A. and Pryce, H.M.L. 1951, Proc. Roy. Soc. A.205, 135.

74) Dickey, D.H. and Drumheller, J.E. 1967. Phys. Rev. 161, 279.

75) Sturge, M.D. 1963. Phys. Rev. 130, 639.

76) Low. W. 1957. Phy. Rev. 105, 801.

77) Auzins. P. 1965. J. Chem. Phys. 43, 1229.

78) Griffiths, J.H.E. and Orton. J.W. 1959. Proc. Phys. Soc. 73, 948.

79) Alper, A.M. McNally, R.N. Doman, R.C. and Keihn, F.G. 1964. J.Am. Ceram.Soc.47, 30.

80) Fletcher, J.R, Marshall, F.G. Rampton, V.W. Rowell, P.M. and Stevens, K.W.H. 1966. Proc. Phys. Soc. 88, Pt.1, 127.

81) Freidel, J. 1965. Electron Microscopy and Strength of Crystals, Proc. 1st Berkley Int. Materials Conf. (New York : Interscience) p.634.

82) Fleischer, R.L. and Hibbard, W.R. 1963. The Relation Between the Structure and Mechanical Properties of Materials, National Physical Laboratory, Symposium. No.15. (H.M.S.O) p.262.

83) Whitworth, R.W. 1967. Phil. Mag. 15, 305.

84) Eshelby, J.D, Newey, C.W.A. Pratt, P.L. and Lidiard, A.B. 1958. Phil. Mag. 3, 75.

85) Kroupa, F. and Hirsch, P.B. 1964. Disc. Farad.Soc.38, 49.

86) Foreman, A.J.E, 1968. Phil. Mag. 17, 353.

87) Mott, N.F. and Nabarro, F.R.N. 1946. J. Inst. Metals. 72, 367.

88) Hornstra, J. 1960, J. Phys.Chem.Solids. 15, 311.

89) Lewis, M.H. Private Communication.

90) Massazza, F. and Sirchia, E. 1958. Chim.Ind. (Milan) 40, 378.

91) Kelly, A. and Nicholson. 1963. Prog. Mater. Sci. 10, 149.

92) Newey, C.W.A. and Radford, K.C. 1967. Anisotropy in Single Crystal Refractory Compounds (Proc.Int.Conf. at Dayton, Ohio)Plenum Press 2,321.

93) Orowan, E. 1948. Symp. on Internal Stresses (Institute of Metals) p.451.

94) Nabarro, F.R.N. 1952. Adv.Phys. 1, 269.

95) Humphreys, F.J. and Martin, J.W. 1967. Phil. Mag. 16, 143.

96) Weatherly, G.C. 1968. Phil. Mag. 17, 791.

97) Brown, L.M. Woolhouse, G.R. and Valdre, U. 1968. Phil. Mag. 17, 781.

98) Embury, J.D. and Nicholson, R.B. 1965. Acta. Met. 13, 403.

99) Lorimer, G.W. and Nicholson, R.B. 1966. Acta Met 14, 1009.

100) Huntington, H.B. 1953. Phys. Rev. 91, 1092.

101) Cochardt, A.W. Schoeck, G. and Wiedersich. H. 1955. Acta Met. 3, 533.

102) Graham, L.J. and Sines,G. 1966. J. Appl. Phys. 37, 4207.

103) Harrison, R.P. and Newey, C.W.A. 1968. Phil. Mag. 17, 525.

104) Ono, K. 1968. J. Appl. Phys. 39, 1803.

105) May, J. E. and Kronberg. M.L. 1960. J. Am. Ceram. Soc. 43, 525.

106) Miles, G.D. 1964. Acta. Met. 12, 1241.

107) Copley, S.M. and Pask, J.A. 1965. J. Am. Ceram. Soc. 48, 139.

108) Kinchin, G.H. and Pease, R.S. 1955. Rep. on Prog. in Physics 18, 1.

109) Silsbee, R.H. 1957. J. Appl. Phys. 28, 1246.

110) Henderson, B. and King. R.D. 1966. Phil. Mag. 13, 1149.

111) Martin. D.G. 1968. J. Phys. C. (Proc. Phys. Soc) 1, 333.

112) Hickman, B.S. and Walker, D.G. 1965. Phil. Mag. 11, 1101.

113) Sambell, R.A.J. and Bradley, R. 1964. Phil. Mag. 9, 161.

114) Groves, G.W. and Kelly, A. 1963. Phil. Mag. 8, 1437.

115) Nadeau, J. S. 1963. J. Appl. Phys. 34, 2248.